CONCATENATION OF A REACTIVE TRANSPORT MODEL TO SIMULATE CO_2 SEQUESTRATION IN GEOLOGIC MEDIA

by
Tristan Paul Wellman

Submitted in Partial Fulfillment
Of the Requirements for the

Masters of Science in Hydrology

New Mexico Institute of Mining and Technology
Department of Earth and Environmental Science
Socorro, New Mexico

December, 2002

ABSTRACT

Majority opinion within the science community is that anthropogenic greenhouse gases contribute to global warming. Of the greenhouse gases, CO_2 plays a significant role in trapping heat near the surface of the earth. Technology is available to capture CO_2 emissions from energy plants, and these captured emissions can be sequestered in deep basin repositories. However determining the viability, risks, and optimal locations of sequestering CO_2 in geologic media requires modeling the complex interactions between the injected CO_2, matrix, and pore fluid under site specific pressure and temperature conditions. Previous studies consisted mainly of simulating flow and transport of CO_2 in subsurface environments. Realizing the importance of chemical processes, we assembled the TR-T reactive transport model, which in addition to flow and transport simulates the impact of fluid-mineral interactions on CO_2 mobility. The TR-T simulator is an assemblage of the CO_2 flow and transport module TOUGH2-EOSCO2 and TRANS, a multicomponent geochemistry module. While the main goal of this project was to create the base version of the TR-T simulator we have begun comparing TR-T predictions to results from laboratory experiments. Comparisons to laboratory experiments provide a means to assess the accuracy of the TR-T simulator. The experiments also offer information to parameterize the TR-T model for specific media. Model predictions show

excellent agreement to results from the first completed experiment. Awaiting additional results, we performed a suite of bench scale sensitivity simulations to determine the effects of varying brine pH and alkalinity, and rock type. Our analysis indicated that varying brine pH and alkalinity resulted in a 0-5 % difference in mineral volume fraction at 1.25×10^7 seconds, depending upon the mineral assemblage. However, we found that variability among rock type was extreme, suggesting that CO_2 injection in some geologic media may induce significant dissolution and dramatically increase CO_2 mobility. As an introduction to larger scale simulations we simulated CO_2 injection at the reservoir scale. Contrary to the bench scale results, the TR-T simulator predicted negligible changes to the matrix. We hypothesize the displacement of brine by the expanding supercritical CO_2 plume may limit brine reactivity with the geologic media. However, we employed a smaller ratio of injected CO_2 to calcite volume in our reservoir scale simulation, which may account for the discrepancy between the simulated matrix change at the bench and reservoir scales. These introductory simulations were used to quantify fluid-mineral interactions, compare simulations to experimental data, and to demonstrate the ability of the TR-T simulator. The ultimate goal will be to employ the TR-T simulator to identify ideal CO_2 repositories and to assess the effectiveness and environmental implications of sequestering CO_2 in deep basin environments.

TABLE OF CONTENTS

LIST OF FIGURES

Figure **Page**

LIST OF TABLES

This thesis is accepted on behalf of the
Faculty of the Institute by the following committee:

Brian McPherson
Advisor

6-11-02
Date

I release this document to the New Mexico Institute of Mining and Technology.

Student's Signature

6-5-02
Date

CHAPTER 1: INTRODUCTION

The main objective of this study was to create the TR-T reactive transport simulator for analysis of CO_2 sequestration in geologic media. The TR-T simulator is a combination of the mass and energy flow simulator TOUGH2-EOSCO2 (Cole, 1999; Pruess, 1999), and the reactive chemistry simulator TRANS (Lichtner, 2000), coupled through a driver program developed as part of this study. In addition to simulating the flow of mass and energy due to CO_2 injection in geologic media, the TR-T simulator models fluid-media interactions and the subsequent changes to the matrix and fluid mobilities as a result of chemical processes. This project is a part of larger collaborative effort between the Earth and Environmental Science Department of New Mexico Tech (NMT), the Petroleum Recovery Research Center of NMT (P.R.R.C.), and the Los Alamos National Laboratory (L.A.N.L.). Achievements in this study include creating the base version of the TR-T reactive transport simulator, comparing TR-T simulations to laboratory results, performing a sensitivity analysis of key parameters, and creating a high-pressure permeameter with digital data acquisition.

Our study focuses on geologic sequestration of CO_2 emissions from power plants. CO_2 is a major greenhouse gas believed to contribute to global warming (Jones, 1999; Marland, 1999) (Figure 1-1) and the magnitude of CO_2 emissions (by state) amounts to millions of tons per year.

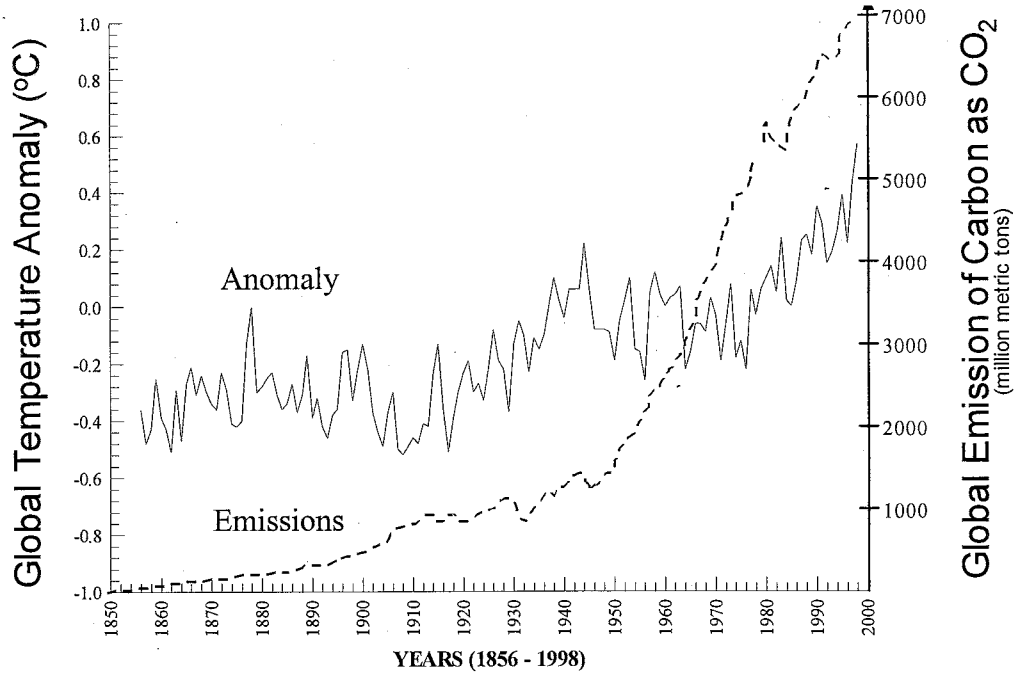

Figure 1-1: Global temperature anomaly Jones, (1999) in relation to anthropogenic global emissions Marland et al, (1994). Plot indicates a positive correlation between temperature deviations from the mean and anthropogenic CO_2 emissions

Therefore, there is a significant source of greenhouse gas emissions that may be sequestered in geologic media, possibly preventing these emissions from contributing to global warming. In addition 85% of the world's energy comes from the burning of fossil fuels (Wawersik, 2001) indicating that CO_2 emissions from energy plants are of global concern. Fortunately, technology is available to capture CO_2 from energy plant emissions before entering the atmosphere. We hypothesize that geologic basins may serve as viable CO_2 repositories. Knox and Hovorka (2001) have shown that the locations of potential CO_2 repositories are ubiquitous and disperse across the United States (Figure 1-2). These potential repositories may likely be available at little to no cost since they are of little

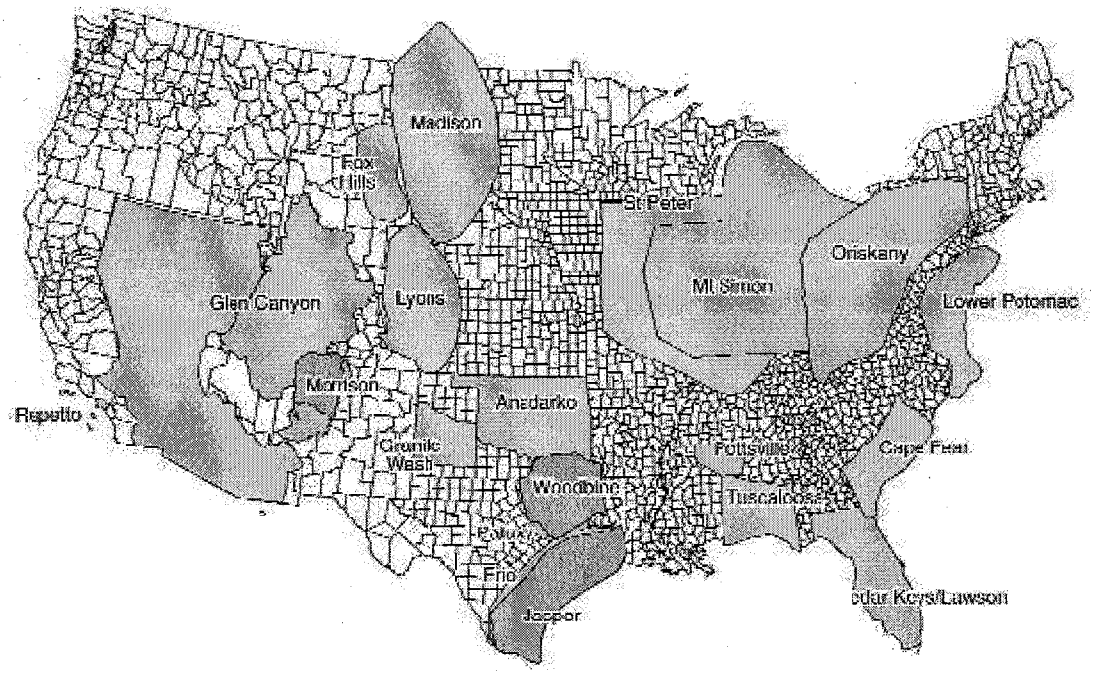

Figure 1-2: Saline aquifers formations throughout the United States suitable for potential CO_2 injection. Adapted from Knox and Hovorka (2001).

economic value and are not in direct competition with other industries. In addition, abundant subsurface data associated with brine formations and depleted petroleum reservoirs are routinely acquired during oil and gas extraction by the petroleum industry. Finally, preexisting well bores, created to extract oil and gas, may be employed to inject CO_2 into the subsurface, saving the added cost of developing new injection wells. In short we may be able to significantly reduce greenhouse gas emissions entering the atmosphere by injecting CO_2 emissions in deep subsurface geologic reservoirs.

However, we must consider the environmental implications of CO_2 injection. Probably the most important issue is how long can CO_2 be effectively sequestered in the subsurface. CO_2 in gas or supercritical form is always less dense than brine and therefore buoyancy

will actively force CO_2 back towards the ground surface in a brine-saturated reservoir. Some mineral or aqueous trapping may occur (Wawersik et al., 2001) where the CO_2 is dissolved into solution or mineralizes, but the majority of CO_2 should remain in the separate (gas or supercritical) phase. If CO_2 returns to the surface, potential severe environmental and safety hazards (e.g., asphyxiation) could result around discharge sites. However, if CO_2 is injected into low permeability units at sufficient depths, it may be sequestered from the atmosphere for time periods much greater than 5,000 years (Cole, 1999). Therefore the question of interest becomes: does the benefit of preventing CO_2 emissions from entering the atmosphere in the near term outweigh the potential environmental implications of CO_2 returning to the surface at some time in the future?

Our group goal is to assess the feasibility and environmental implications of sequestering CO_2 in geologic media. The P.R.R.C. is performing core flooding experiments injecting CO_2 and into geologic media to quantify fluid mineral interactions and the resulting permeability-porosity relationships of various media. A pilot injection study will be directed by L.A.N.L in the near future to measure field scale CO_2 injection processes. Our contribution is the creation of the TR-T reactive transport simulator.

The TR-T simulator is an assemblage of three individual modules comprising 145 program files and roughly 50,000 lines of Fortran computer code. Flow of mass and energy is simulated by TOUGH2 developed by Karsten Pruess at the Lawrence Berkeley National Laboratory (Pruess, 1999). TOUGH2 is linked to a CO_2 equation of state (EOSCO2) applicable for deep basin environments developed by Barett Cole at New

Mexico Tech (Cole, 1999). Reactive chemistry is simulated by TRANS developed by Peter Lichtner at the Los Alamos National Laboratory (Lichtner, 2000). We developed a driver program in this study, which sequentially couples TOUGH2-EOSCO2 to TRANS. In the coupled mode TOUGH-EOSCO2 simulates the flow of mass and energy in the system. At the convergence at each time step execution control is passed from TOUGH-EOSCO2 to TRANS, which repeats the TOUGH-EOSCO2 time step, simulating the chemical processes. Coupled variables are updated and passed at the convergence of each time step through the driver program. The coupled TR-T simulator models multidimensional, multiphase, multicomponent, nonisothermal, reactive transport in porous media, including that associated with subsurface CO_2 injection and sequestration.

Although a work in progress, the base version of the TR-T is complete. We have tested mass balance in 2-D systems and aqueous CO_2 transport in 1-D systems. Mass balance error was shown to be both a function of injection rate and time step size. In all cases global mass balance errors were less than 1.6 percent but could be constrained to less than 1 percent by decreasing time step size. CO_2 transport for a constant velocity non-reactive matrix was used to demonstrate that the TR-T aqueous CO_2 profiles match those of TOUGH2-EOSCO2 running independently (standalone mode). The results indicate that transport is operating correctly and mass balance error is reasonable in the TR-T simulator. However, future testing and development is required.

We performed a set of initial tests to aid in model development and parameterization. We compared TR-T simulations to P.R.R.C. core flooding laboratory results to assess

whether our model can accurately capture reactive transport at the bench scale. In addition we performed a sensitivity analysis to determine the dominant fluid and media properties in various geologic systems. Finally as an introduction to future work, we performed a reservoir CO_2 injection simulation in carbonate basin. Future experimental results will be used to quantify model parameters and to support that the TR-T simulator accurately simulates CO_2 sequestration in geologic reservoirs. In this and future studies, the TR-T simulator will be used to assess the feasibility and environmental implications of injecting CO_2 in geologic basins throughout the United States.

CHAPTER 2: PREVIOUS WORK

The practice of numerically simulating CO_2 geologic sequestration remains in the developmental stage, with only a few studies. Even fewer studies have employed reactive transport simulators, and much of the research is proprietary or in the developmental stages. A brief overview of published previous work in CO_2 sequestration modeling is provided below.

Non-reactive transport modeling began in the early 90's when Van der Meer (1992) simulated CO_2 sequestration in a circular anticlinal stratigraphic trap. In his simulations Van der Meer injected 2.5×10^6 kg day^{-1} of CO_2 into 6 injection wells within a 50m thick sandstone unit dipping 1 degree. Lateral CO_2 migration was caused by upwardly decreasing pressure gradients, and vertical migration occurred from buoyancy forces resulting from density contrasts between CO_2 and brine. Van der Meer concluded that 2-3 percent of the porous media could be used to store CO_2 before it escaped past the edges of the anticlinal limbs of a stratigraphic trap.

A subsequent study by Holt, Jensen, and Lindeburg (1995) modified the black oil simulator ECLIPSE 100 to include the solubility of CO_2 in H_20. Their study incorporated empirical relative permeability relations between liquid and gas phases, previously

neglected by Van der Meer (1992). However, reactive chemistry between the fluid and media was not considered. In their simulations, CO_2 was injected at a rate of 3.9 x 10^6 kg day^{-1} into a dipping heterogeneous sandstone media. Their findings showed that injection rate and absolute permeability were the dominant factors of migration of injected CO_2. In addition they found that under high injection rates viscous forces dominated fluid flow, CO_2 preferentially flowed through higher conductivity pathways, and under low injection rates gravity segregation dominated and a stability front resulted. By adding the solubility function to the ECLIPSE 100 model they determined that 3 to 11 % of the injected CO_2 could be trapped in the dissolved phase.

Another study by Van der Meer (1995) addressed CO_2 injection into a 2-dimensional quasi-infinite aquifer. Van der Meer (1995) simulated CO_2 injection at a rate of 1.5 x 10^7 kg day^{-1} for 50 years in a 55-meter thick sandstone reservoir. Following a 100-year shut in period the plume grew in size from 16 to 18 km in diameter. Van der Meer concluded that it was possible to sequester significant amounts of CO_2 in the subsurface but added that capturing the combined effects of viscous fingering and gravity segregation would require 3-dimensional modeling.

A study by Lindberg (1995) described simulations of CO_2 injection at 8000 meters depth in a horizontally finite aquifer. CO_2 was injected at a rate of 1.5 x 10^8 kg day^{-1} for 25 years into a 160-meter thick unit. Lindberg (1995) assumed that all CO_2 reaching the upper model boundary escaped into the atmosphere. A sensitivity analysis of absolute permeability showed that in low permeability media (< 1 Darcy), CO_2 did not reach the

model boundaries in less than 1000 years, resulting in minimal loss to the atmosphere. For higher permeability media, larger distances from the upper boundaries were necessary to sequester CO_2 for the same 1000-year period. In the worst case scenario using a media of 8 D and a well placement 3000m from the boundary, 17 percent of the CO_2 escaped to the atmosphere in the first 2000 years, while the remainder resided in the dissolved phase of the formation water. Similar to previous studies, Lindberg (1995) did not incorporate chemical reactions between the CO_2, brine, and geologic media. He concluded that CO_2 storage is feasible beneath horizontal seals provided that injection locations are sufficiently deep.

Law and Bachu (1996) conducted a study incorporating the STARS model to simulate multidimensional, multicomponent flow and transport of CO_2 injected into a sedimentary basin for 30 years. The STARS model allows phase partitioning between separate and dissolved phase CO_2. They limited their injection rates such that pressure was below 90% lithostatic to avoid hydrofracturing and varied porosity and permeability and other parameters to assess the effects of CO_2 injection rate, amount, and distribution. As with previous studies they neglected chemical reactions between the media and fluid. They concluded that the most important factors affecting CO_2 storage potential include intrinsic permeability and injection pressure, while the unit thickness is moderately important. Variable porosity produced minimal effects on the results.

Weir et al. (1996) used the multiphase, multicomponent TOUGH2 model to simulate CO_2 injection in geologic media. In their model, they injected CO_2 at an average rate of 8.6 x

10^6 kg day^{-1} to a depth of 2950 meters in a 3000-meter deep fresh water aquifer. They neglected reactive chemical reactions between the fluid and media. Their results showed that using a 20:1 ratio of horizontal to vertical permeability, 12 percent of the injected CO_2 would escape to the atmosphere in 12 years. They also concluded that the most significant factor affecting volumetric CO_2 storage potential is intrinsic permeability.

Patterned after the work of Weir et al. (1996), Cole (1999) developed a CO_2 equation of state for use with the TOUGH simulator that incorporated the effect of capillary pressure phenomena. In addition Cole (1999) changed the previously employed variable switching technique used in TOUGH2 to a persistent set of primary variables applicable in both saturated and unsaturated conditions. Cole (1999) performed a sensitivity analysis to assess which physical parameters controlled the long-term storage of CO_2. His analyses indicated that, in agreement with previous studies, absolute permeability was the dominant mechanism controlling CO_2 migration. However the injection rate and injection depth were also of significant importance. Cole (1999) did not consider chemical reactions between media, formation fluid, and injected CO_2.

Johnson et al. (2001) used the simulator package NUFT (Nitao, 1998) to model CO_2 sequestration in geologic media. The NUFT simulator models the reactive transport of CO_2 injected into geologic media. Simulations were patterned after field scale CO_2 injections that are taking place at Statoils North-Sea Sleipner facility. The near field geologic system at the facility consists of a 200-meter thick porous sandstone saturated with saline formation water and a 25-meter thick shale capping layer. CO_2 injection was

simulated at a rate of 27.4 kg day^{-1} for 10 years (prograde) followed by a period of 10 years of zero injection (retrograde). Their findings indicated that intra-aquifer structures have the most control of separate phase CO_2 migration paths and solubility within the aquifer unit, but that a capping layer at least 25 meters thickness is required to prevent CO_2 from eventually escaping into the atmosphere. Results from the simulations showed that intra-aquifer structures attenuated the supercritical CO_2 plume, causing more fluid to interact with a larger body of formation fluid and resulting in more dissolved CO_2 and smaller vertical migration velocities. However, regardless of whether intra-shale units were present, the immiscible CO_2 plume migrated toward the surface. In each simulation, the low permeability capping layer effectively confined all injected CO_2. These simulations indicated negligible mineral precipitation. The significance of the minimal precipitation (.05 to .2 percent volume fraction) is questionable in light of the uncertainties present in estimating reactive transport modeling parameters such as mineral kinetic reaction rates. The simulations showed magnesite to be the dominant mineral to precipitate in the capping layer, with the maximum precipitation less than 1 percent of the total volume after 30 years. The magnesite precipitation is hypothesized to seal the micro fractures, which are present in the shale unit and therefore act in increasing its sealing ability with continued CO_2 flushing. The overall results revealed that precipitation may be an influencing factor in cases where minute changes in porosity result in extreme permeability changes.

In summary, previous work indicates it is possible to sequester CO_2 in the subsurface for long periods under ideal conditions. Previous studies also suggest that absolute

permeability of both the aquifer and capping layer are the dominant geologic controls on CO_2 migration. We test the hypothesis that chemical reactions induced by CO_2 injection in deep basin environments may alter existing predictions of transport and storage potential. Building on the research of Cole (1999), we created the TR-T CO_2 reactive transport simulator for geologic media. The TR-T simulation package couples the flow simulator TOUGH2 (Pruess, 1999), the CO2 equation of state of Cole (1999), and the chemical reaction and transport simulator TRANS (Lichtner, 2000).

CHAPTER 3: TOUGH2 FLOW SIMULATOR

3.1 TOUGH2 INTRODUCTION

We employed TOUGH2 to simulate flow of mass and energy in our TR-T reactive transport simulator. TOUGH2 simulates nonisothermal, multiphase, multicomponent fluid systems of one, two, or three dimensions in porous and fractured media. Mass and energy balance equations are approximated in space using an integral finite volume approach, and discretized in time using a fully implicit method (Edwards, 1972; Narasimhan and Witherspoon, 1976). In this study, TOUGH2 employs the CO_2 equation of state developed by Cole (1999). The primary and secondary variables are summarized in Table 3-1.

EOSCO2 PRIMARY VARIABLES	EOSCO2 SECONDARY VARIABLES
T = Temperature	H = Enthalpy **
P = Pressure	ρ = Density **
X_{CO2} = Mass Fraction Dissolved CO_2	μ = Dynamic Viscosity **
S_{CO2} = Saturation Separate Phase CO_2	P_c = Capillary Pressure *
	k = Relative Permeability
	* separate phase ** liquid and separate phase

Table 3-1: showing the primary and secondary variables used in the TOUGH2- CO_2 equation of state details from Cole (1999). EOSCO2 represents the CO_2 equation of state

The primary variables are solved iteratively within the TOUGH2 simulator. At each

iteration, the CO_2 equation of state calculates secondary variables necessary to solve the mass and energy balance equations. The following section provides a general overview of TOUGH2. A more detailed description is given by Pruess (1999).

3.2 GRID ARCHITECTURE/INTER-CELL TRANSPORT

TOUGH2 solves mass and energy balance equations that describe inter-cell fluid and heat flow. A mesh-generator utility employs either radial or Cartesian coordinates. A multiple interacting continua (MINC) method (Pruess, 1999) enables simulation of fractured media, extending a dual permeability approach to more than two domains. Advective and diffusive mass and energy transport can occur in all fluid phases. Thermal dispersion is considered negligible. Mass and energy balance equations are discretized in space using an integral finite volume approach (Edwards, 1972; Narasimhan and Witherspoon, 1976) to calculate mass and energy transport. Excluding spatial gradients, the integral finite volume approach avoids reference to a global coordinate system. Mass and energy transport occur through directionless connections of a finite length between adjacent cells, which simplifies calculations of traditional finite difference methods in cases of irregular grid boundaries.

TOUGH2 assumes that primary and secondary variables are homogeneous (constant) throughout each cell, effectively providing averaged values rather than a distribution of values within the cell. At the convergence of each time step TOUGH2 updates the primary and secondary variables, and mass and energy transport are calculated for each cell connection.

Inter-cell fluxes are calculated using an assigned weighting scheme (upstream, harmonic, or geometric). The upstream weighted mobility option is employed in this study to achieve unconditional stability (Peaceman, 1977), as it may help avoid convergence to non-physical solutions (Aziz and Settari, 1979). One downside to using upstream weighting is that it will often produce excessive front smearing (Adenekan et al., 1993).

3.3 SYSTEM CONSTRAINTS

To properly constrain each system the number of equations must equal the number of unknowns. Gibbs phase law is used to determine the thermodynamic degrees of freedom in the system given as,

$$F = NK + 2 - NPH\,. \qquad \textbf{(Eq. 3-3-1)}$$

Gibbs phase law states that at chemical equilibrium the thermodynamic degrees of freedom (F) must equal the number of components (NK) plus two minus the number of phases (NPH). Three components are used in this study: H_2O, aqueous CO_2, and separate phase CO_2. Therefore 3 thermodynamic degrees of freedom exist within the system. Since more than one phase may exist in each cell, the saturation degrees of freedom must also be taken into account given by

$$\sum_{\beta=1}^{NPH} S_\beta = 1. \qquad \textbf{(Eq 3-3-2)}$$

TOUGH2 constrains the cumulative saturation (S) of all phases (β) equal to unity, making the degrees of freedom associated with saturation equal to NPH-1. For this study NPH -1 = 1, and the total degrees of freedom (NK1) is equal to 4, or

$$NK1 = F + NPH - 1 = NK + 1 \ . \qquad \textbf{(Eq 3-3-3)}$$

Therefore, 4 primary variables are required by TOUGH2 to simulate H_2O and CO_2 in both dissolved and separate phases in a nonisothermal system.

3.4 MASS AND ENERGY BALANCE EQUATIONS

Discretization using the integrated finite volume method (Edwards, 1972; Narasimhan and Witherspoon, 1976) results in a set of strongly coupled nonlinear algebraic equations with the time dependent primary variables as unknowns. The general balance equation for mass and energy can be written as

$$\frac{d}{dt}\int_{V_n} M^{\kappa} dV_n = \int_{\Gamma_n} F^{\kappa} \bullet N d\Gamma_n + \int_{V_n} q^{\kappa} dV_n \ . \qquad \textbf{(Eq 3-4-1)}$$

This general mass and energy balance equation represents the change in the volume normalized mass or energy (M^{κ}) of each component (κ) with time (t) in each cell equal the mass or energy flux per unit area (F^{κ}) into each cell plus any volume normalized source or sink of mass or energy (q^{κ}) within the cell for each component. The left hand

term represents the change in mass or energy accumulation in each cell volume. The mass per unit volume is calculated by

$$M^{\kappa} = \phi \sum_{\beta=l,g} S_{\beta} \rho_{\beta} X_{\beta}^{\kappa} \qquad \sum_{\kappa=H2O,CO_2} X_{\beta}^{\kappa} = 1 \ . \qquad \textbf{(Eq 3-4-2)}$$

This relation shows that the mass per unit volume of component κ is calculated by summing the mass per unit volume (M) of component κ from each fluid phase β contained within the pore fraction (ϕ). The mass of each component equals the product of the saturation (S), density (ρ), and mass fraction (X) of each fluid phase. The energy per unit volume is given by,

$$M^{\kappa} = (1-\phi)\rho_r C_r T + \phi \sum_{\beta=l,g} S_{\beta} \rho_{\beta} E_{\beta} \quad . \qquad \textbf{(Eq 3-4-3)}$$

The first term is the sum of the energy within the media and is a product of the media density (ρ_r), specific heat of the geologic material (C_r), and the Temperature (T). The energy contained within the fluid is the sum of the product of the saturation, density, and internal energy (E) of all fluids.

Inter cell fluid flux in the primary TOUGH2 governing equation (3-4-1) is calculated using Darcy's Law for multiphase flow multiplied by the density of the respective phase,

$$F_\beta = u_\beta \rho_\beta = -k \frac{k_r}{\mu_\beta} \rho_\beta (\nabla P_\beta - \rho_\beta g), \qquad \textbf{(Eq 3-4-4)}$$

where the sum of the fluxes of each phase equals the total mass flux of each component κ. The flux (f) is proportional to the potential term and the intrinsic permeability of the media, corrected by the relative permeability (k_r) in the case of a multiphase system.

Permeability is directly related to the hydraulic conductivity of the media and must occasionally be modified in the presence of a gas phase. The Klinkenberg relation is used to adjust the intrinsic permeability (k) when absolute permeability of the gas phase increases at low pressures (Klinkenberg, 1941) and is given by

$$k = k_{\text{inf}} \left(1 + \frac{b}{P} \right). \qquad \textbf{(Eq 3-4-5)}$$

Intrinsic permeability (k) is estimated by the product of the permeability at infinite pressure (k_{inf}) and a correction term $\left(1 + \frac{b}{P} \right)$, where P represents pressure and b represents the Klinkenburg coefficient.

Vapor pressure lowering is calculated using Kelvin's equation. The effective vapor pressure (P_v) is reduced from the saturated vapor pressure (P_{sat}) by the vapor pressure lowering factor given by

$$P_v(T,S_l)=\left(\exp\left[\frac{M_w P_{cl}(S_l)}{\rho_l R(T+273.15)}\right]\right)\cdot P_{sat}(T). \qquad \textbf{(Eq 3-4-6)}$$

This equation relates the vapor pressure as an exponential function of the pressure difference between the gas and liquid (P_{cl}) and the saturation pressure (P_{sat}) at ambient temperature.

The equivalent energy flux term includes contributions from conduction and heat convection. The total energy flux is represented by

$$F^{\kappa}=-K\nabla T+\sum_{\beta=l,g}H_{\beta}F_{\beta} \qquad \textbf{(Eq 3-4-7)}$$

where the total energy flux (F_k) is equal to the conductance term (a product of the thermal conductivity (K) and temperature gradient (∇T)) and the convective heat flow (the summation of product of the enthalpy (H_β) and fluid flux (F_β) of each phase).

3.5 SPACE AND TIME DISCRETIZATION

A numerical approximation is employed to solve the set of coupled nonlinear mass and energy transport equations. Since the procedure for solving both the energy and mass balance equations are quite similar, the mass balance solutions are provided as representative of both methods.

Since all parameters are considered to be volume averages, the integral of the

accumulation term reduces to

$$\int_{V_n} MdV = V_n M_n \,, \qquad \textbf{(Eq 3-5-1)}$$

the product of cell (n) volume and volume normalized mass or energy.

Similarly, fluxes across each cell surface reduce to

$$\int_{\Gamma_n} F^{\kappa} \bullet n d\Gamma = \sum_m A_{nm} F_{nm}^{avg} \quad , \qquad \textbf{(Eq 3-5-2)}$$

where the integral is reduced to the summation of the average fluid flux (F_{avg}) multiplied by the respective cross sectional area A_{nm} connecting cells N and M through which the fluid is transported.

Substituting the two above simplifications into the TOUGH2 governing equation (Eq 3-4-1) transforms the integral components to algebraic form. Employing a fully implicit time discretization the simplified form is represented by

$$\frac{dM_n^{\kappa}}{dt} = \frac{1}{V_n} \sum_m A_{nm} F_{nm}^{\kappa} + q_n^{\kappa} \qquad \textbf{(Eq 3-5-3)}$$

Using a fully implicit approach, the transient (accumulation) term depends on the parameter values of the current time and previous time step. If values for the mass and

energy equations are correct, the left-hand-side (LHS) terms must equal the right-hand-side (RHS) terms. Discretizing in time using the fully implicit approach and constraining the residual (R) to zero leads to

$$R_n^{\kappa,K+1} = M_n^{\kappa,K+1} - M_n^{\kappa,K} - \frac{\Delta t}{V_n}\left[\sum_m AF_{nm}^{\kappa,K+1} + V_n q_n^{\kappa,K+1}\right] = 0 \ . \qquad \textbf{(Eq 3-5-4)}$$

However, a zero residual is impossible on a finite arithmetic machine. For that reason a tolerance is set based on the accuracy of the machine.

3.6 NEWTON-RAPHSON ITERATION METHOD

The Newton-Raphson method is employed as a means to attain a near zero solution residual of the coupled, non-linear mass and energy equations. For each new time step, primary variables values of the last time step are chosen for the first iteration guess. These primary variables are used in constitutive relations by the CO_2 equation of state to calculate the secondary variables present in the mass and energy balance equations discussed above. Each primary variable is individually incremented to calculate the effect to the solution residual caused by each primary variable change. A first order Taylor series expansion, is performed on each residual given by,

$$R_n^{\kappa,K+1}\left(x_{i,p+1}\right) = R_n^{\kappa,K+1}\left(x_{i,p}\right) + \sum_i \left.\frac{\partial R_n^{\kappa,K+1}}{\partial x_i}\right|_p \left(x_{i,p+1} - x_{i,p}\right), \qquad \textbf{(Eq 3-6-1)}$$

where the residual error at time (K+1) of the primary variable (x_i) at iteration (p) is equal to the residual at the previous iteration plus the sum of the change in the residual for each primary variable increment multiplied by the difference in the primary values between iterations. Constraining this solution to converge to zero yields

$$-\sum_i \left.\frac{\partial R_n^{\kappa,K+1}}{\partial x_i}\right|_p \left(x_{i,p+1} - x_{i,p}\right) = R_n^{\kappa,K+1}\left(x_{i,p}\right), \qquad \textbf{(Eq 3-6-2)}$$

where the left hand term of 3-6-1 was set to zero. Using this approach, new guesses for the primary variable values at iteration (p+1) are formulated. The iteration process continues until the convergence criterion

$$\left|\frac{R_{n,p+1}^{\kappa,K+1}}{M_{n,p+1}^{\kappa,K+1}}\right| \leq \varepsilon_1 \quad , \qquad \textbf{(Eq 3-6-3)}$$

is met. The tolerance (ε) must be greater than or equal to the absolute value of the ratio of solution residual to the mass or energy magnitude of each component. If convergence occurs at the first time step for 10 consecutive time steps, the simulation terminates. Conversely, if convergence fails for a prescribed number of iterations, the simulation is considered "non-convergent" and also terminates. If neither condition occurs, the TOUGH2 simulation proceeds until the simulation time reaches the prescribed maximum time. For more complete details, the reader is referred to Pruess (1999).

3.7 TOUGH2 SUMMARY

TOUGH2 is a numerical simulator for nonisothermal, multiphase, multicomponent fluid systems of one, two, or three dimensions in porous and fractured media. Mass and energy balance equations are approximated using an integral finite volume approach (Edwards, 1972; Narasimhan and Witherspoon, 1976), and solved in time using a fully implicit method. The equation of state calculates secondary variables at each iteration using primary variable values. The Newton-Raphson method is employed to iteratively solve for primary variable values. The iteration procedure occurs at each time step until the solution imbalance falls below the set tolerance. Once the solution tolerance is met TOUGH2 increments to the next time step. This process repeats until the completion of the simulation.

CHAPTER 4: CO_2 EQUATION OF STATE

4.1 EOS INTRODUCTION

The CO_2 equation of state (EOSCO2) used in this study was developed at The New Mexico Institute of Mining and Technology and is described in detail by (Cole, 1999). The equation of state provides the secondary variables used in TOUGH2 to calculate the mass and energy. In this equation of state, CO_2 is simulated either as aqueous dissolved phase or as a separate phase in a gas or supercritical state, depending on thermodynamic conditions. The effects of other chemical species on the thermophysical variables have not yet been determined. Future versions of the equation of state should incorporate the effects of a brine solution.

4.2 PRIMARY VARIABLES

In other TOUGH2 equation of state modules (Pruess, 1999), the appropriate choice of primary variables depends on the number of fluid phases. For example, a two-component system of CO_2 and H_2O requires three primary variables to constrain the system. Pressure and temperature are logical choices of primary variables evident by their presence in most constitutive equations. For a volume element containing only one phase, the third primary variable is the mass fraction of one component, since the total mass fraction of each component in all phases is constrained to unity. For two-phase flow, the saturation

of one phase must be used. Previous equation of state modules (Pruess, 1999) used a variable switching technique, changing variables based on the number of phases present in each volume cell. Cole (1999) reported convergence problems associated with the variable switching method. Weir et al. (1996) also reported similar convergence problems. To mitigate these convergence problems, Cole's (1999) CO_2 equation of state was developed to incorporate four persistent primary variables: pressure, temperature, saturation of separate phase CO_2, and dissolved mass fraction of CO_2. These persistent primary variables satisfy the requirements of the constitutive relations used to calculate all secondary variables in both single and multiphase systems. In this manner no variable switching is necessary.

4.3 INTERPHASE MASS TRANSFER

In all previous versions of TOUGH2, decision criteria were specified to invoke phase transitions dictated by the equation of state. The use of four persistent primary variables to define the system renders the previous system of TOUGH2 phase transitions meaningless. Declaring four primary variables allows separation of the CO_2 components in each phase. This allows for separate mass balancing of each CO_2 component. The method of adding an additional primary variable requires additional iterations to achieve solution convergence. However, in light of solution convergence problems with the variable switching technique, the persistent variable method proved more robust (Cole, 1999).

4.4 THERMOPHYSICAL PROPERTIES

All secondary variables are evaluated by the CO_2 equation of state, including specific density, specific enthalpy, dynamic viscosity, relative permeability, and capillary pressure, through constitutive relations based on the four persistent primary variables. In general the CO_2 equation of state is valid for pressures ranging from .1 MPa to 100MPa, and temperatures ranging from 15°C to 200°C, covering most of the typical reservoir conditions. Thermophysical variables are calculated for pure water, separate phase CO_2, and aqueous CO_2 mixtures.

4.4.1 PURE WATER

The International Steam Tables (International Formulation Committee, 1967) are employed to calculate thermophysical properties of pure water as functions of temperature and pressure. Representative plots of each pure H_2O thermophysical variable can be found in Cole et al. (1999).

4.4.2 GASEOUS/SUPERCRITICAL CO_2

This subsection summarizes thermophysical properties of gaseous/supercritical CO_2 under representative reservoir conditions. These properties include density, enthalpy, and dynamic viscosity, calculated as constitutive functions of pressure and temperature. Additionally, relationships for the compressibility factor for gaseous/supercritical CO_2 are developed in this subsection. For a complete summary and parameter specifications see Cole (1999).

4.4.2.1 Specific Density

Properly characterizing pure gas density requires understanding the relationship between volumetric fluid behavior as a function of temperature and pressure. Based on Van der Waals equation, Weir et al. (1996) developed a pressure (P) and temperature (T) dependent density relationship given by

$$P = \frac{RT(1+y+y^2-y^3}{\nu(1-y)^3} - \frac{c(t)+\frac{d(T)}{\nu}+\frac{e(T)}{\nu^2}+\frac{f(T)}{\nu^3}}{\sqrt{T\nu(\nu+b)}} \qquad y = b/4\nu \cdot \qquad \textbf{(Eq 4-4-1)}$$

The above equation is solved for the molar density (ν) and converted to mass density in EOSCO2. Weir (1996) developed second order polynomial curve fit functions c, d, e, and f,

$$\begin{aligned} c(T) &= c_1 + c_2T + c_3T^2 \\ d(T) &= d_1 + d_2T + d_3T^2 \\ e(T) &= e_1 + e_2T + e_3T^2 \\ f(T) &= f_1 + f_2T + f_3T^2 \end{aligned} \qquad \textbf{(Eq 4-4-2)}$$

Each term is fit with three coefficients with the subscripts 1, 2, and 3 (Weir, 1996). Using this relation the density can be calculated with the primary variables pressure and temperature.

4.4.2.2 Compressibility Factor

Derived from the ideal gas law, Reid et al. (1987) developed an expression for the

compressibility of CO_2 gas given by

$$Z = \frac{1 + y + y^2 - y^3}{(1-y)^3} - \frac{a(P,T)}{RT^{1.5}(\nu + b)} \quad \text{and} \quad a(P,T) = c(T) + \frac{d(T)}{\nu} + \frac{e(T)}{\nu^2} + \frac{f(T)}{\nu^3}, \quad \textbf{(Eq 4-4-3)}$$

where the compressibility factor (Z) is a function of the molar density (ν) and temperature (T).

A comparison between the IUPAC values (tabulated in Angus et al., 1976) to those of Cole (1999) reveals strong agreement at nearly all pressures and temperatures. As with the molar density the compressibility factor also depends on pressure and temperature.

4.4.2.3 Specific Enthalpy

Following Weir et al. (1996), the enthalpy of CO_2 is determined using residual properties. A residual fluid property is defined as the difference between the real fluid property value at the temperature and density of the fluid and the perfect gas state property value at a reference temperature (T_{ref}) and pressure (P_{ref}) (Patel and Eubank, 1988). This relation is represented as

$$H - H^*_{ref} \equiv H(T, \rho) - H^*\left(T_{ref}, \frac{P_{ref}}{RT_{ref}}\right), \quad \textbf{(Eq 4-4-4)}$$

where the enthalpic residual from the reference state ($H - H^*_{ref}$) is calculated as the

residual between the enthalpy at the specified temperature and density, and the enthalpy at the reference temperature (H^*) and molar density (calculated through an ideal gas law relation (P/RT)). Following Patel and Eubank (1988), the reference states molar enthalpy, H^*_{ref}, is chosen to equal zero at $T_{ref} = 273.16\ K$ and $P_{ref} = 1000\ Pa$. Using the integration method prescribed by Patel and Eubank, (1988), (Eq. 4-4-4) reduces to

$$\frac{H - H^*_{ref}}{RT} = (A) + (B) + Z - \frac{T_{ref}}{T} \quad . \qquad \textbf{(Eq 4-4-5)}$$

The abbreviated expressions "A" and "B" correspond to the multi-order polynomial functions shown below from Angus et al. (1976)

$$\frac{1}{12b^4RT^{1.5}}\left[\begin{array}{l} b^3\rho\left(-18d_1 - 6d_2T + 6d_3T^2\right) + b^2\rho\left(18e_1 + 6e_2T - 6e_3T^2\right) + \\ b\ \rho\left(-18f_1 - 6f_2T + 6f_3T^2\right) + b^3\rho\left(-9e_1 - 3e_2T - 3e_3T^2\right) + \\ b^2\rho^2\left(-9f_1 - 3f_2T - 3f_3T^2\right) + b^3\rho^3\left(-9e_1 - 3e_2T - 3e_3T^2\right) + \\ \ln(1+b\rho)\left[\begin{array}{l} b^3\left(-18c_1 - 6c_2T + 6c_3T^2\right) + b^2\left(18d_1 + 6d_2T + 6d_3T^2\right) + \\ b\left(-18e_1 - 6e_2T + 6e_3T^2\right) + \left(18f_1 + 6f_2T - 6f_3T^2\right) \end{array}\right] \end{array}\right], \qquad \textbf{(Eq 4-4-6)}$$

and

$$\gamma_o - 1 + \frac{T_{ref}}{T}(1-\gamma_0) + \frac{\beta\gamma_1}{T}\ln\left(\frac{T}{T_{ref}}\right) + \frac{\beta^2\gamma_{21}}{T}\ln\left(\frac{1}{T_{ref}} - \frac{1}{T}\right) + \frac{\beta^3\gamma_3}{2T}\ln\left(\frac{1}{T^2{}_{ref}} - \frac{1}{T^2}\right) +$$
$$\frac{\beta^4\gamma_4}{3T}\ln\left(\frac{1}{T^3{}_{ref}} - \frac{1}{T^3}\right) + \frac{\beta^5\gamma_5}{4T}\ln\left(\frac{1}{T^4{}_{ref}} - \frac{1}{T^4}\right) + \frac{\beta^6\gamma_6}{5T}\ln\left(\frac{1}{T^5{}_{ref}} - \frac{1}{T^5}\right) + \qquad \textbf{(Eq 4-4-7)}$$
$$\frac{\beta^7\gamma_7}{6T}\ln\left(\frac{1}{T^6{}_{ref}} - \frac{1}{T^6}\right)$$

respectively. These relations reveal how enthalpy depends on the primary variables

temperature and fluid density.

4.4.2.4 Dynamic Viscosity

Total dynamic viscosity is expressed by the summation of three viscosity components as

$$\eta(\rho,T)=\eta_0(T)+\Delta\eta_c(\rho,T)+\Delta\eta(\rho,T), \qquad \textbf{(Eq 4-4-8)}$$

where η_o is the zero limit density arising from two body molecular interactions, $\Delta\eta_c$ contribution of critical point enhancement from long range fluctuations near the critical point, and $\Delta\eta$ is all other processes. This representation, from Vesovic et al. (1990) is valid for pressures up to 300 MPa for temperatures ranging from 200 to 1000 K, and for pressures up to 30 MPa for temperatures ranging from 1000 to 1500 K. The first term in (Eq 4-4-8) is the zero limit density produced from two body molecular interactions and is given by

$$\eta_0(T)=\frac{1.00697\sqrt{T}}{\psi_\eta^*(T^*)}, \quad \ln\psi_\eta^*(T^*)=\sum_{i=0}^{4}a_i(\ln T^*)^i \ , \qquad \textbf{(Eq 4-4-9)}$$

which is a function of temperature and the effective reduced cross section (φ) across molecules. In this case a_i is coefficient ranging from 1 to 4 (Vesovic et al.1990).

The $\Delta\eta_c(\rho,T)$ term represents the critical point contribution, which is neglected because it applies over a short temperature-pressure range and requires significant computational expense (Cole, 1999). The remaining term represents all remaining viscosity influences

that are not associated with the viscosity contributions of critical point enhancement or near body collisions, expressed by

$$\Delta\eta(\rho,T) = d_{11}\rho + d_{21}\rho^2 + \frac{d_{64}\rho^6}{T^{*3}} + d_{81}\rho^8 + \frac{d_{82}\rho^8}{T^*}\ , \qquad \textbf{(Eq 4-4-10)}$$

where $d_{\#}$ is a coefficient fit to the polynomial equation. This bulk term includes the contributions of many-body collisions, molecular-velocity correlations, and collisional transfer (Vesovic et al., 1990).

4.4.3 AQUEOUS H_2O/CO_2 MIXTURES

In this subsection we summarize the relationships employed to calculate the thermophysical properties of aqueous mixtures of H_2O and CO_2 necessary to characterize the flow of such mixtures in the subsurface.

4.4.3.1 Solubility

CO_2 partitioning between the dissolved and separate phases is described by a modified form of Henry's law (Reid et al., 1987). Reid et al. (1987) showed that the mole fraction of the gaseous solute in aqueous solution is reasonably approximated as a function of the fugacity, pressure, and temperature shown by

$$\ln\left(\frac{f}{X_2}\right) = \ln H_{2,1}^{P_{vp1}} + \frac{\overline{V}_2^{\infty}\left(P - P_{vp1}\right)}{RT}\ , \qquad \textbf{(Eq 4-4-11)}$$

where the natural log of the ratio of fugacity (*f*) to mole fraction (X) is equal to the natural log of enthalpy (H) plus a modified ideal gas law factor. The factor term is the product of the molar volume at infinite dilution (V^{∞}) and the difference between the ambient system pressure and the vapor pressure at the prevailing temperature ($P-P_{vp}$). Equation (Eq 4-4-11) is an equilibrium relationship, where kinetics of CO_2 phase transfer are not explicitly defined between time steps. Development of a rate conversion function has been created in this study to define the kinetics during each TOUGH time step. To eliminate phase flashing, equation (Eq 4-4-11) is converted into a rate dependent function given by

$$R_p = K_r(T)\left[\exp\left(\ln\frac{f_2}{H_{2,1}^{P_{vp1}}} - \frac{\overline{V}_2^{\infty}\left(P-P_{vp1}\right)}{RT}\right) - X_2\right], \qquad \textbf{(Eq 4-4-12)}$$

where the CO_2 mass conversion rate (R_p) depends on the degree to which the system is in equilibrium. At equilibrium the bracketed term becomes zero, and the rate of mass transfer between phases also becomes zero (instantaneous transfer). The actual CO_2 mass conversion rate is likely a function of the phase transition interface area, molecular path interface area, and molecular path lengths that implicitly affect the rate multiplier (K_r) (Lichtner, personal communication, 2001). The CO_2 phase transition rate may also be a function of the disequilibrium or the degree to which the system falls out of agreement to the modified Henry's law relationship (Lichtner, personal communication, 2001). This may promote more realistic transfer rates in for small time steps where systems could not reasonably reach equilibrium. The rate factor (K_r) can be interpreted as an effective rate

constant, K_r is temperature dependent, and may be scaled by the Peclet, Sherwood, or Damkoehler numbers, to predict diffusion across the CO_2-H_2O interface (Lichtner, personal communication, 2001). The extent that the interfacial area depends on saturation may depend on the wetting characteristics of the phases, as different wetting characteristics may produce unique saturation-interfacial area relationships. Water should wet the rock surface with more CO_2 in the pore interiors. The CO_2 mass conversion rate term can be implemented to calculate the mass fraction of dissolved CO_2 given by

$$XCO2_t = R_p \Delta t + XCO2_{t-1} \quad , \qquad \textbf{(Eq 4-4-13)}$$

where the updated mass fraction of dissolved CO_2 at time t ($XCO2_t$) is equal to the change in mass for the current time step ($R\Delta T$) summed with the previous time step mass fraction ($XCO2_{t-1}$). The first term on the right hand side may be either positive or negative depending upon the direction of the phase transition. A positive conversion rate flux would indicate a flux of CO_2 to the aqueous phase, and a negative rate flux would indicate CO_2 flux to the separate phase.

This rate-limited partitioning function modified from Reid et al. (1987) has not been utilized in this study, although the programming has been completed in the CO_2 equation of state. Future laboratory experiments are needed to properly define these parameters. For this study CO2 phase transfer was linearly interpolated in TRANS between each TOUGH2 time step. However, the nonlinear relationships of most thermophysical variables raises question regarding the adequacy of a linear interpolation method if the

temperature change is large between time steps. If the temperature change is small, the linear approximation should be fairly robust Future version of the TR-T simulator should implement the rate limited transfer function that will properly define the CO_2 phase transfer kinetics under transient thermal conditions. Also, the above-described relationship for the solubility of CO_2 in water is derived for pure water. Increasing salinity decreases CO_2 solubility. For example, the solubility of CO_2 in a solution of three percent salinity is approximately 85 percent of the solubility of CO_2 in pure water (Enick and Klara, 1990). Therefore, the EOSCO2 will overestimate of the mass of CO_2 dissolved in water. Future versions of the EOSCO2 should incorporate both the effect of salinity on all thermophysical variables and the rate limited phase transfer between separate and dissolved phase CO_2.

4.4.3.2 Specific Density

The dissolution of CO_2 in water increases the density of water. Based on empirical data and theoretical considerations, Anderson et al. (1992) suggest that the molar density of aqueous mixtures of CO_2 and water (ρ_{mix}) can be approximated using

$$\rho_{mix} = \frac{\rho_{H_2O}\rho_{CO_2}^{sat}}{(1-X_{XCO_2})\rho_{CO_2}^{sat} + X_{XCO_2}\rho_{H_2O}}, \qquad \textbf{(Eq 4-4-14)}$$

where ρ_{H_2O} is the molar density of water, ρ_{CO2}^{sat} is the molar density of CO_2 at saturation pressure, and X_{CO2} is the dissolved mole fraction of CO_2. The molar density of CO_2 at saturation pressure (ρ_{CO2}^{sat}) is determined by the following relationship

$$\rho_{CO_2}^{sat} = \frac{1}{37.36 - 7.109x10^{-2}T - 3.812x10^{-5}T^2 + 3.296x10^{-6}T^3 - 3.702x10^{-9}T^4}. \quad \textbf{(Eq 4-4-15)}$$

Therefore, the density of a CO_2-H_2O mixture is estimated by the density of each phase and their relative proportions, calculated using the mass fraction of dissolved phase CO_2 term.

4.4.3.3 Specific Enthalpy

Weir et al. (1996) demonstrated that the enthalpy of aqueous mixtures of CO_2 (H_{mix}) can be approximated by the enthalpy of pure water (H_{H2O}), the specific enthalpy of CO_2 (H_{CO2}), and the specific enthalpy of solution for CO_2 (H_{sol}) given by

$$H_{mix} = (1 - X_{CO_2})H_{H_2O} + X_{CO_2}(H_{sol} + H_{CO_2}), \quad \textbf{(Eq 4-4-16)}$$

where X_{CO2} denotes the mole fraction of dissolved phase CO_2. The solution enthalpy is calculated as a polynomial function of temperature expressed as

$$H_{sol} = -0.073696x10^6 + 0.56405x10^6\left(\frac{T}{100}\right) + 0.70363x10^6\left(\frac{T}{100}\right)^2 - 0.27882x10^6\left(\frac{T}{100}\right)^3 + 0.04579x10^6\left(\frac{T}{100}\right)^4 \quad \textbf{(Eq 4-4-17)}$$

The enthalpy calculations for H_2O and CO_2 are calculated as described above in the

section on each component. Cole (1999) compared the enthalpy differences between a pure H_2O solution and a CO_2-H_2O aqueous mixture, demonstrating a moderate pressure dependency of enthalpy along five isotherms for both pure H_2O and a CO_2-H_2O solution mixture. The temperature dependency was nearly linear in all cases, with little difference between fluids.

4.4.3.4 Dynamic Viscosity

Available data suggest that the dynamic viscosity of pure water is not significantly affected by the presence of dissolved CO_2 (Cole, 1999). Therefore, the dynamic viscosity of pure water predicted from the relationship provided by the International Steam Tables (International Formulation Committee, 1967) is used to represent the dynamic viscosity of aqueous mixtures and pure water.

4.4.3.5 Capillary Pressure

Assuming insignificant fluid-solid interactions and a rigid porous medium, Parker et al. (1987) developed a scalable parametric model to describe capillary pressure as a function of wetting fluid saturation given by

$$P_c = \frac{1}{\alpha\beta_c}\left(S_w^{1/m} - 1\right)^{1/n}, \qquad \textbf{(Eq 4-4-18)}$$

where the capillary pressure (P_c) is a function of the effective wetting saturation (S_w). The

remaining terms are modified fitting parameters from Van Genuchten (1980) on scaled saturation capillary pressure relationships (Cole, 1999). The parameter values are used for supercritical CO_2 and water. Capillary pressures for gaseous CO_2 are considered negligible in the 1999 version of the equation of state. The capillary pressure functions are scaled by according to Leverett (1941) where the capillary pressure is divided by the square root of the permeability modifier (Pruess, 1999). Future versions should incorporate the capillary pressure of CO_2 in the gaseous phase.

4.4.3.6 Relative Permeability

Relative permeability equations were experimentally determined by Parker et al. (1987). CO_2 is considered to be the non-wetting phase and H_2O is the wetting phase. The relative permeability is the fraction of flow that is attributed to a particular fluid ranging from 0 to 1. Relative permeability for the wetting phase is expressed by

$$k_{rw} = \overline{S}_w^{1/2}\left(1-\left(1-S_w^{1/m}\right)^m\right)^2, \qquad \textbf{(Eq 4-4-19)}$$

where the wetting relative permeability (k_{rw}) is proportional to a power law relationship of the wetting phase saturation (S_w). The nonwetting relative permeability is expressed by a similar function where

$$k_{rnw} = (\bar{S}_t - \bar{S}_w)^{1/2}\left(\left(1 - \bar{S}_w^{1/m}\right)^m - \left(1 - \bar{S}_t^{1/m}\right)^m\right)^7 \quad \text{and} \quad \bar{S}_t = \frac{S_w + S_{nw} - S_r}{1 - S_r}. \qquad \textbf{(Eq 4-4-20)}$$

In this case the relative permeability of the nonwetting phase (k_{rnw}) is a function of both the nonwetting and wetting saturations.

4.5 EOS SUMMARY

The EOSCO2 was designed to provide secondary variables of the mass and energy balance equations, used in TOUGH2 to model the flow of CO_2 in the aqueous and separate phases. While the CO_2 equation of state provides a sound foundation on which to characterize CO_2 behavior in geologic media, future modifications to this equation of state must implement the effects of brine composition on each of the secondary variables, including not only density effects, but also modifications to all secondary variables. The degree to which the additional chemical species may alter results is most likely a function of relative concentrations. In light of this limitation, brine concentrations in all simulations are minimized to reduce the potential thermophysical effects of the interacting solute concentrations on CO_2 phase properties.

CHAPTER 5: TRANS REACTIVE TRANSPORT SIMULATOR

5.1 TRANS INTRODUCTION

TRANS solves mass conservation equations for a multicomponent multiphase geochemical system (Lichtner, 2000). TRANS is the geochemistry simulator of the coupled model FLOTRAN, and calculates homogeneous (1- phase) aqueous and heterogeneous (2 – phases) gaseous and mineral reactions. Aqueous reactions include mineralization, dissolution, ion exchange, redox, surface complexation, and sorption. Both aqueous and gaseous reactions are reversible, while mineral reactions are irreversible. In this study, flow and transport are sequentially coupled. TOUGH2 calculates flow using the equation of state for multiphase CO_2. TOUGH2 was used in lieu of the flow code FLO in FLOTRAN (Lichtner, 1999) because of the multiphase CO_2 equation of state programmed in TOUGH2 format and expanded user base.

5.2 CHEMICAL SPECIES REPRESENTATION

The mass accounting approach used in TRANS assumes that a set of independent aqueous species can fully describe the chemical system. The number of independent (primary) species (N_i) equals the difference between the total species (N_T) and the number of linearly independent reactions (N_R), or

$$N_I = N_T - N_R \quad . \qquad \textbf{(Eq 5-2-1)}$$

Primary species must be in the aqueous phase. Gas and mineral species are always defined as secondary species. The resulting reactions (N_R) for aqueous, gaseous, and mineral reactions are given by

$$\begin{aligned}
&\sum_{j=1}^{N_c} \nu_{ji}^{l} A_j \longleftrightarrow A_i^l \ldots.(i = 1,\ldots\ldots N_l) \\
&\sum_{j=1}^{N_c} \nu_{ji}^{g} A_j \longleftrightarrow A_i^g \ldots.(i = 1,\ldots\ldots N_g) \quad , \qquad \textbf{(Eq 5-2-2)} \\
&\sum_{j=1}^{N_c} \nu_{ji}^{m} A_j \longleftrightarrow M_i \ldots.(i = 1,\ldots\ldots N_m)
\end{aligned}$$

where the matrices ($\nu_{ji}^{l,g,m}$) house the stoichiometric reaction coefficient ratio denoting the number of moles of the jth primary species in one mole of secondary species (liquid A_i^l, gas A_i^g, mineral M_m).

Transport within the system may be prescribed using equilibrium reactions or kinetic rate law relationships. In both cases a stoichiometric relationship between the primary and associated secondary species is used.

5.3 MULTIPHASE-MULTICOMPONENT TRANSPORT EQUATIONS

In the absence of colloidal transport, which is not used in this study, TRANS simulates reactive transport for a set of prescribed primary species described by

$$\frac{\partial}{\partial t}\left[\phi\psi_j + \sum_m \bar{C}_j^m\right] + \nabla\cdot\Omega_j = -\sum_r \nu'_{jm} I_m + \sum_r \nu'_{jk} I_k \quad . \qquad \textbf{(Eq 5-3-1)}$$

The transient term (left-hand side) represents total aqueous concentration, as well as sorption to the matrix surface. The total primary species accumulation is represented by (ψ_j), or

$$\psi_j = s_l \psi_j^l + s_g \psi_j^g \quad , \quad \psi_j^{l,g} = \delta C_j + \sum_{i=1}^{N_{l,g}} \nu_{jl,g} C_i \quad , \qquad \textbf{(Eq 5-3-2)}$$

where the total primary species equals the cumulative sum of the gas (ψ^g_j) and liquid (ψ^l_j) concentrations multiplied by their respective saturations (S).

The second component in the transient term in the TRANS governing equation represents sorption given by

$$\sum_m \bar{C}_j^m \quad , \qquad \textbf{(Eq 5-3-3)}$$

where the concentration of total primary sorbed species ($\bar{C}_j^m$) equals the summation of the component concentrations sorbed to each mineral (m).

The solute flux term of the TRANS mass balance equation (5-3-1) accounts for solute transport due to advective and diffusive processes. The diffusive flux component of dispersion is assumed Fickian. The total flux (Ω) consists of individual flux components of each fluid phase (liquid (Ω_l) and gas (Ω_g)) as shown by

$$\Omega_j = \Omega_j^l + \Omega_j^g \quad . \qquad \textbf{(Eq 5-3-4)}$$

The individual fluxes include both the advective and dispersive components of each phase given by

$$\Omega_j^{l,g} = \delta J_j^{l,g} + \sum_{i=1}^{N_{l,g}} v_{ji} J_i^{l,g} \qquad \textbf{(Eq 5-3-5)}$$

where

$$J = q\psi_j - \tau\phi s D \nabla\psi_j \quad . \qquad \textbf{(Eq 5-3-6)}$$

The cumulative flux component for each primary species is equal to the sum of the individual primary species and its secondary liquid, gas, and mineral species. The advective and dispersive flux is represented by J. The advective component is calculated using Darcy's law for multiphase flow

$$q_{l,g} = -\frac{k k_{rl,rg}}{\mu_{l,g}} \nabla\left(P_{l,g} - \rho_{l,g} g z\right) . \qquad \textbf{(Eq 5-3-7)}$$

Using Darcy's Law, the advected mass of primary species j is calculated as the product of the concentration and fluid flux. However, in coupled mode TOUGH2 calculates the flux. The accompanying dispersive term consists of the traditional Fickian diffusion coefficient and a tortuosity parameter.

The source-sink terms of the TRANS governing equation represent species transfer for kinetic reactions. The mineralization transfer term is given by

$$\sum_r \nu_{jm} I_m \,, \qquad \textbf{(Eq 5-3-8)}$$

which is the summation of the stoichiometric ratio (ν) and the kinetic rate (I) of each fluid-mineral reaction.

Likewise the gaseous and liquid speciation that is kinetically controlled is modeled as the summation of the product of the stoichiometric ratio and the rate of reaction for each respective species, and is expressed as

$$\sum_r \nu_{jk} I_k \,. \qquad \textbf{(Eq 5-3-9)}$$

In summary, there are two methods by which a chemical reaction may occur. The first method employs an equilibrium reaction that incorporates an equilibrium constant and assumes that the system is in local equilibrium. The second method uses a kinetic rate,

where the mass transfer is depends on a rate constant. The transport equations rely on chemical mass balances of primary species, which define the chemical system.

5.4 CHEMICAL REACTIONS

5.4.1 EQUILIBRIUM REACTIONS

Mass action equations assume chemical equilibrium and employ equilibrium constants to determine the concentration of each species. A temperature dependent equilibrium constant equals the activity ratio of the products over the reactants, where each activity is raised to the power of its stoichiometric coefficient. Two thermodynamic databases store all reactions used in TRANS. Both databases have been modified from the EQ3/6 database (Wolery, 1983). An isothermal database contains equilibrium constants at the standard temperature of 25°C. The nonisothermal database applies over a temperature range of 0-300°C. Equilibrium constants (K) are stored at temperatures (T) of .01, 25, 60, 100, 150, 200, 250, and 300°C and interpolated using a Mayer-Kelly function given by

$$\log K(T) = \frac{a_2}{T^2} + \frac{a_1}{T} + a_0 \ln T + a_1 + a_2 T \quad . \qquad \textbf{(Eq 5-4-1)}$$

The Mayer-Kelly function provides a fit to the tabulated temperatures at any specified temperature. TRANS employs the equilibrium constant to calculate the distribution of each species in a particular reaction. The equilibrium constants enter the mass action equations for aqueous and gaseous species, and minerals given by,

Aqueous: $$C_i^l = \rho_l^{\alpha l-1}\left(\gamma_i^l\right)^{-1} K_i^l \prod_{j=1}^{N_c}\left(\gamma_j^l C_j^l\right)^{\nu_{ji}^l}, \quad \textbf{(Eq 5-4-2)}$$

Gas: $$C_i^g = \frac{K_i^g}{RT} K_i^l \prod_{j=1}^{N_c}\left(\gamma_j^l C_j^l\right)^{\nu_{ji}^g}, \quad \textbf{(Eq 5-4-3)}$$

Mineral: $$K_m \prod_{j=1}^{M}\left(\gamma_j C_j^l\right)^{\nu_{jm}} = 1 \ , \quad \textbf{(Eq 5-4-4)}$$

where the concentration of each species is calculated by solving for the respective species from the mass action equations with the associated equilibrium constant (K). The gaseous term relates the mass from an ideal gas law. The activity is calculated using the extended Debye-Huckel relation

$$\log\gamma_i = -\frac{z^2 A\sqrt{I}}{1+Ba\sqrt{I}} + bI \quad , \quad \textbf{(Eq 5-4-5)}$$

where the log of the activity (γ) is a function of the ionic charge (z) and ionic strength (I).

5.4.2 KINETIC REACTIONS

As described above the chemical system can be modeled either as equilibrium or kinetically driven for each species and for different phases. The kinetic homogeneous aqueous reaction rate is described by

$$I_k = k_k \prod_{\nu_{jk}>0} \left(\gamma_j C_j\right)^{\nu_{jk}} \left[1 - \frac{K_k}{Q_k}\right], \quad Q_k = \prod_j \left(\gamma_j C_j\right)^{\nu_{jk}}, \qquad \textbf{(Eq 5-4-6)}$$

where the reaction rate (I) of the aqueous reaction is a function of the degree to which the system is out of chemical equilibrium. Q represents the ion activity product, which is a proportion of the equilibrium constant and a measure the equilibrium of the system. Note that the bracketed term vanishes to zero at equilibrium when the ion activity product is equal to the equilibrium constant consistent with zero net reaction rate at equilibrium.

The transport limited mineralization rate (I_j) assumes similar mathematical formulation as that of the aqueous rate function given by

$$I_j = -\sum_l \mathrm{P}_{jl} k_{jl} \left[1 - K_j Q_j\right] \text{ where } Q_j = \left(a_j^j\right)^{-1} \prod_{j=1}^{nc} \left(\gamma_j^l C_j\right)^{\nu_{jl}}. \qquad \textbf{(Eq 5-4-7)}$$

The transport limited reaction rate (I_j) is based on the assumption of local equilibrium in which the kinetic rate law is replaced by the mass action equation. The prescribed kinetic rate is represented by k. Note that when the ion activity product term is zero the equation reduces to the sum of the prefactor-prescribed rate constant expression summed over the lth parallel chemical reaction within the system.

5.5 METHOD OF SOLUTION

TRANS uses an integral finite volume scheme, similar to TOUGH2, to numerically

approximate the chemical system prescribed in a simulation. Various options of solution algorithms are available, including implicit, explicit, and operator-splitting finite difference methods. Either a tri-diagonal or conjugate gradient solver WATSOLV (Van der Kwaak et al., 1995) may be selected for the implicit scheme, depending on the problem. (Lichtner, 2000). The operator splitting scheme is also available for larger problems. To be consistent in the couple TR-T model we employed an implicit scheme for both TOUGH2 and TRANS

5.6 TRANS SUMMARY

TRANS can simulate multicomponent, multiphase, nonisothermal, reactive transport for 1-, 2-, or 3-dimensional spatial domains. TRANS' modeling capabilities include ion exchange, sorption, mineralization, dissolution, and solute and colloidal transport. A tridiagonal or conjugate gradient solver is used with an implicit, explicit, or operator-splitting scheme. Within the TR-T model developed in this study, TRANS uses the coupled flow variables provided by TOUGH2 to calculate the reactive chemistry within the simulated geologic system.

CHAPTER 6: DRIVER PROGRAM

6.1 DRIVER INTRODUCTION

A driver program, created in this study, couples executions in the TR-T simulator (Figure 6-1). Its main function is to sequentially couple TRANS with TOUGH2-EOSCO2. Under

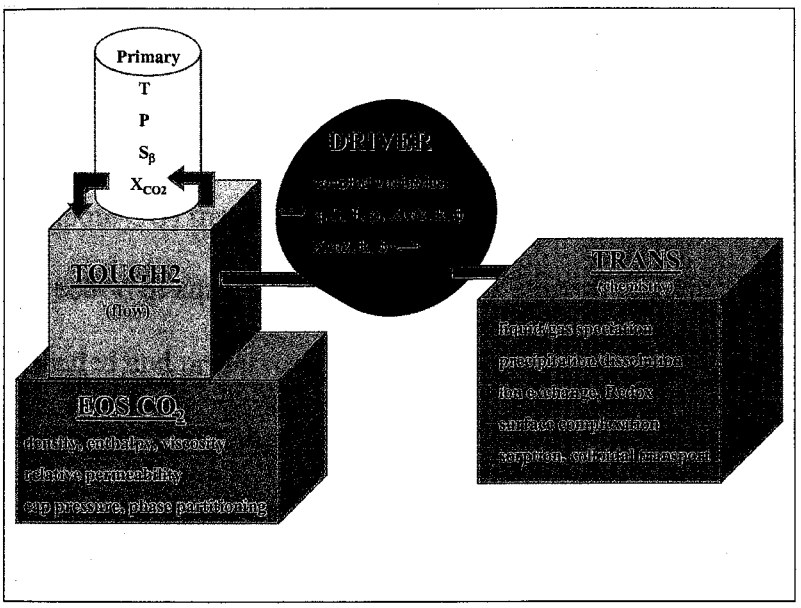

Figure 6-1: Flow control of the TR-T model. Coupled variables (velocities, saturations, temperature, densities, dissolved CO_2) are passed to TRANS. TRANS in turn return the changes to the matrix (porosity and absolute permeability).

this numerical scheme TOUGH2-EOS and TRANS operate independently but are linked through coupled variables updated at every time step within the driver program (Figure 6-1). TOUGH2 calculates mass and energy flow. At the convergence of each

flow time step, the driver program transfers coupled flow variables to TRANS through driver. TRANS simulates the simulates the chemical reactions from the previous (TOUGH2) time step and then in turn updates variables affected by reactive transport in TOUGH2 via the driver. This process repeats until the end of the TR-T simulation.

Required error testing for the TR-T model is minor. Internal functions are unchanged in both TOUGH2 and TRANS, allowing each simulator to operate independently. Lichtner (2000) created the sequentially coupled model FLOTRAN and programmed TRANS to operate in coupled mode with the flow simulator FLOW. As a result, the internal functions of TRANS have been restructured to operate in a sequentially coupled mode. The driver program couples TRANS to TOUGH2 in a similar manner, with the addition of coupling the dissolved mass fraction of CO_2. Since both TRANS and TOUGH2 compute CO_2 transport, potential error in the TR-T model may arise when simulating the advection of aqueous CO_2. Test results suggest that the TR-T model is operating as intended and preserves mass of all species in all phases. In addition to model testing, this chapter describes the driver program structure and the coupled variables in each simulator.

6.2 COUPLED VARIABLES

Coupled variables were identified by comparing the governing and constitutive equations present in TRANS to those in TOUGH2. The coupled variables are:

- Temperature
- Liquid and gas velocity
- Liquid and gas saturation

- Liquid and gas density
- Dissolved phase CO_2
- Absolute permeability
- Porosity

Provided below is a mathematical description identifying each coupled variable within the TR-T model. The variable notation for each simulator has been preserved, matching both the operator manuals and section descriptions in this publication. The equations are presented in a hierarchical structure, beginning with the governing equation of each simulator and then expanding all individual terms necessary to reveal the coupled variables. First the equations of TOUGH2 are presented, followed by equations employed in the TRANS simulator.

6.2.1 TOUGH2 COUPLED VARIABLES

Rather than refer the reader to the appropriate equations detailed in earlier chapters, the equations are reprised here for convenience. The coupled variables are identified first and briefly discussed after the equations are summarized.

We expanded the appropriate terms from the TOUGH2 governing equation to reveal the roles of each coupled variable. The governing equation for advective mass or energy flow in TOUGH2 is represented by

$$\frac{d}{dt}\int_{V_n} M_{mass,energy}{}^{\kappa}\, dV_n = \int_{\Gamma_n} F^{\kappa} \bullet N d\Gamma_n + \int_{V_n} q^{\kappa}\, dV_n \,, \qquad \textbf{(Eq 6-2-1)}$$

where M is the mass or energy per unit volume (V) of component κ, t is time, $F \cdot N$ is the inward normal flux over the surface area (Γ) for cell n, and q is a volume normalized source-sink term Pruess (1999). The left hand term represents the accumulation of volume normalized mass or energy within each grid cell. The volume averaged mass is represented by

$$M_{mass}^{\kappa} = \phi \sum_{\beta=l,g} S_\beta \rho_\beta X_\beta^\kappa \qquad \textbf{(Eq 6-2-2)}$$

a function of porosity (ϕ), saturation (S), density (ρ), and mass fraction (X) of each fluid phase (β). The energy term represents the sum of the energy of the fluid and geologic media and is given by

$$M_{energy}^{\kappa} = (1-\phi)\rho_r C_r T + \phi \sum_{\beta=l,g} S_\beta \rho_\beta u\left(H(T,\rho)\right)_\beta \qquad \textbf{(Eq 6-2-3)}$$

The matrix energy storage term is a function of the specific heat of the rock (C_r) and the density and temperature. The pore fluid energy storage term is a function of the saturation, density, and specific internal energy (u), also a function of temperature (T).

The component mass flux is calculated by the summation of all mass and energy fluxes in each phase (F) through the relation

$$F^{\kappa} = \sum_{\beta=l,g} X_\beta^\kappa F_\beta^\kappa , \qquad \textbf{(Eq 6-2-4)}$$

which expresses a summation of the mass fraction (X) of each component for each phase multiplied by the corresponding fluid flux of each phase for each component (F_β^κ). Each fluid flux is calculated using Darcy's law for multiphase flow given by

$$F_\beta = -k\frac{k(S_\beta)_r}{\mu(P,T)_\beta}\rho_\beta(\nabla P_\beta - \rho_\beta g) \qquad \textbf{(Eq 6-2-5)}$$

that depends on intrinsic permeability(k), relative permeability ($k(S_\beta)_r$) as a function of the phase saturation, viscosity ($\mu(P,T)_\beta$) as a function of the pressure and temperature, fluid density, and the flow potential term $(\nabla P_\beta - \rho_\beta g)$. In addition to mass transport, the fluid flux described above is also used to calculate the total energy flux given by

$$F^\kappa = -\lambda\nabla T + \sum_{\beta=l,g} H(T,\rho)_\beta F_\beta \quad , \qquad \textbf{(Eq 6-2-6)}$$

where the energy flux for each component (F^κ) is composed of both a conductive (first right-hand side term) and convective term (second left-hand side term). Thermal conductivity (λ) in the conductive term depends on fluid saturation for the respective phase and rock type. Ethalpy (H) in the convective term, varies as a function of temperature and density.

Temperature is present in the equations for enthalpy, dynamic viscosity, and heat conduction. Saturation is present in the equations for conduction, convection, relative

permeability, and the mass and energy fluxes. Density is present in the equation for enthalpy, and mass and energy fluxes. Porosity is present in both the mass and energy flux terms. The mass fraction of dissolved CO_2 is employed in the total flux equation. In summary, the roles of each coupled variable in TOUGH2 has been identified. The next step is to verify the presence of the coupled variables in the TRANS set of equations.

6.2.2 TRANS COUPLED EQUATIONS

The TRANS governing chemical mass balance equation is given by

$$\frac{\partial}{\partial t}\left[\phi S_l \psi_l + \sum_m \bar{C}_j^m\right] + \nabla \cdot \Omega_l = -\sum_r \nu'_{jm} I_m + \sum_r \nu'_{jk} I_k \,, \qquad \textbf{(Eq 6-2-7)}$$

where the accumulation of each primary chemical species equals the flux of the respective species plus a source-sink from kinetic and mineral precipitation-dissolution reactions. The accumulation term is the summation of all aqueous and mineral species written in terms of a set of primary variables ($\phi S_l \psi_l$) and the summation of the sorbed species ($\sum_m \bar{C}_j^m$). Expanding the inner terms of the general flux (Ω) in the TRANS governing equation leads to

$$\frac{\partial}{\partial t}\left[\phi S_l \psi_l + \sum_m \bar{C}_j^m\right] + \nabla \cdot \left(\left(-\phi \tau S_l \; D_l \nabla C_j^l + q_l C_j^l\right) + \sum_{i=1}^{N_l} \nu_{ji}^l \left(-\phi \tau S_l \; D_l \nabla C_i^l + q_l C_i^l\right)\right) = -\sum_r \nu'_{jm} I_m + \sum_r \nu'_{jk} I_k \,. \qquad \textbf{(Eq 6-2-8)}$$

Note the presence of porosity, fluid saturation, and velocity (q) in this flux equation, common with the TOUGH2 equations. The generalized flux term is the summation of the primary variable component fluxes and the associated secondary variables written in terms of the primary variables. Within the generalized flux term the dispersive flux is a function of the porosity, tortuosity (τ), saturation, Fickian diffusion coefficient (D), and the concentration gradient. The total generalized flux is the summation of the diffusive and advective solute fluxes, shown as a function of the fluid velocity and concentration. Expansion of the primary species concentration term (C) yields

$$\frac{\partial}{\partial t}\left[\phi S_l \psi_l + \sum_m \bar{C}_j^m\right] + \nabla \cdot \left(\left(-\phi\tau S_l \; D_l \nabla C_j^l + q_l C_j^l\right) + \sum_{i=1}^{N_l} \nu_{ji}^l \begin{pmatrix} -\phi\tau S_l \; D_l \left(\rho_l^{\alpha l - 1} \left(\gamma_i^l\right)^{-1} K_i^l \prod_{j=1}^{N_c} \left(\gamma_i^l C_j^l\right)^{\nu_{ji}^l} \right) \\ + q_l \left(\rho_l^{\alpha l - 1} \left(\gamma_i^l\right)^{-1} K_i^l \prod_{j=1}^{N_c} \left(\gamma_i^l C_j^l\right)^{\nu_{ji}^l} \right) \end{pmatrix} \right), \quad \textbf{(Eq 6-2-9)}$$

$$= -\sum_r \nu_{jm}^{'} I_m + \sum_r \nu_{jk}^{'} I_k$$

and includes density and saturation terms contained within the generalized flux (Ω). The expanded concentration terms are calculated as the product of the porosity, tortuosity, diffusion coefficient, and the equivalent primary species concentration. The equivalent primary species concentration comprises the contribution of all species written in term of the primary variables through a stoichiometric coefficient (γ) and the equilibrium constant (K). The porosity term is separately updated according to the reactive chemical processes between the fluid and geologic media. As a result of the variable porosity, the permeability is modified. Accordingly, changes in porosity are linked to the intrinsic permeability through a prescribed power law given by

$$k_t = \left(\frac{n_t}{n_0}\right)^{\beta} \cdot k_0 \quad , \qquad \textbf{(Eq 6-2-10)}$$

where the current permeability (k_t) is related to the initial permeability (k_0) through a permeability modifier term ($\left(\frac{n_t}{n_0}\right)^{\beta}$). The modifier term is a function of the ratio of current (n_t) to initial porosity (n_0) through a power law relationship of order β.

The variables common to TOUGH2 and TRANS are temperature, liquid and gas velocity, liquid and gas saturation, liquid and gas density, dissolved phase CO_2, absolute permeability, and porosity. A simple expansion of the TRANS governing equation reveals the role of each coupled variable, except temperature. Temperature is not explicitly present in the TRANS expanded governing equation, but rather is coupled through chemical equilibrium reaction constants that are functions of temperature. Saturation is employed in the accumulation term (to covert molality to molarity) and in generalized flux term. Porosity is present in the accumulation and generalized flux term, while density and velocity are coupled solely through the generalized flux term. The concentration of aqueous CO_2 in TRANS is present in the generalized flux term and is converted to mass fraction of dissolved CO_2 in TOUGH2.

In summary, the role of each coupled variable in the TR-T simulator was identified. The driver program passes the flow variables from TOUGH2 to TRANS. TRANS employs the coupled flow variables to calculate reactive transport, updating the dissolved mass fraction of CO2, permeability modification, and porosity in TOUGH2 for the next time step.

6.3 COUPLED MODEL STRUCTURE

The TR-T model simulates flow and reactive transport of mass and energy in a nonisothermal, multicomponent, multiphase system. Individually, TRANS simulates reactive chemistry in the aqueous and mineral phases, and TOUGH2 simulates transport of mass and energy in both aqueous and gas phases. The heterogeneous phase partitioning between CO_2(g) and CO_2(aq) is calculated in EOSCO2 using a modified Henry's law relation by Reid et al. (1987). Thus, CO_2 partitioning between the gas and aqueous phases is simulated in TOUGH2. Gas diffusion is ignored, but since CO_2 is usually in a supercritical state under deep basin conditions, ignoring gas diffusion will have insignificant effects on simulator results. Advective fluxes are calculated in TOUGH2 and the driver program passes these values to TRANS at each time step. Supercritical CO_2 advection and gas saturation terms are employed in TRANS to calculate non-reactive gas advection. Both the diffusive and advective fluxes in the aqueous phase may be calculated for a multi-component, chemically reactive system. Processes such as mineralization, dissolution, colloidal transport, and sorption may change the aqueous and mineral concentrations of each species during a simulation. In addition, CO_2 transport is simulated in both TRANS and TOUGH2, providing opportunity for minor discrepancies in the distribution of dissolved phase CO_2. In addition, dispersive fluxes are simulated in TRANS. To neglect possible inconsistencies in CO_2 transport between the two simulators and to account for potential chemical sources or sinks of CO_2 in TOUGH2, CO_2 aqueous transport calculated by TRANS supersedes that by TOUGH2 in the TR-T model. Once the TRANS simulation reaches

the current TOUGH2 time step, the updated CO_2 aqueous concentrations and reactive variables are updated in TOUGH2 for the next time step. In this coupling formulation, aqueous CO_2 is simulated in both TRANS and TOUGH2, while all other species and subsequent reactions with the geologic media are simulated solely by TRANS. In summary, the TR-T model combines the attributes and functions of TOUGH2 and TRANS, creating a multicomponent multiphase reactive transport model for CO_2 injection in geologic media

6.4 ORGANIZATION

The method of coupling is a key consideration. Fully coupled models are usually more accurate than semicoupled models but with a significant cost in computation time (Yeh and Tripathi, 1989). For two models to be fully coupled, the chemistry, mass, and energy balance equations must be simultaneously solved. This method affects computation time, as both the flow and reactive transport must be solved at each iteration. For many systems semi-coupled models can produce accurate results and the added computational cost may be avoided (Lichtner et. al., 1996). In addition, when using a sequentially coupled approach the individual code structures of each model are preserved, avoiding possible operational errors associated with code modifications. Lichtner (1999) linked TRANS to the flow simulator FLOW using a sequentially coupled approach. Since time constants of chemical reactions are often much smaller than those in flow processes, TRANS time steps are often much smaller than FLOW time steps (Lichtner, 2000). In such cases, coupled FLOW variables are linearly interpolated according to the proportion of the time step in TRANS to the time step taken by FLOW. For the driver program developed in

this study, a sequentially coupled approach was also employed to couple TOUGH2 and TRANS. All variables discussed above that are common to each simulator are coupled. Beginning at each time step TOUGH2 runs to convergence, passing updated flow variables to the driver program. TRANS accepts the coupled variables through the driver program. Repeating the previous TOUGH2 time step, TRANS calculates the changes in chemistry and subsequent changes in porosity and permeability of the system. Changes to the dissolved CO_2, porosity and permeability are updated in TOUGH2 for the next time step through the driver. Since the coupling method is essentially identical to FLOTRAN, the driver program linking TRANS to FLO was used as a guide in creating the portion of the driver program coupling TRANS. Furthermore, since TRANS was previously linked to FLOW using a sequentially coupled approach, the internal functions within TRANS under the identical coupling method are preserved when coupled to TOUGH2. Therefore, no individual testing of the TRANS simulator was necessary. However, coupled effects and mass balancing errors using the new driver program must be tested in future development efforts.

6.5 FUNCTIONS

The driver program module performs several functions in the TR-T simulator (Figure 6-2). Its main function is to update coupled variables between TRANS and TOUGH2. Secondary functions are to assign array address pointers, initialize TRANS, update permeability and porosity, and control coupled output.

The first procedure of the driver program is initialization of the main work array. The

main work array stores several individual arrays and provides computational workspace used in the TRANS simulator. Patterned after FLOTRAN, address pointers are created to define the location of each individual array. Once the main work array is created and the addresses are assigned the driver program initializes TRANS. The initialization process mimics that in FLOTRAN.

Once TRANS initialization and addressing is complete, the driver program releases control back to TOUGH2 to complete its initialization procedure. TOUGH2 then performs its initialization procedure using updated aqueous CO_2 concentration from TRANS. This ensures that at the beginning of the simulation there is an equivalent concentration of dissolved CO_2 present in both simulators. The CO_2 equation of state is called to determine the density of pure water at the initial temperature and pressure conditions. A second call to the equation of state uses the density of pure water and dissolved mass fraction of CO_2 to calculate the initial density of the solution. Following the solution density calculation "switch zero" is called in the driver program's MASSTRANSFER subroutine. "Switch zero" converts the molal concentration of dissolved CO_2 in TRANS to mass fraction dissolved CO_2 in TOUGH2.

The final step of initialization is to activate a permeability modifier function in TOUGH2, a new feature in the latest TOUGH2 release. Preprocessing of the permeability array is required by the user. In the driver program the permeability modifier is initialized as unity, where permeability modifications are calculated in TRANS at each time step. The power law relationship between permeability and porosity, described earlier, is specified

in the TRANS input file.

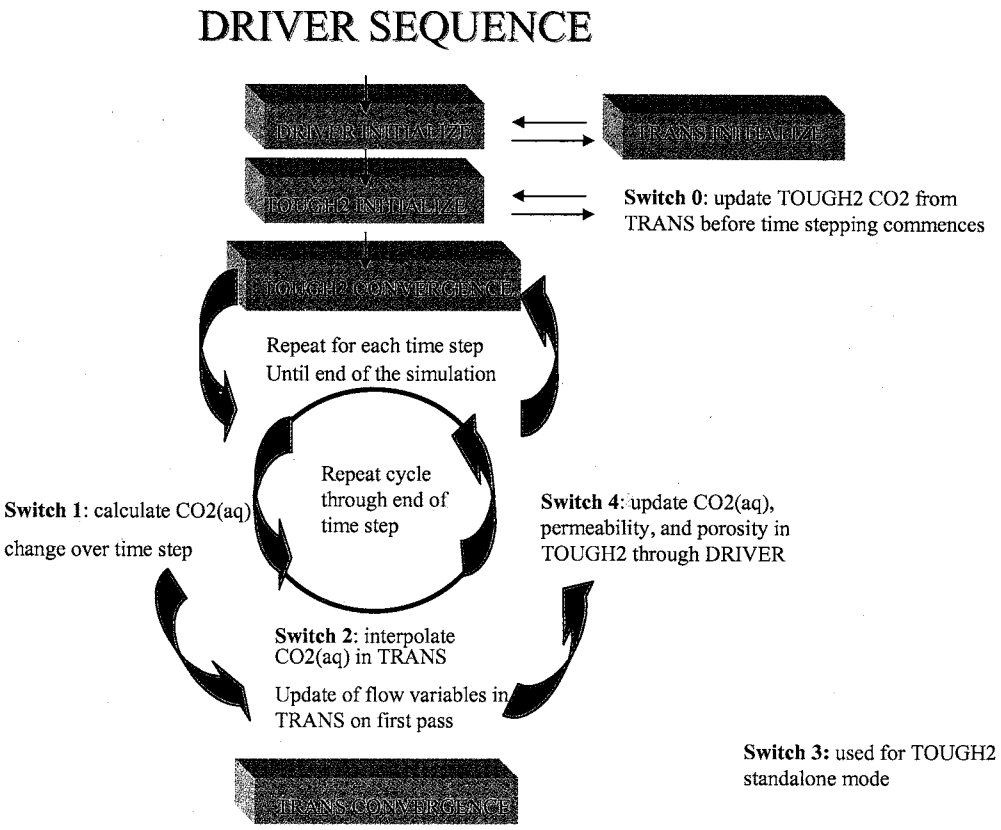

Figure 6-2: Sequence of events directed by driver program in the TR-T reactive transport model. The driver program initializes trans and allocates array space for TOUGH2. Once the TRANS initialization is complete, control is handed to TOUGH2 for the initialization step. After all initialization is complete, TOUGH2 runs to convergence of one time step. Coupled variables are updated in the driver program and TRANS repeats the time step completed by TOUGH2. CO2(aq) is controlled through the switch functions (outlined below). Once TRANS completes the time step, the resulting changes to the permeability and porosity are updated in TOUGH2 through driver. Control is then handed back to TOUGH2 where the process continues until the end of the simulation.

After the initialization procedure, the driver program calls TOUGH2 at the beginning of each new time step. At the convergence of each TOUGH2 time step coupled flow variables are updated in TRANS through the driver program and execution control is passed to TRANS to simulate the chemical reactions. "Switch 1" in the driver program's MASSTRANSFER subroutine is called to calculate the change in aqueous CO_2 during

the previous TOUGH time step increment due to CO_2 injection and any phase partitioning of CO_2 between the supercritical and aqueous phases (Figure 6-2). The driver program's subroutine RUN_TRANS is patterned after the TRANS driver program in FLOTRAN and is called to operate TRANS in a sequentially coupled mode. During each TRANS time step in the RUN_TRANS subroutine, "switch 2" of the MASSTRANSFER subroutine is called to interpolate the fraction of change in aqueous CO_2 over the larger TOUGH2 time step (Figure 6-2). TRANS internally interpolates the remaining coupled variables. Once TRANS advances to the current TOUGH2 time, control is released to the driver, where "switch 4" of the MASSTRANSFER subroutine is called and the final aqueous CO_2 concentration in TRANS is updated in TOUGH2 (Figure 6-2). The driver program then updates porosity and permeability in TOUGH2 through the driver program's subroutine PERM_MOD. TRANS calculates permeability changes based on porosity changes of the geologic media caused by the chemical reactions with brine fluid. Following the initialization procedure the driver program begins the time stepping process, updating coupled variables at each time step in the simulation. Control is then delegated to TOUGH2 where a new time step begins and the process repeats anew until the completion of the simulation.

6.6 ERROR TESTING

Sequentially coupling TRANS and TOUGH2 does not require direct modification of either code. The internal functions in TRANS have been previously programmed (Lichtner, 2000) and operate as intended in coupled mode. Minor additions were made to the TOUGH2 simulator, but none of these adaptations affect the internal functioning of

TOUGH2, inasmuch as they consist solely of calls to driver program subroutines or calculations used only by the driver. Since each simulator individually operates as intended in the standalone mode, error analyses were restricted to functions common in the coupled model. Therefore global chemical mass balancing and advective transport of aqueous CO_2, common to both simulators, are considered in this error analysis.

In light of the importance of appropriate mass balances, an automated global mass balance output is automatically created for each simulation. A sample mass balance analysis is provided below to illustrate that global mass is conserved in the example, However, balancing errors will likely be specific to each simulation. In addition, local mass balances in each code may occur. However, it is not within the scope of this project to code local mass balance functions in each simulator directly, which is required in order to calculate local mass balance calculations in the coupled TR-T model. Local mass balance calculations of each individual simulator have been set aside for a future project. For this first version of the TR-T model, a global mass balance test is assumed sufficient to demonstrate proper accounting and transfer of the system mass.

Also, a test simulation of the advective transport of CO_2 is provided below to demonstrate that the transport of CO_2 is simulated as intended in the TR-T model. Since each simulator evaluates transport of dissolved CO_2, it is important that both models be consistent with each other throughout the simulation. To eliminate the need to account for minor disparities in transport between the two simulators, TRANS was arbitrarily assigned to control dissolved CO_2 transport. Potential sources of error are addressed

below.

6.6.1 MASS BALANCE ANALYSES

A suite of test simulations was performed to demonstrate the maintenance of global mass balance for all chemical species. The purpose of this section is to show that mass is conserved in all species and to highlight where extra precaution should be taken to minimize error. The tests conducted in this analysis compare the resulting calculated total CO_2 to the intended total simulated CO_2 (i.e., the initial amount plus the amount injected into the model domain). Since the initial CO_2 is known, the total CO_2 at any time during the simulation can be calculated as the summation of the initial CO_2 and amount of CO_2 injected into the model domain from the beginning of the simulation.

As an aside, while the total CO_2 can be calculated, there is no available analytical solution to calculate the distribution of CO_2 within the model domain. An analysis using simulated boundary cell fluid fluxes and concentrations could be used to calculate the expected inner cell CO_2 mass balance. However, using these simulated fluxes is merely an analysis of whether each simulator is transporting CO_2 correctly through its domain. These simulated CO_2 fluxes have little applicability in determining whether global CO_2 is correct. Further, it is assumed that both TRANS and TOUGH2 have been fully tested and correctly simulate transport (Pruess, 1999; Lichtner, 2000). Assuming each individual simulator models transport accurately, a strong agreement between TR-T and TOUGH2 transport in addition to acceptable global CO_2 mass balancing would support that the TR-T simulator is functioning as intended.

In the TR-T model, the responsibility to account for chemical species is divided between TRANS and TOUGH2. Non-CO_2 chemical species are exclusively simulated in TRANS, while accounting responsibility for CO_2 is shared with TOUGH2. Therefore, a mass balance of non-CO_2 species is internal to TRANS, but calculating global mass balance of CO_2 requires adding the appropriate CO_2 components from each. To test for global mass balance, we employed a 50 x 50 x 1, two-dimensional vertical cross-section model (Figure 6-3), to mimic deep basin conditions. Cole (1999) also used a similar model, so another purpose of this particular model was to serve as a basis for comparison with Cole's (1999) earlier work.

We assigned the following initial and boundary conditions for the test analysis. Upper (near surface) and lower (greatest depth) vertical cells in the two-dimensional model were prescribed as Dirichlet and thus parameters were held constant in these cells throughout the simulation (Figure 6-3). We employed the large volume boundary cell approach in TOUGH2 (Pruess, 1999), and all Dirichlet boundary cells for the TR-T model were assigned a volume of 1.0×10^{20} m^3. The inner non-boundary cells were assigned a volume of 1.0×10^{6} m^3. The upper prescribed boundary was set to atmospheric pressure and a surface temperature of 15°C. Initial temperature was increased at a constant gradient of 25°C km^{-1} from the surface, while initial pressure was hydrostatically increased with depth. The boundary cells maintained the overall temperature and pressure gradients during the simulation. The reservoir-scale cross-section model was initially saturated with an aqueous brine solution within the pore space. The aqueous

concentration of the brine is outlined in (Table 6-1).

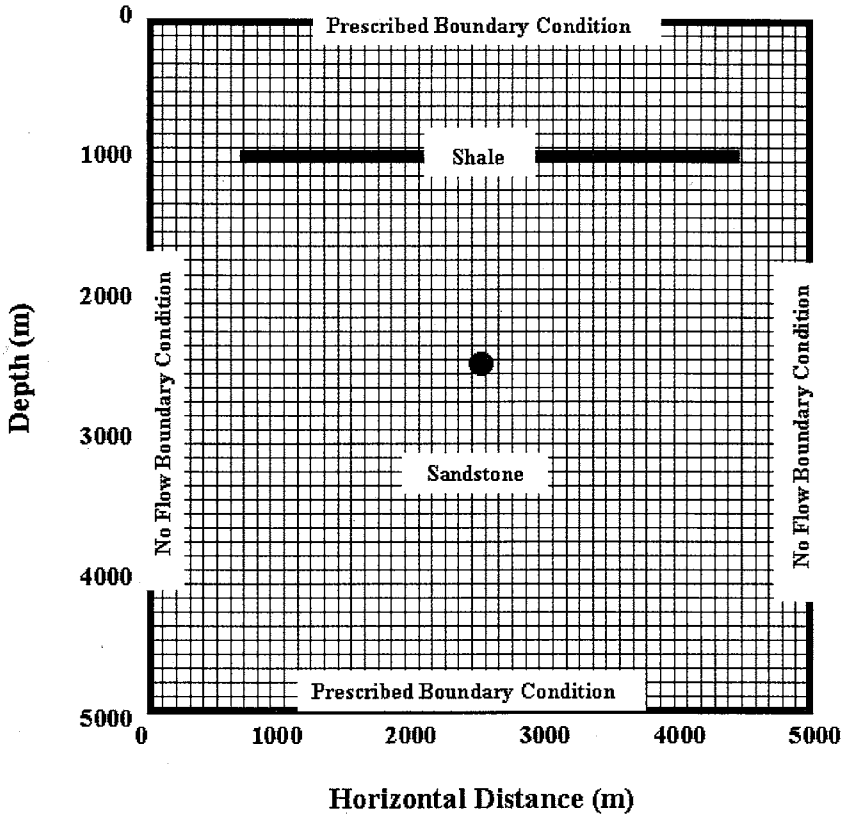

Figure 6-3: 50 x 50 x 1, 2500 cell, two-dimensional reservoir to basin-scale cross-section model. The media consists predominantly of sandstone with a chemically nonreactive capping layer at 1000m depth. Injection of CO_2 occurs in the center of the model (circle).

The initial aqueous CO_2 is minimal compared to the amount of CO_2 injected into the reservoir even under relatively minimal injection rates. At the beginning of the simulation

Species	Concentration (mol kg^{-1})
CO2(aq)	2.45E-25
Ca++	2.17E-03
Mg++	2.70E-03
Na+	0.4348
Cl-	0.4272
H+	3.16E-08
SiO2(aq)	1.00E-20

Table 6-1: Initial fluid concentration. The brine fluid composition was arbitrarily assigned and does not represent any particular formation brine. The negligible concentrations of CO2(aq) and SiO2(aq) were included in the brine so that the matrix could be pure quartz (SiO2(aq)) and that CO2(aq) could be accounted for as it was injected into the system.

approximately 2.5 x 10^{-1} kg of aqueous CO_2 was present in the cross-section. The pH of the brine solution was set to 7.5, a typical value in many brine fluids. The dissolved ions consisted mostly of sodium and chloride with moderate amounts of dissolved magnesium and calcite. The fluid concentration was initially homogeneous and saturated in all pore space of the geologic material, which was given an initial porosity of 15 percent. The vertical and horizontal intrinsic permeability was set to 1.0 x 10^{-17} m^2 and 1.0 x 10^{-15} m^2 respectively. The geologic material in the cross-section consisted of either pure quartz sandstone or a 99 percent by volume quartz sandstone with a 1 percent by volume calcite cementing mineral for all inner cells. The minor percentage of calcite was prescribed to incorporate the effect of a reacting matrix but low enough as to not overshadow the amount of CO_2 injected during the simulation, i.e., to minimize its effect on the mass balance of carbon. Likewise, large volume boundary cells were prescribed as pure quartz and therefore did not affect the CO_2 mass balance calculations. For each simulation, CO_2 was injected at a constant rate into the reservoir. Although these injection rates were constant, they were varied (7.0 x 10^{-1} kg-sec^{-1}, 7.0 x 10^{-2} kg-sec^{-1}, 7.0 x 10^{-3} kg-sec^{-1}) between simulations. The additional simulation with 1% calcite media was presented to incorporate the influences of a mineral phase containing CO_2. Based on these simulation results, some controls on mass balances were discussed to guide future simulations and reduce the potential for global mass balance errors.

In the CO_2 mass balance analyses, the simulated total CO_2 from all phases was compared to the calculated value determined from the injection rate and the initial conditions. Before the simulation began the initial chemical concentrations in all phases, with the

exception of gas phase CO_2, was calculated by TRANS. TOUGH2 was responsible for CO_2 in the gas phase. Therefore the total CO_2 in the aqueous, separate, and mineral phases was calculated by simple addition of the components of CO_2 in each simulator. The injection rate was constant, and the amount of CO_2 introduced into the system was calculated by the constant injection rate multiplied by the simulation time. Adding the initial CO_2 to the amount of CO_2 injected into the system yielded the total calculated CO_2.

Results from the mass balance test simulations show low mass balance errors for the test simulations. In the first pure quartz sandstone simulation, CO_2 was injected at a rate of 7.0×10^{-3} kg-sec^{-1}, which was increased an order of magnitude for the two subsequent simulations. Table 6-2, Table 6-3, and Table 6-4 show the results of each simulation in the order of increasing injection rate. Each chart reproduces the automated error balance output created in each TR-T simulation. From left to right within each table, simulation time in seconds was listed, followed by the CO_2 gas calculation from TOUGH2 and the CO_2 aqueous and mineral mass in TRANS. The total simulated CO_2 was calculated as the cumulative sum of the CO_2 in both TOUGH2 and TRANS. To the right is the calculated CO_2 and percent error between expected and simulated total CO_2 values. The last two columns display the time steps taken by TOUGH and TRANS during the simulation. TRANS generally took smaller time steps than TOUGH2. For example, in these simulations TRANS time steps out numbered TOUGH2 time steps by a factor of 25-100. A plot of the percent error of global CO_2 from each of the three simulations is shown in errors were low and decreased with time. Each of the simulations revealed a similar pattern of decreasing error with time as more CO_2 was introduced into the system. This

TIME (sec)	Gas (kg)	Aq. + Min. (kg)	Total Sim. (kg)	Total Calc. (kg)	Error %	TOUGH T.S.	TRANS T.S.
3.1540E+07	3.6126E+04	1.8395E+05	2.2008E+05	2.2075E+05	3.0432E-01	384	16
6.3070E+07	1.0938E+04	4.2916E+05	4.4009E+05	4.4150E+05	3.1922E-01	700	20
9.4610E+07	1.6374E+04	6.4562E+05	6.6199E+05	6.6226E+05	3.9515E-02	1017	25
1.2610E+08	5.3328E+04	8.2882E+05	8.8215E+05	8.8301E+05	9.7113E-02	1333	29
1.5770E+08	1.0936E+04	1.0918E+06	1.1028E+06	1.1038E+06	8.9747E-02	1649	33
1.8920E+08	1.6372E+04	1.3083E+06	1.3246E+06	1.3245E+06	9.7876E-03	1966	38
2.2080E+08	5.3328E+04	1.4913E+06	1.5446E+06	1.5453E+06	4.3801E-02	2282	42
2.5230E+08	1.0933E+04	1.7545E+06	1.7654E+06	1.7660E+06	3.2577E-02	2598	46
2.8380E+08	1.6371E+04	1.9709E+06	1.9873E+06	1.9868E+06	2.6055E-02	2915	51
3.1540E+08	5.3329E+04	2.1537E+06	2.2070E+06	2.2075E+06	2.2560E-02	3231	55
6.3070E+08	3.7561E+04	4.3785E+06	4.4160E+06	4.4150E+06	2.2145E-02	6387	87
9.4610E+08	3.0020E+05	6.3202E+06	6.6205E+06	6.6226E+06	3.1834E-02	9543	119
1.2610E+09	2.4860E+06	6.3419E+06	8.8279E+06	8.8301E+06	2.4528E-02	12698	151
1.5770E+09	4.6755E+06	6.3600E+06	1.1035E+07	1.1038E+07	1.9541E-02	15853	183
1.8920E+09	6.8665E+06	6.3764E+06	1.3243E+07	1.3245E+07	1.6219E-02	19008	215
2.2080E+09	9.0589E+06	6.3916E+06	1.5450E+07	1.5453E+07	1.3850E-02	22162	247
2.5230E+09	1.1252E+07	6.4057E+06	1.7658E+07	1.7660E+07	1.2078E-02	25317	279
2.8380E+09	1.3446E+07	6.4192E+06	1.9866E+07	1.9868E+07	1.0701E-02	28471	311
3.1500E+09	1.5615E+07	6.4342E+06	2.2049E+07	2.2050E+07	3.6952E-03	31589	343

Table 6-2: Mass balance results of CO_2 injected at rate of 7×10^{-3} kg-sec^{-1} in a quartz sandstone cross-section. Each component of CO_2 is added in the coupled model and compared to the calculated solution. The error percent is the relative error between the simulated and calculated values. Time steps taken in each simulator are at the far right.

TIME (sec)	Gas (kg)	Aq. + Min. (kg)	Total Sim. (kg)	Total Calc. (kg)	Error %	TOUGH T.S.	TRANS T.S.
3.1540E+07	3.6594E+05	1.8396E+06	2.2055E+06	2.2075E+06	9.1571E-02	384	16
6.3070E+07	1.2407E+05	4.2970E+06	4.4211E+06	4.4150E+06	1.3678E-01	700	20
9.4610E+07	3.3938E+05	6.3016E+06	6.6409E+06	6.6226E+06	2.7752E-01	1017	25
1.2610E+08	2.4388E+06	6.3616E+06	8.8004E+06	8.8301E+06	3.3609E-01	1333	29
1.5770E+08	4.6215E+06	6.4092E+06	1.1031E+07	1.1038E+07	6.1618E-02	1649	33
1.8920E+08	6.8191E+06	6.4167E+06	1.3236E+07	1.3245E+07	7.0263E-02	1966	38
2.2080E+08	9.0182E+06	6.4042E+06	1.5422E+07	1.5453E+07	1.9619E-01	2282	42
2.5230E+08	1.1213E+07	6.4406E+06	1.7653E+07	1.7660E+07	3.8568E-02	2598	46
2.8380E+08	1.3413E+07	6.4457E+06	1.9858E+07	1.9868E+07	4.6537E-02	2915	51
3.1540E+08	1.5612E+07	6.4328E+06	2.2045E+07	2.2075E+07	1.3617E-01	3231	55
6.3070E+08	3.6391E+07	7.7419E+06	4.4133E+07	4.4150E+07	3.9566E-02	6387	87
9.4610E+08	4.8662E+07	1.7547E+07	6.6209E+07	6.6226E+07	2.5606E-02	9543	119
1.2610E+09	7.0085E+07	1.8196E+07	8.8281E+07	8.8301E+07	2.2891E-02	12698	151
1.5770E+09	9.1333E+07	1.9023E+07	1.1036E+08	1.1038E+08	1.7924E-02	15853	183
1.8920E+09	1.1220E+08	2.0236E+07	1.3243E+08	1.3245E+08	1.4340E-02	19008	215
2.2080E+09	1.3159E+08	2.2920E+07	1.5451E+08	1.5453E+08	1.0623E-02	22162	247
2.5230E+09	1.4702E+08	2.9547E+07	1.7657E+08	1.7660E+08	1.7748E-02	25320	283
2.8380E+09	1.6481E+08	3.3824E+07	1.9864E+08	1.9868E+08	1.9704E-02	28474	315
3.1500E+09	1.8434E+08	3.6130E+07	2.2047E+08	2.2050E+08	1.2949E-02	31592	347

Table 6-3: Mass balance results of CO_2 injected at rate of 7×10^{-2} kg-sec^{-1} in a quartz sandstone cross-section. Each component of CO_2 is added in the coupled model and compared to the calculated solution. The error percent is the relative error between the simulated and calculated values. Time steps taken in each simulator are at the far right.

was due to the increase in total CO_2 relative to the solver convergence tolerances (Figure 6-4). The results indicated that total CO_2 increased with time and mass balance

TIME (sec)	Gas (kg)	Aq. + Min. (kg)	Total Sim. (kg)	Total Calc. (kg)	Error %	TOUGH T.S.	TRANS T.S.
3.1540E+07	3.6126E+04	1.8395E+05	2.2008E+05	2.2075E+05	3.0432E-01	384	16
6.3070E+07	1.0938E+04	4.2916E+05	4.4009E+05	4.4150E+05	3.1922E-01	700	20
9.4610E+07	1.6374E+04	6.4562E+05	6.6199E+05	6.6226E+05	3.9515E-02	1017	25
1.2610E+08	5.3328E+04	8.2882E+05	8.8215E+05	8.8301E+05	9.7113E-02	1333	29
1.5770E+08	1.0936E+04	1.0918E+06	1.1028E+06	1.1038E+06	8.9747E-02	1649	33
1.8920E+08	1.6372E+04	1.3083E+06	1.3246E+06	1.3245E+06	9.7876E-03	1966	38
2.2080E+08	5.3328E+04	1.4913E+06	1.5446E+06	1.5453E+06	4.3801E-02	2282	42
2.5230E+08	1.0933E+04	1.7545E+06	1.7654E+06	1.7660E+06	3.2577E-02	2598	46
2.8380E+08	1.6371E+04	1.9709E+06	1.9873E+06	1.9868E+06	2.6055E-02	2915	51
3.1540E+08	5.3329E+04	2.1537E+06	2.2070E+06	2.2075E+06	2.2560E-02	3231	55
6.3070E+08	3.7561E+04	4.3785E+06	4.4160E+06	4.4150E+06	2.2145E-02	6387	87
9.4610E+08	3.0020E+05	6.3202E+06	6.6205E+06	6.6226E+06	3.1834E-02	9543	119
1.2610E+09	2.4860E+06	6.3419E+06	8.8279E+06	8.8301E+06	2.4528E-02	12698	151
1.5770E+09	4.6755E+06	6.3600E+06	1.1035E+07	1.1038E+07	1.9541E-02	15853	183
1.8920E+09	6.8665E+06	6.3764E+06	1.3243E+07	1.3245E+07	1.6219E-02	19008	215
2.2080E+09	9.0589E+06	6.3916E+06	1.5450E+07	1.5453E+07	1.3850E-02	22162	247
2.5230E+09	1.1252E+07	6.4057E+06	1.7658E+07	1.7660E+07	1.2078E-02	25317	279
2.8380E+09	1.3446E+07	6.4192E+06	1.9866E+07	1.9868E+07	1.0701E-02	28471	311
3.1500E+09	1.5615E+07	6.4342E+06	2.2049E+07	2.2050E+07	3.6952E-03	31589	343

Table 6-4: Mass balance results of CO_2 injected at rate of 7×10^{-1} kg-sec^{-1} in a quartz sandstone cross-section. Each component of CO_2 is added in the coupled model and compared to the calculated solution. The error percent is the relative error between the simulated and calculated values. Time steps taken in each simulator are at the far right.

time steps chosen for the test simulations. There was also an oscillatory effect superimposed over this general trend as the error approached zero. The controls of this oscillatory pattern will not be explored further, but could be a product of the sequential coupling, time stepping, or solver convergence tolerances. Despite the oscillatory patterns, the error decreased with time and was well within acceptable limits.

The mass balance results for the non-CO_2 species controlled by the TRANS simulator reveal mass balance errors far below that of CO_2 species. Non-CO_2 species are solely controlled by TRANS and therefore do not undergo any mass exchange through driver, providing less opportunity for error. Also a likely reason for the small error was no imposed source or sink of non-CO_2 species, which would have altered concentrations during the simulation. In each simulation tested, non-CO_2 species exhibited identical results relative to the degree of numerical precision in the TRANS output file. Although

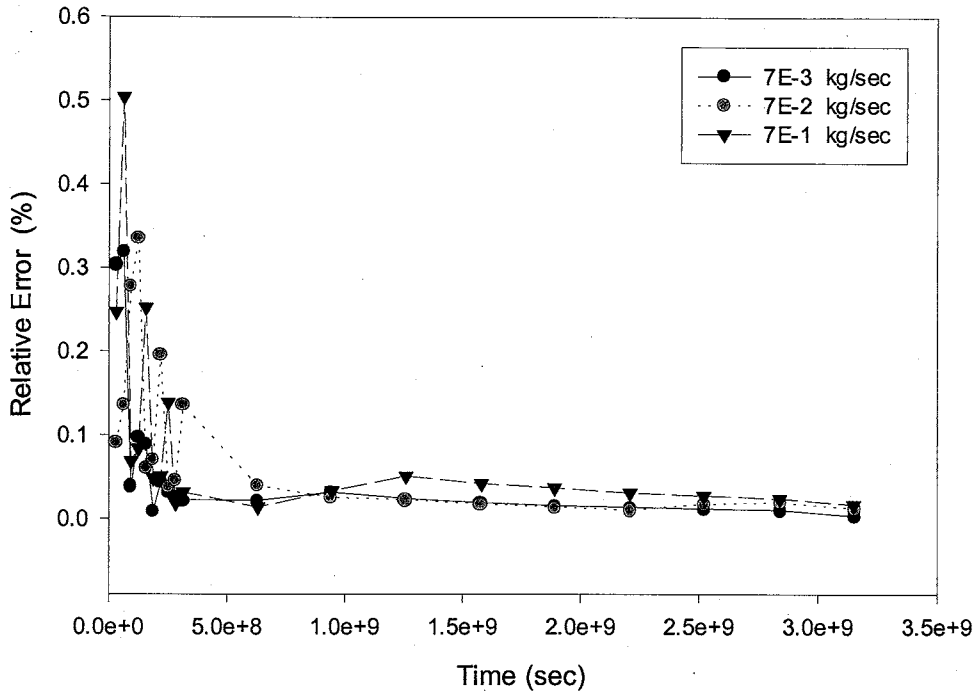

Figure 6-4: Error percent (calculated: simulated) from CO_2 injection, at 3 different rates. The error percent declines with time as CO_2 mass is increased within the system. Note that the maximum error is below 1percent. The sign of the error denotes whether error is greater or less than the calculated values.

the results were nearly identical for each simulation, Figure 6-5 shows the non-CO_2 species error under the highest CO_2 injection rate. The remaining species error increased throughout the simulation, but the magnitude of the error even after 30,000 time steps (100 years) was below 1.0×10^{-7} percent mass balance error. In all test simulations performed in the development of TR-T model, non-CO_2 species error in TRANS was always extremely low.

The highest injection rate simulation was repeated for sandstone comprised of 1 percent calcite and 99 percent quartz by volume. Calcite was added to the quartz matrix to include the potential error caused by incorporating a solid form of CO_2 within the model.

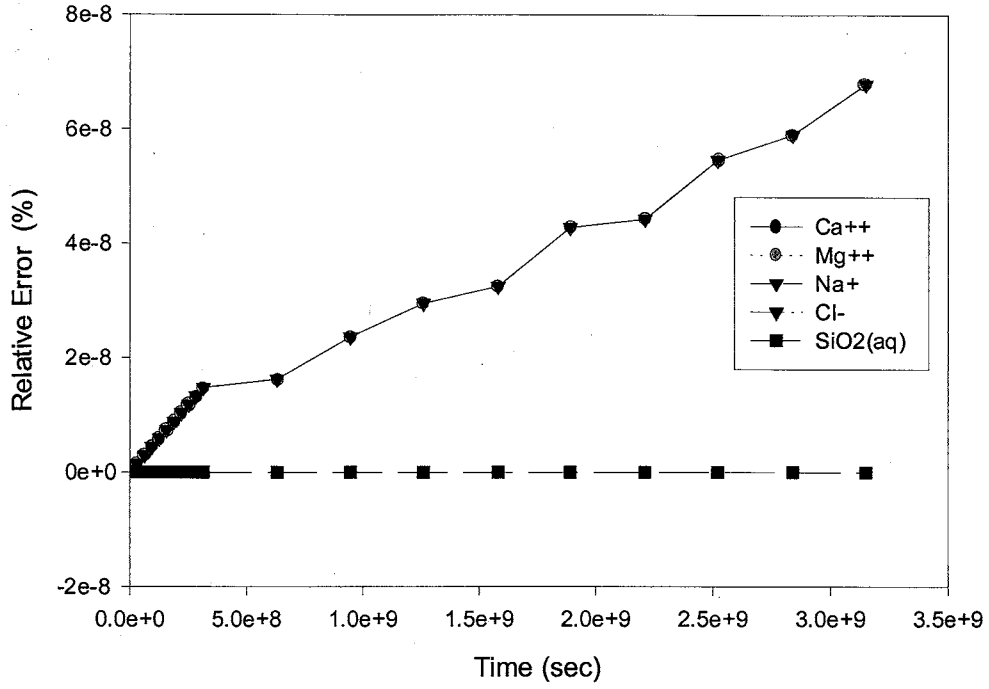

Figure 6-5: TRANS relative error percent through time for all non-CO_2 species for all injection rates. Note that while error increases steadily throughout the simulation, the magnitude of error is low, typical in TRANS simulations. SiO_2 error is lowest, with all other species grouped closely in the higher error line. The sign of the error denotes whether the error is greater or less than the expected values

A one percent by volume proportion of calcite was chosen to limit the effect of the matrix in relation to the mass of CO_2 injected during the simulation. The volume of calcite was minor in relation to the quartz matrix, but even a 1 percent by volume proportion of calcite was two orders of magnitude greater than the amount of CO_2 injected. The results shown in Figure 6-6 were as expected. When calcite was included in the matrix the overall global relative error diminishes because the proportion of CO_2 injected into the system is smaller.

The mass balance analysis demonstrated the potential mass balance errors that may arise

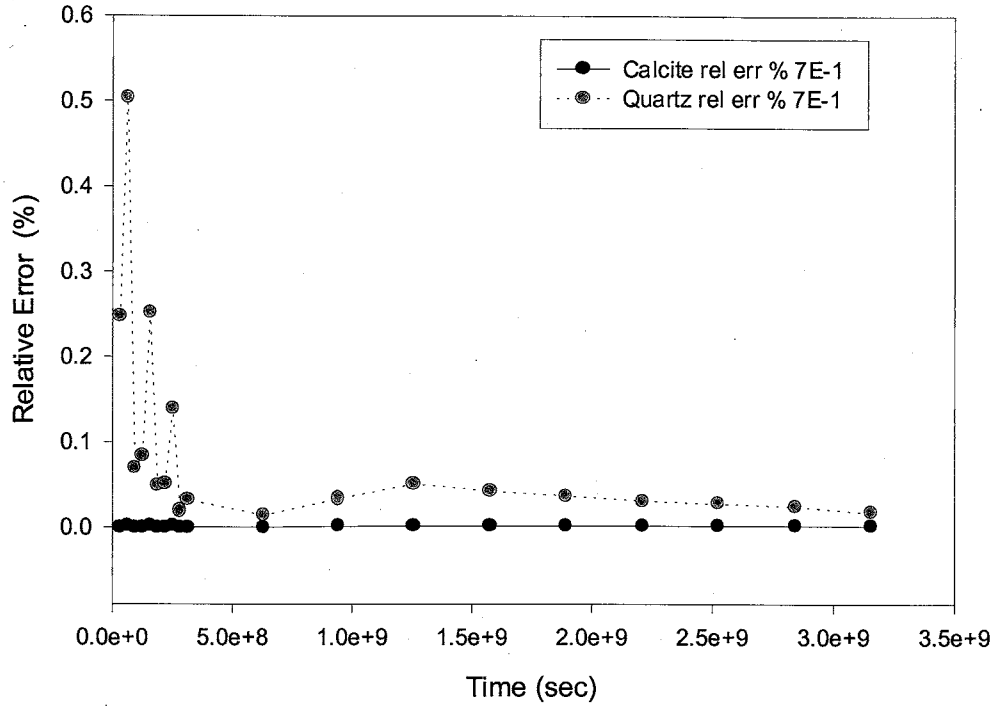

Figure 6-6: Relative error (percent) of CO_2 injected in a pure quartz sandstone media compared to a quartz sandstone consisting of 1 percent calcite cement by volume. The results show that error decreases with increasing calcite (solid form CO_2 species).

during a simulation as function of time step size. As a simple comparison, the maximum time step size was increased one order of magnitude for each simulator in the highest injection pure quartz simulation, shown in (Figure 6-7). In the TR-T model, time stepping is internally controlled in each simulator where a minimum and maximum time step are prescribed in each input file. The TRANS time steps are essentially identical between simulations. This suggested that TRANS was at its optimal time step size and is operating to its full efficiency at the tolerance level prescribed in the TRANS input file. The TOUGH2 time step size increase demonstrated that the TOUGH2 simulator time steps are not optimized. However, the increased time step size in TOUGH2 increased the global mass balance error in the TR-T simulator. Further increases in the time steps

would likely lead to lower resolution and increased mass balance errors. In addition to time stepping issues, solver type and tolerances, grid spacing and geometry, CO_2 injection rates and perhaps the grid size may have contributed to mass balance errors. In light of the numerous contributions to global mass balance error, the automated CO_2 balance output has been created to help the user constrain global balance errors within acceptable limits for specific simulations.

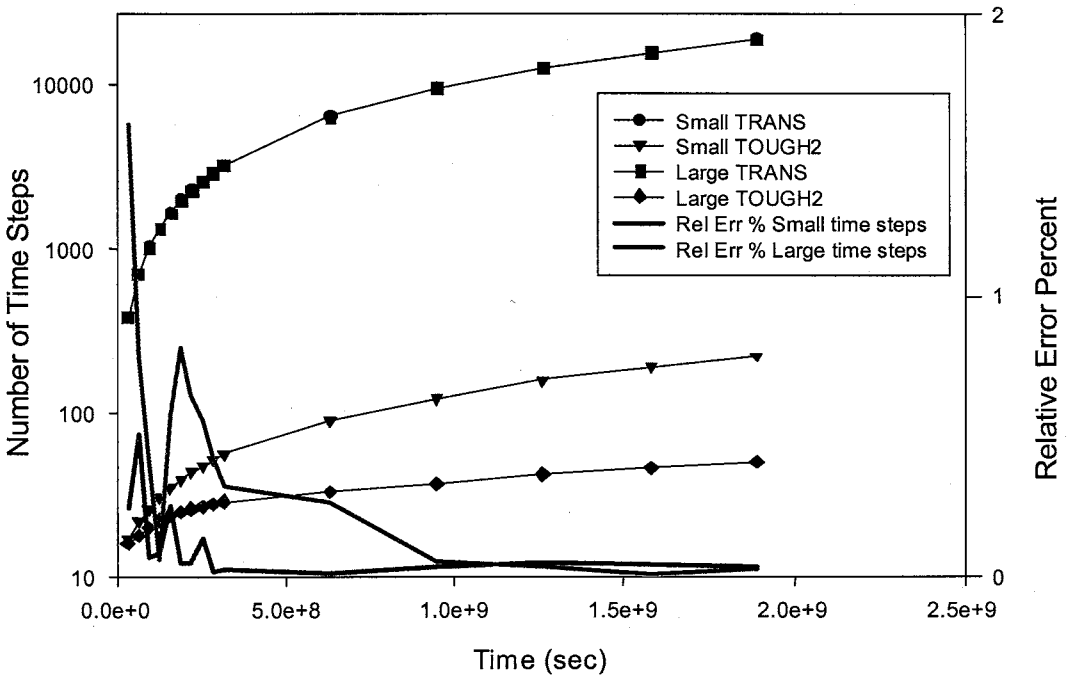

Figure 6-7: Comparison of the global CO_2 mass balance error in relation to number of time steps. "Large" represents large time steps. "Small" represents small time steps. The solid lines (black and green) represent the mass balance error shown on the right vertical axis. The left vertical axis shows the range of time steps taken during the simulation (plot lines shown in red). Note that for both simulations, although each simulator was allowed to take larger time steps, only TOUGH2 increased the time step size. The larger TOUGH2 time step size reduced resolution and therefore increased the CO_2 mass balance error.

6.6.2 ADVECTIVE TRANSPORT

In the TR-T coupled model, both TRANS and TOUGH2 simulate the transport of CO_2 in

the dissolved phase. It is necessary to evaluate whether advection of dissolved CO_2 is comparably modeled in each numerical simulator. Dispersion is not modeled in TOUGH-EOSCO2 and therefore TRANS controls dispersive fluxes in the TR-T simulator. As stated above, TRANS controls the dissolved phase CO_2, updating TOUGH2 between each of its time steps. Once TOUGH2 converges at a particular time step, coupled flow variables are updated in TRANS. TRANS simulates the chemical reactions that occurred during the TOUGH2 time step, and updates the dissolved phase CO_2 before releasing control back to TOUGH2. In this manner synchronization of dissolved CO_2 in TR-T is maintained.

We evaluated whether advection is simulated correctly by comparing dissolved CO_2 profiles in TOUGH2 with those in TR-T using identical 1-D piston flow models. Dirichlet boundary conditions were prescribed in each boundary cell to maintain a pressure gradient through the horizontal column, providing a constant flow velocity. Throughout the simulation, fluid moved from the first boundary cell through the column and into the terminal boundary cell. Temperature was held constant at 25°C. The simulated media consisted of pure quartz sandstone with a porosity of 15% and a permeability of 1×10^{-14} m^2. The initial concentration of dissolved CO_2 throughout the column and terminal boundary cell was prescribed as $\sim 10^{-75}$ M, essentially zero with respect to the solver. A small number was employed because TRANS primary variable concentrations must be assigned a non-zero value. We initialized the influent boundary cell with an aqueous CO_2 concentration of 2.45×10^{-4} M. From the beginning of the simulation, the higher concentration fluid in the first boundary cell flowed through the

column towards the terminal boundary cell. Since the pressure gradient is maintained constant, the resulting fluid velocity was constant. Therefore, the position of the CO_2 profile may be calculated through time.

The expected position of the CO_2 slug was calculated by multiplying the fluid velocity by the current time. The expected position was compared to the simulated position of TOUGH2 in the standalone mode and the TR-T coupled model. The maximum time step size was varied 3 orders of magnitude to create varying profiles of dissolved CO_2. For each of the 3 simulations of varying time step size, the simulated and calculated profiles are compared at 4 points in time along the column. The first simulation was assigned a maximum time step size of 1 x 10^5 seconds (Figure 6-8). The four print times

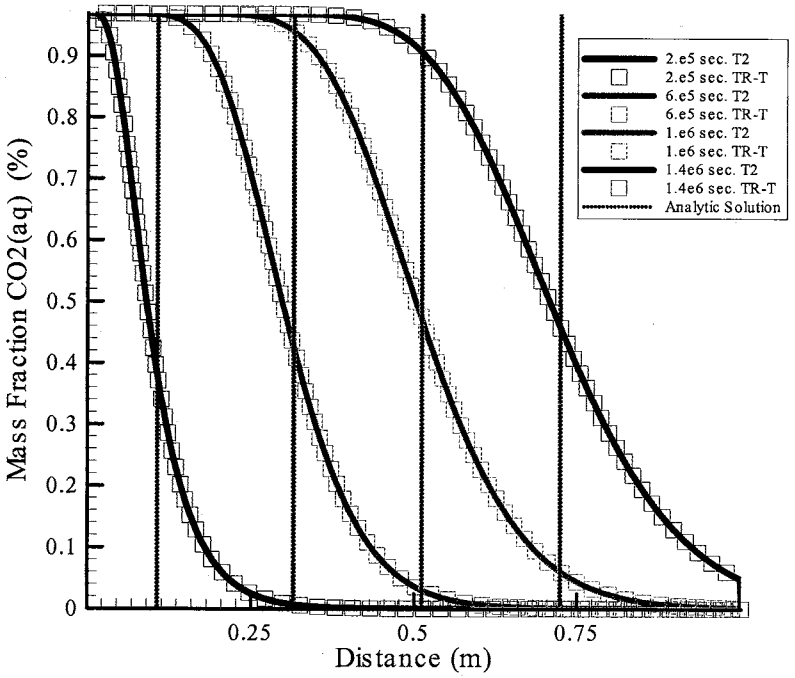

Figure 6-8: Maximum time steps are 1.0 x 10^5 seconds. The TR-T coupled model results (symbols) are compared to TOUGH2 (solid lines). The dotted black line is the calculated expected position of each profile.

incrementally increase along the column from left to right. The TOUGH2 standalone mode results are in solid colored lines and the TR-T coupled results are represented as symbols of the corresponding line color. The calculated expected position is shown as a dotted black line. There is excellent agreement between TOUGH2 and the TR-T coupled model, showing no appreciable difference in values. However there is moderate numerical dispersion at each print time. In absence of diffusion or mechanical dispersion, as is the case here, the expected solution would be a vertical profile. In viewing each solution it becomes clear that the model underpredicts the concentration of CO_2 in the upflow direction and over predicts CO_2 in the down stream direction, with error increasing in time and/or distance traveled along the column, i.e., it is not a vertical front. This may be referred to as "numerical dispersion" or low resolution which may be attributed to a number of factors such as large time-step size, coarse grid size, upstream weighting, etc. Also note the overall uniformity in the deviations from the analytical solution at each time shown and the slight shifting of the concentration profiles in the upstream direction (intersection of expected line and CO_2 profile at mass fraction = .5). In general the bulk of the displacement is modeled correctly. Figure 6-9 shows the results of decreasing the maximum time step to 1×10^4 seconds. Overall, the same observations are noted when using an order of magnitude smaller time step. However, the apparent numerical dispersion is significantly decreased, i.e., the profiles are more vertical. Also the shifting of the CO_2 profiles decreased using a smaller time step, and revealed less shifting as a function of distance from the injection wells. As in the previous simulation, the TR-T transport is in excellent agreement with TOUGH2 in the standalone mode. When the maximum allowable time step is reduced to 1×10^3 seconds, nearly all of the

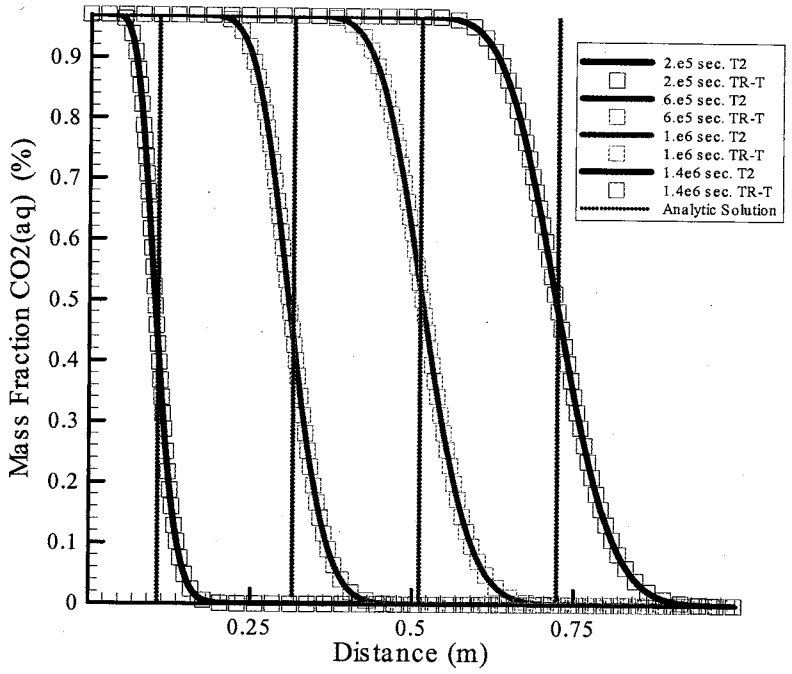

Figure 6-9: Maximum time steps are 1.0 x 10^4 seconds. The TR-T coupled model results (symbols) are compared to TOUGH2 (solid lines). The dotted black line is the calculated expected solution of each profile.

numerical dispersion is removed (Figure 6-10). Once again the TR-T coupled model transport is in excellent agreement with TOUGH2 in the standalone mode. In addition, the shifting of the CO_2 profile has been nearly eliminated. In summation, for the 1000 cell 1-D model, the transport of dissolved phase CO_2 is simulated as intended in the TR-T coupled model, matching the transport calculated by TOUGH2 in the standalone mode.

The former suite of test simulations was presented to demonstrate that the dissolved CO_2 transport of the TR-T model is functioning as intended. There may be cases where such close agreement in simulating CO_2 transport is not achieved. Potential factors such as

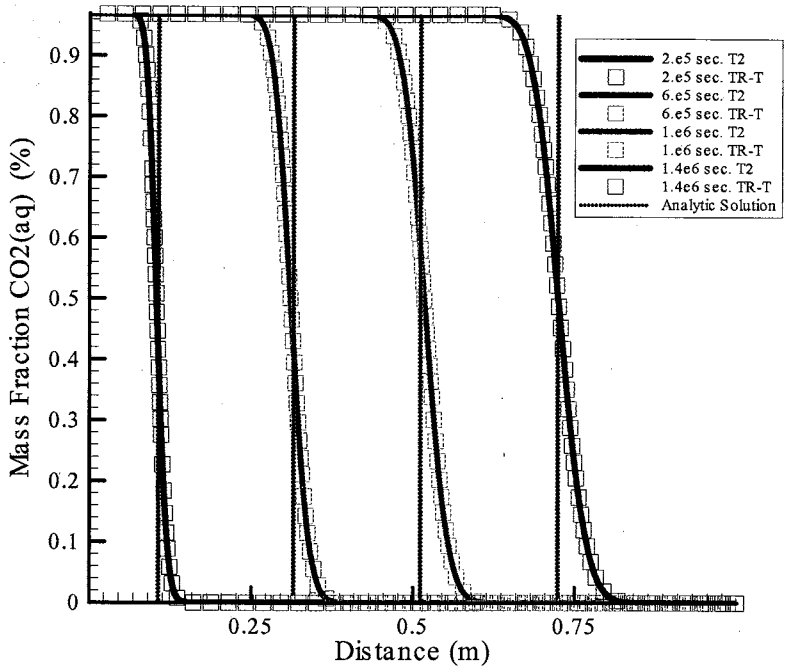

Figure 6-10: Maximum time steps are 1.0 x 10^3 seconds. The TR-T coupled model results (symbols) are compared to TOUGH2 in standalone mode (solid lines). The dotted black line is the calculated expected solution of each profile.

time step size, fluid reactions with the matrix, upstream weighting, model dimensions, or number of cells may reduce the agreement in modeling dissolved CO_2 transport. Also, it is evident that by simply decreasing the time step size the apparent numerical dispersion in TOUGH2 was significantly reduced. In short, the accuracy of the TR-T model may differ using different model domains, grid resolution, and time step size. Care should be taken to ensure that errors are minimized.

6.7 DRIVER SUMMARY

The TR-T model incorporates the driver program to link TOUGH2-EOSCO2 to TRANS in a sequentially coupled scheme. Sequential coupling preserves the original functioning of each simulator, but also generates some operational errors due to coupled mass

imbalances and dissolved CO_2 transport. Test results of the 2500 cell 2-dimensional cross-section model showed TR-T mass imbalances were small. Global mass balance errors of both CO_2 and non-CO_2 species are usually much less than 1 percent, when time steps and convergence criteria are appropriately prescribed. Dissolved CO_2 profiles are nearly identical at each CO_2 injection rate in the 1000 cell 1-D horizontal column simulations, suggesting that transport is also simulated properly in the coupled model. Tests simulations demonstrate proper model performance, but it is important to consider potential errors specific to each simulation.

CHAPTER 7: RESULTS

7.1 INTRODUCTION

CO_2 sequestration is receiving significant scientific attention as a means of reducing carbon fluxes into the atmosphere. Of the various proposed strategies, sequestering CO_2 into deep geologic basins may provide safe and reliable storage of anthropogenic CO_2, thereby reducing greenhouse gas emissions entering the atmosphere (Wawersik et al., 2000). Evaluating geologic reservoirs as CO_2 repositories requires accurate characterization of CO_2 mobility and chemical reactivity. Research has shown that CO_2 mobility may vary significantly, mainly dependent on CO_2 injection rate and depth, and absolute permeability (Cole, 1999, Weir, 1995, Law and Bachu 1996 and others). However, these modeling studies neglected chemical reactions among the CO_2, brine, and geologic media that may induce significant changes in intrinsic permeability, porosity, and most importantly to the mobility of CO_2. In light of this limitation, we have created the TR-T reactive transport simulator of CO_2 injection in geologic media. The TR-T simulator is a tool to characterize both the physical and chemical influences affecting CO_2 storage potential in deep basin reservoirs.

Our current project compares TR-T model predictions with results of CO_2 and brine injection experiments performed at the Petroleum Resource and Recovery Center, New

Mexico Tech. Our main goals are to evaluate the accuracy of the TR-T simulator and to quantify permeability and porosity changes caused by chemical or mechanical processes associated with CO_2 injection in representative basin environments. We compared TR-T model predictions with the first completed laboratory experiment, but additional experimental results are not yet available.

We performed a sensitivity analysis to characterize chemical processes in various geologic media. We simulated CO_2 and brine injection through four rock types. We chose a pure quartz sandstone (slow reaction rate) and pure calcite media (high reaction rate) to represent end member cases of matrix reactivity among reservoir injection candidates. In addition to monolithic media, we chose quartz-evaporite and quartz-carbonate rock assemblages to evaluate the matrix response of lithologically heterogeneous media. For each media, we varied brine alkalinity and pH using published values for siliclastic and carbonate aquifers (Langmuir, 1997). These bench scale simulations were analyzed to compare parameter importance and their degree of sensitivity under varying reservoir conditions. Finally, we examined a larger scale system by transforming the calcite bench scale simulation into a reservoir scale 2-D model. From the available laboratory results and model simulations, we make inferences about the effects of CO_2 sequestration on varying geological systems at the bench and reservoir scales.

7.2 BENCH SCALE EXPERIMENTS AND MODEL SIMULATIONS

The major goal of the laboratory experiments is to characterize permeability and porosity changes in geologic media caused by CO_2 injection and associated chemical processes.

Our hypothesis is that CO_2 injection into the subsurface may cause significant physical changes to the matrix for many rock types. We compared results from the first completed experiment to TR-T model predictions. In addition, we performed a sensitivity analysis to determine which chemical or mineralogical properties are most important when evaluating a basin as a CO_2 repository. Below is a detailed description of the laboratory experiments and corresponding model representation, followed by the results of our analysis and a discussion of their significance.

7.2.1 EXPERIMENTAL EQUIPMENT

All CO_2-brine injection experiments involve the same basic mechanical configuration. A schematic of the system is shown in Figure 7-1. Supercritical CO_2 and brine, injected by separate syringe pumps, are flushed through a cylindrical rock sample contained within a core holder assembly. Confining pressure is applied to the outer surface of the sample to eliminate fluid flow along the sample edges. Figure 7-2 is a photograph of the core holder assembly. Pressure transducers and differentials are used to measure the pressure difference across the sample at various times during the experiment. The fluid exit pressure is maintained by a back pressure regulator positioned at the down stream end of the core holder. Injection is halted periodically to measure the permeability and porosity of the sample. Once permeability and porosity are measured, the system is re-pressurized and the experiment continues until the next permeability-porosity measurement or experiment termination.

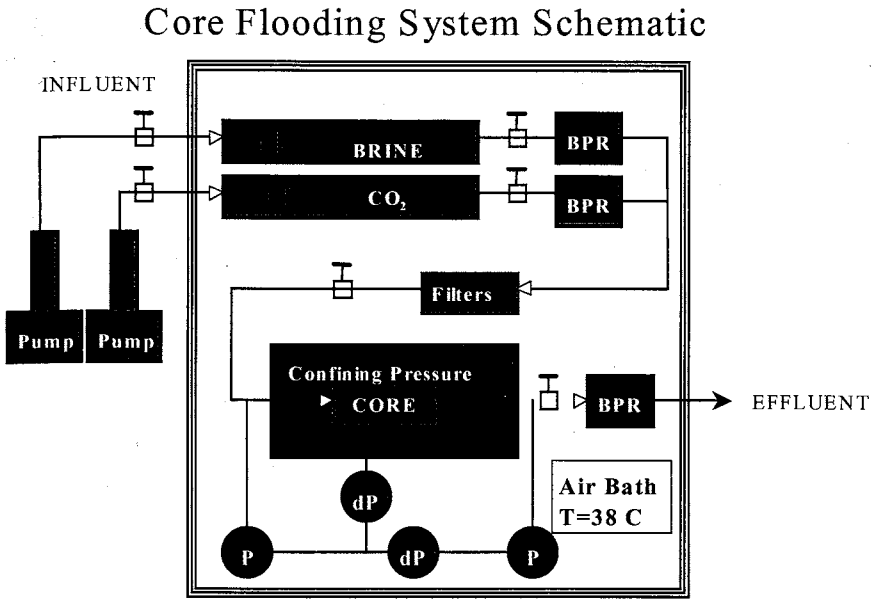

Figure 7-1: Schematic showing fluid injection experiments. CO_2 and brine are pumped from their respective syringe pumps through the rock core sample contained within the core holder assembly. Exiting fluid must pass through a BPR valve set at 13.79MPa back-pressure. System temperature was held at 38°C. "P" denotes the pressure at each point. The pressure differential is measured across each location labeled "dP".

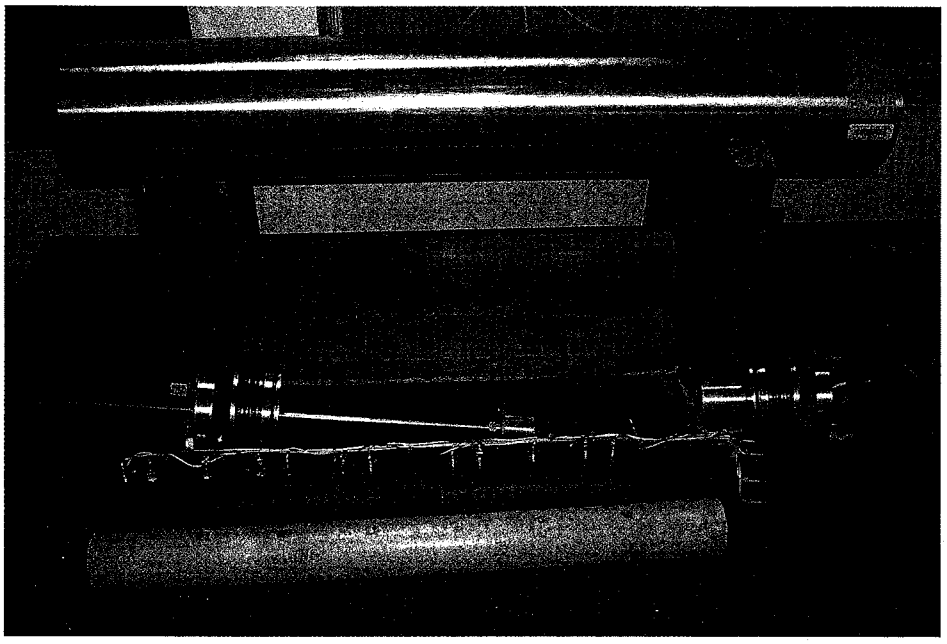

Figure 7-2: Photograph of Temco core holder assembly (top). The cylindrical core sample is displayed at the bottom of the photo, and measures 5 cm in diameter and .50m in length. The sealing sleeve adjacent to core the sample seals the core sample from the confining fluid in the core holder assembly

7.2.2 MODEL DOMAIN

We simulated the laboratory experiments using a 1-D 100 cell horizontal column with each cell measuring 4.5 x 10^{-2}cm x 4.5 x 10^{-2}cm x .5cm (Figure 7-3). Non-boundary cell volumes were preserved to match the experimental dimensions, but the Dirichlet effluent cell was assigned a larger volume of 1 x 10^{6} m^3 to maintain constant boundary conditions. For each simulation, we injected supercritical CO_2 and brine into the first 4 grid cells, inducing fluid flow from the injection area towards the effluent cell. We assigned the Dirichlet effluent cell a constant pressure of 13.79MPa to represent the back pressure regulator (BPR) in the core flooding system. Pressure in the remaining model cells was allowed to fluctuate. This model configuration was used to capture pressure changes resulting from the chemical processes affecting the permeability of the geologic media.

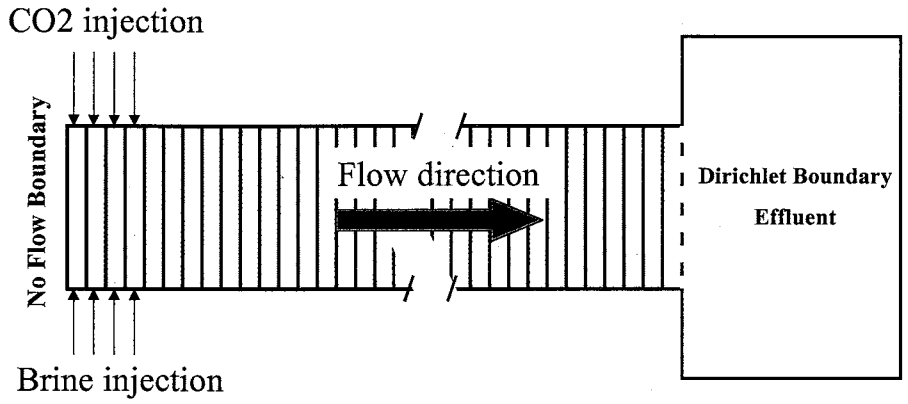

Figure 7-3: 1-D 100-cell model used to represent laboratory core experiments. CO_2 and brine solution were injected into the first 4 grid cells (left), which induced fluid flow from the injection point towards the effluent catchment cell (left to right), held at 13.79 MPa.

7.2.3 ROCK CHARACTERISTICS

One model was developed explicitly to simulate an actual dolomite-anhydrite core flow experiment, performed by staff at the Petroleum Recovery Research Center in 2002. We

also evaluated four rock types in a sensitivity analysis to complement the dolomite-anhydrite core flow experiment model. The mineralogical volumetric percentages for each media are presented below (Table 7-1). Quartz was chosen for its low reactivity with formation fluids. Calcite was chosen for high reactivity with formation fluids. Evaporite and carbonate mineral fractions within quartz sandstone were chosen to characterize chemical reactivity of lithologically heterogeneous media.

Pure Quartz	Pure Calcite	Quartz w/ Carbonates	Quartz w/ Evaporites	Dolomite w/ Anhydrite
Quartz 100 %	Calcite 100%	Quartz 40%	Quartz 45%	Dolomite 57%
--	--	Calcite 30%	Gypsum 20%	Anhydrite 20%
--	--	Magnesite 15%	Halite 20%	--

Table 7-1: Media variations used in the TR-T model simulations. Values are percent by total volume, where porosity is 15 % for all media, except measured dolomite-anhydrite core porosity equaled 13%.

The anhydrite mineral fraction in the experimental dolomite-anhydrite rock was estimated at 20 percent by visual inspection of several trimmings from the core stock. The resulting amount of dolomite was calculated as the residual fraction, accounting for the measured porosity. Originally, we planned on using a pure calcite media. However, due to mechanical difficulties the experiment was postponed and a previous dolomite-anhydrite experiment was substituted in its place. Future laboratory experiments using mixed media should include use of thin section point counts or some related analysis to determine mineral fractions.

7.2.4 MINERAL REACTION KINETICS

In order to determine the influences of varying lithology, fluid-mineral reaction rates

must be quantified for simulator input. Mineral kinetics in TRANS are calculated as a function of the prescribed kinetic rate and the degree to which the fluid is in equilibrium with the geologic media. As described earlier, the rate of reaction in TRANS decreases as the system approaches equilibrium and conversely increases as the system diverges from equilibrium.

We estimated the reaction kinetics for calcite in a chemically unsaturated solution using a relation from Sjoberg and Rickard (1984), given by

$$R = k[H]^{0.90} \text{ where } k = 0.198 - 444/T, \qquad \textbf{(Eq 7-2-1)}$$

where the hydrogen activity ([H]) and temperature (T), control the reaction rate (R). In this relation the kinetic term (k) is a function of temperature (T). The rate was determined as the product of the rate constant, and hydrogen activity. Based on a temperature of 38°C and a brine solution of pH 4.0, the calcite reaction rate was estimated as ~1.0×10^{-4} mol kg^{-1} sec^{-1}. However, to be compatible with the TRANS simulator the mineral reaction rate must be specified in terms of surface area rather than per unit mass.

We employed an idealized relation to estimate the surface area to volume ratio where

$$S = (6/D) * \lambda, \qquad \textbf{(Eq 7-2-2)}$$

which assumed that the effective surface area to volume ratio (S) could be approximated

by spherical grain particles of diameter (D), corrected for a roughness coefficient (λ). The roughness coefficient depends on the degree of weathering, physical mineral properties, and in some cases laboratory preparation (Lichtner et al., 1996). We assumed a roughness coefficient of 1. We estimated a mean grain size diameter of .1mm (Folk, 1962). Using a roughness coefficient of 1 and mean grain diameter of .1mm in the above relation (Eq 7-6-2), the surface area to volume ratio of the calcite media was estimated at 60,000 to 1. Applying our surface area to volume estimation and multiplying by mineral density (2650 kg m^3), the reaction rate of calcite was calculated to be $\sim 1 \times 10^{-5}$ mol $m^{-2} sec^{-1}$, within an order of magnitude of laboratory values measured at 25°C (Stumm, 1990). Since the solubility of calcite decreases as a function of temperature we expected a lower solubility.

In addition to calcite reaction rates, Stumm, (1990) measured reaction rates of dolomite and quartz. The dolomite reaction rate was measured to be roughly an order of magnitude slower than calcite. The quartz reaction rate was reported to be roughly 8 orders of magnitude slower than calcite. These relative mineral rate differences were used to estimate the reaction rates of dolomite and quartz, relative to the calculated kinetic reaction rate of calcite at 38°C. In addition, since the dolomite-anhydrite sample in the completed experiment exhibited porous cavities, the effective surface area of fluid-mineral contact decreased (Lichtner et al., 1996). To account for the decrease in effective surface area the dolomite reaction kinetics were decreased an order of magnitude. Therefore, model reaction rates for dolomite and quartz were calculated to be 1×10^{-7} mol cm^{-2} sec^{-1} and 1.0×10^{-13} mol cm^{-2} sec^{-1} respectively. However, due to the widely reported difficulties of precipitating dolomite under laboratory conditions (Arvidson et al.,

2000, Land, 1998), dolomite reaction kinetics were turned off in simulations without an initial dolomite mineral fraction. Dolomite precipitation requires microbial intervention (Lith et al., 2000). The TR-T simulator predicts dolomite precipitation in a microbe rich environment, and in laboratory environments (microbe poor environments) reaction kinetics must be manually turned off. We assumed reaction rates of magnesite and dolomite were equal. Initial evaporite reaction rates were estimated as an order of magnitude faster than calcite at 1×10^{-4} mol cm^{-2} sec^{-1}. As with dolomite (in the dolomite–anhydrite sample) the reaction rate of anhydrite was adjusted for preferential flow due to cavities present in the experiment sample. In addition the anhydrite was observed to be concentrated in nodules rather than being disperse through the sample. We decreased the reaction rate an additional order of magnitude to account for the lower effective reactive surface area of the nodules in relation to a disperse media. (Table 7-2) summarizes the mineral kinetics used in this study. These reaction rate estimations were used for all simulations.

	Reaction Rates (mol m^{-2} sec^{-1})
Calcite	1.0×10^{-5}
Dolomite	1.0×10^{-7}
Magnesite	1.0×10^{-7}
Quartz	1.0×10^{-13}
Anhydrite	1.0×10^{-6}
Halite	1.0×10^{-4}
Gypsum	1.0×10^{-4}

Table 7-2: Table showing mineral kinetic reaction rates. Note that in experiments with no initial dolomite volume fraction, dolomite reaction kinetics were turned off (5×10^{-99} mol cm^2 sec^{-1}) as a result of the extreme difficulties in reproducing dolomite mineralization in laboratory environments.

7.2.5 BRINE COMPOSITION

The base brine composition used in all TR-T simulations is summarized in Table 7-3. All

species, except pH and $CO_2(aq)$, are identical in all simulations. The $CO_2(aq)$ concentration and pH concentrations tabulated in Figure 7-3 are those used in the completed dolomite-anhydrite experiment. Their values were adjusted in the sensitivity analysis.

We conducted a sensitivity analysis to evaluate the effect of varying brine pH and alkalinity, and media type. The range of alkalinity in siliclastic aquifers typically ranges

Brine Component	Concentration [M]
Na^+	7.21×10^{-1}
SO_4^{2-}	6.55×10^{-3}
Mg^{2+}	2.60×10^{-2}
Cl^-	8.46×10^{-1}
Ca^{2+}	4.56×10^{-2}
pH	8.4 **
$CO_2(aq)$	2.54×10^{-5} **

Table 7-3: Table of the dolomite-anhydrite experimental brine solution concentration. "" indicates the concentration is varied for the sensitivity simulations.**

from 50-200 mg/L, while alkalinity in carbonate aquifers is much greater, usually ranging from 200-400 mg/L (Langmuir, 1997). The dolomite-anhydrite experiment employed an alkalinity value of 305 mg/L. These reported minimum, maximum, and experimental values (input as HCO_3^-) were simulated for each media type to characterize the impact of alkalinity. Simulations representing pure quartz and pure calcite media used the appropriate published ranges for siliclastic and carbonate aquifers. Quartz alkalinity values were assigned to the quartz-evaporite media, while the carbonate alkalinity values were assigned to the quartz-carbonate media (Figure 7-4). The experimental alkalinity in the suite of siliclastic simulations is greater than the typical maximum for siliclastic

aquifers. However, such high alkalinity could be used to represent a scenario of fluid flushing from a carbonate into a siliclastic aquifer. We varied solution pH in a similar manner as alkalinity. We considered a reasonable pH range for deep basin reservoirs to be between 6.5 and 8.5. Since the solution pH in the laboratory flow experiment was calculated as 8.4, we set the upper pH limit to 8.4 instead of 8.5. As a result, pH was varied among 6.5, 7.5, and 8.4. Table 7-4 summarizes the parameters used in the sensitivity analysis. Values labeled "(P)" designate the brine fluid composition of the

PH	MEDIA TYPE	LOW VALUE [mg/L]	MED. VALUE [mg/L]	HIGH VALUE [mg/L]
6.5	Calcite Quartz-Carbonate	200	305 (P)	400
6.5	Quartz Quartz-Evaporite	50	200	305 (P)
7.5	Calcite Quartz-Carbonate	200	305 (P)	400
7.5	Quartz Quartz-Evaporite	50	200	305 (P)
8.4 (P)	Calcite Quartz-Carbonate	200	305 (P)	400
8.4 (P)	Quartz Quartz-Evaporite	50	200	305 (P)

Table 7-4: Brine alkalinity and pH ranges (LOW, MEDIUM, HIGH) for each media type of proposed laboratory experiments. Experimental values for the dolomite-anhydrite experiment are marked with a "P".

dolomite-anhydrite experiment. In total, 36 simulations were used in the sensitivity analysis to evaluate the influence of varying pH, alkalinity and media type.

7.2.6 CHEMICAL EQUATIONS

The chemical equations used by the TRANS simulator are prescribed through a modified version of the EQ3/6 thermodynamic chemical database from Wolery (1983). Table 7-5 species relations were assigned as equilibrium reactions. Therefore $CO_2(aq)$ and H_2O instantaneously partition into their associated secondary species at each time step. The mineral reactions described above are kinetically driven. This suite of chemical reactions was employed for both the sensitivity analysis and the completed dolomite-anhydrite experiment-model comparison. Table 7-5 shows the major aqueous and mineral reactions that were considered for this study.

$CO_{2(aq)} + H_2O \leftrightarrow H^+ + HCO_3^-$
$H_2O \leftrightarrow OH^- + H^+$
Quartz $\leftrightarrow SiO_{2(aq)}$
Magnesite $+ H^+ \leftrightarrow HCO_3^- Mg^{2+}$
Dolomite $+ 2H^+ \leftrightarrow HCO_3^- + Mg^{2+}$
Halite $\leftrightarrow Na^+ +$ Cl-
Calcite + H+ $\leftrightarrow Ca^{2+} + HCO_3^-$
Anhydrite $\leftrightarrow Ca^{2+} + SO_4^{2-}$

Table 7-5: Main chemical equations used in the TR-T model simulations of this study. Secondary species reactions (other than HCO3- and OH-) are not presented.

7.2.7 DOLOMITE-ANHYDRITE EXPERIMENT

In this section we compare TR-T simulator predictions to the dolomite-anhydrite experiment results. Input parameters are described below.

7.2.7.1 Input Parameters

Temperature: the core flooding system was held at 38°C, which was represented in the TR-T simulator as an isothermal system at the same temperature.

Pressure: the core flooding system uses a BPR valve to maintain fluid exit pressure above 13.79MPa. Maintaining a constant exit pressure in the TR-T simulation was achieved by assigning a Dirichlet boundary condition at the effluent cell at the same pressure.

Porosity: the initial measured dolomite-anhydrite bulk porosity of 13% was implemented as a homogeneous porosity in the model simulation.

Permeability: the initial measured bulk permeability of 30.6mD was implemented as a homogeneous permeability in the model simulation.

Injection Rate: CO_2 and brine injection was alternated several times over the course of the experiment. Less than 1 percent oil (by volume) in one time interval was also injected through the column. Oil is not modeled by EOSCO2, is not extremely reactive with geologic media on short time scales, and is a minor component of the total volume injected. Therefore, it was deemed necessary to mention but reasonable to neglect its presence in model simulations. Also since alternating injection is currently not an option in the TR-T simulator, fluid was injected at the average volumetric rate of 21.52cm^3 hr^{-1} and 33.09cm^3 hr^{-1} for the CO_2 and brine respectively. Therefore in our simulations we are

simulating constant brine-CO_2 flushing, contrary to the actual oscillating injections where pure fluid flow (either CO2 or brine) will occur for portions of the experiment. Therefore the saturation histories will be different. However, the same equivalent number of pore volumes pass through the test core, at an average rate. These input data are summarized in Table 7-6.

	Completed Experiment
Temperature	38°C
Back Pressure	13.79MPa
Initial Saturation	Brine Sat. = 1.0
Geologic Media	57% Dolomite 20% Anhydrite
Porosity	13%
Permeability	30.6 mD
CO2 Inj. Rate	21.53 cm^3 hr^{-1}
Brine Inj. Rate	33.09 cm^3 hr^{-1}
Total Simulation Time	9.584 x 10^6 seconds

Table 7-6: Input parameters of completed dolomite-anhydrite experiment

7.2.7.2 Results

Our analysis revealed model predictions were consistent with experimental results, suggesting that the TR-T model may be used to simulate subsurface CO_2 injection and its affect on geologic media, at least at the bench scale and for short time scales. Over the course of the 4 month experiment, approximately 145L of supercritical CO_2 and brine was injected into the dolomite-anhydrite core. Periodically the core assembly was depressurized and drained in order to measure the porosity of the core sample. Since the core did not need to be depressurized to measure the absolute permeability, measurements were taken when the porosity was measured, and also at several times between porosity measurements. For our analysis, we compared the TR-T simulator

predictions to experimental results when both the porosity and permeability was measured (Figure 7-4).

The solid red and blue lines represent the measured porosity and permeability, respectively, and the dashed lines indicate the TR-T model predictions in the same color scheme. The black line represents the permeability predicted by the TR-T simulator using the measured porosity data. From the simulated results, we calculated bulk permeability as a harmonic average of the permeability values from all grid cells. Comparisons are shown as a function of total injected fluid volume. Although there was some attenuation in the simulated response, our comparison revealed strong agreement between TR-T simulator predictions and experimental results. The maximum porosity difference

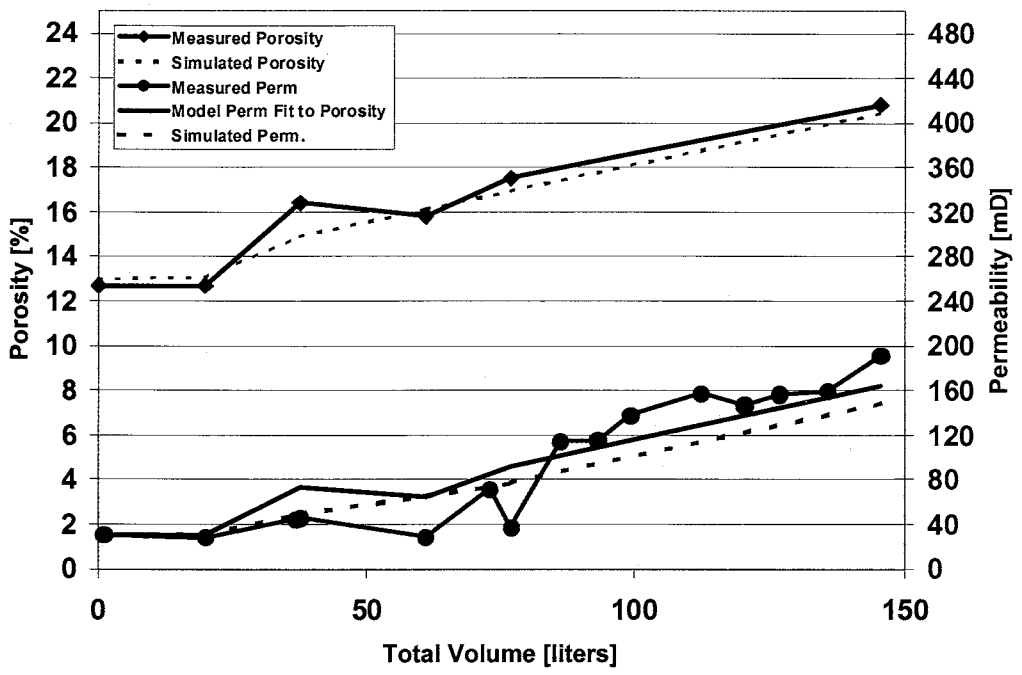

Figure 7-4: Experimental vs. simulated porosity and permeability values as a function of injected fluid volume. Red and blue solid lines represent experimental porosity and permeability values. Corresponding simulated values are shown as dashed lines as same color. The solid black line shows the predicted permeability by the TR-T model based on the measured porosity values above.

(measured - simulated) was always less than 1.5 percent, and the permeability difference (measured - simulated) was less than 20mD for much of the experiment. However, we were unsure of the potential errors induced by our experimental anhydrite-dolomite volume fraction estimation. In other words, could small changes in the anhydrite volume fraction amount to large changes in the predicted porosity through time? Was the strong agreement between predicted and measured results a product of counteracting errors? We tested the sensitivity of our estimation by simulating a dolomite-anhydrite media comprising 10 and 30 percent anhydrite volume fractions in addition to our original 20 percent estimation. Our analysis indicated only minor differences in the predicted bulk porosity through time (Figure 7-5).

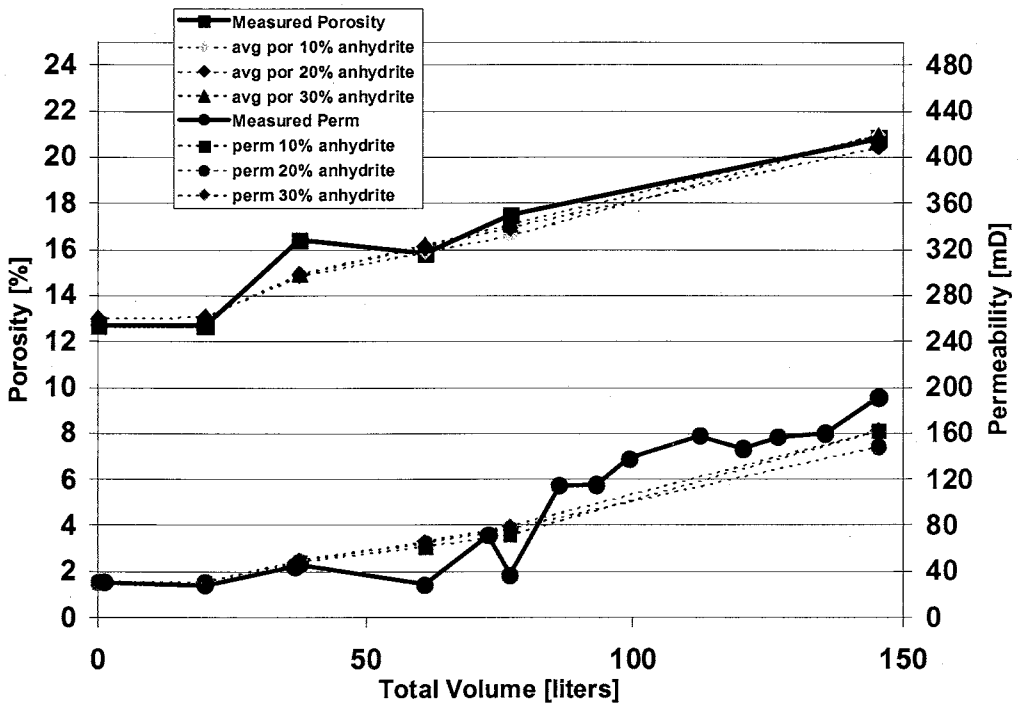

Figure 7-5: Sensitivity analysis of varying anhydrite volume fraction estimation. Plot compares TR-T porosity and permeability predictions versus measured values using anhydrite volume fractions of 10, 20, and 30 percent. Porosity was held constant at 13 percent and the residual volume fraction (1-(porosity + anhydrite)) was assigned to dolomite.

We believe the insensitivity to varying anhydrite fractions was a function of dissolution kinetics and mineral volume fraction. The magnitude of dissolved anhydrite was simulated as the product of the kinetic rate constant and the anhydrite surface area (proportional to the volume fraction). With continued anhydrite dissolution, the system must approach a threshold where the influence of the larger volume, slow reacting dolomite surpasses the influence of the diminishing, fast reacting anhydrite. Our predictions were insensitive to changes in volume fractions because our anhydrite volume fraction did not fall below this threshold value. However, we felt comfortable that the anhydrite volume fraction was above 10 percent and therefore did not pursue this threshold value specific to this system. In light of the insensitivity to our volume fraction estimation, we feel that the strong agreement between measured and predicted results supports a conclusion that the TR-T model can accurately simulate flow, transport, and chemical reactivity associated with supercritical CO_2 injection in these specific geologic media.

7.2.8 SENSITIVITY ANALYSIS

The strong agreement to measured values motivated a sensitivity analysis to determine the influence of varying brine pH and alkalinity for each of the 4 rock types. We pattered our sensitivity analysis after a pure calcite injection experiment, which was was stopped due to mechanical difficulties. The parameters in our analysis incorporated measured values from the calcite experiment.

7.2.8.1 Input Parameters

Temperature: the core flooding system was held at 38°C, which was represented in the TR-T simulator as an isothermal system at the same temperature.

Pressure: the core flooding system used a BPR valve to maintain fluid exit pressure above 13.79MPa. Maintaining a constant exit pressure in the TR-T simulation was achieved by assigning the Dirichlet boundary condition at the effluent cell at the same pressure.

Porosity: the initial measured calcite bulk porosity of 15% was implemented as a homogeneous porosity in the corresponding model simulations.

Permeability: the initial measured calcite bulk permeability of 38.4mD was implemented as a homogeneous permeability in the corresponding model simulation.

Injection Rate: the injection was set constant at 5.0×10^{1} cm^3 hr^{-1} for both CO_2 and brine. Again, these values are representative of the current calcite experiment

These parameters are summarized Table 7-7.

Results of our analysis (36 simulations) suggest there are only minor effects induced by varying pH and alkalinity under constant 50 cm^3-hr^{-1} injection rates of supercritical CO_2 and brine (Figure 7-6). The example media was calcite but similar results occurred for

	Sensitivity Analysis
Temperature	38°C
Back Pressure	13.79MPa
Initial Saturation	Brine Sat. = 1.0
Geologic Media	A) 100 % Quartz B) 40% Quartz + 30% Calcite + 15% Magnesite C) 45% Quartz + 20% Halite + 20% Gypsum D) 100% Calcite
Porosity	15%
Permeability	38.4 mD
CO_2 Inj. Rate	50 cm^3 hr^{-1}
Brine Inj. Rate	50 cm^3 hr^{-1}
Brine pH	6.5, 7.5, and 8.4
Brine Alkalinity	Carbonate: 200, 305, and 400 mg/L Siliclastic: 50, 200, and 305 mg/L
Total Simulation Time	1.50 x 10^7 seconds

Table 7-7: summary input parameters (base model) for sensitivity analysis.

each simulated rock type, at all pH and alkalinity values. The simulations indicated that there is a measurable difference in calcite dissolution under varying fluid pH and alkalinity. As expected, the most dissolution occurred in the presence of the least resistant, lowest alkalinity, lowest pH brine, and the least dissolution occurred in the most resistant, highest pH, highest alkalinity brine. The intermediate brine fell between the two end member cases. However, although the volumetric mineral difference is measurable (0-5%), it is minor in relation to the overall magnitude of dissolution within the column.

7.2.8.2Numerical Dispersion in Simulations

TR-T simulation results indicated numerical smearing (dispersion) near the injection area. We hypothesized the smearing was an artifact of the TOUGH2 simulator. We found evidence of numerical smearing by running TOUGH2 in standalone mode using the input file from the sensitivity study. Three simulations were performed varying the maximum

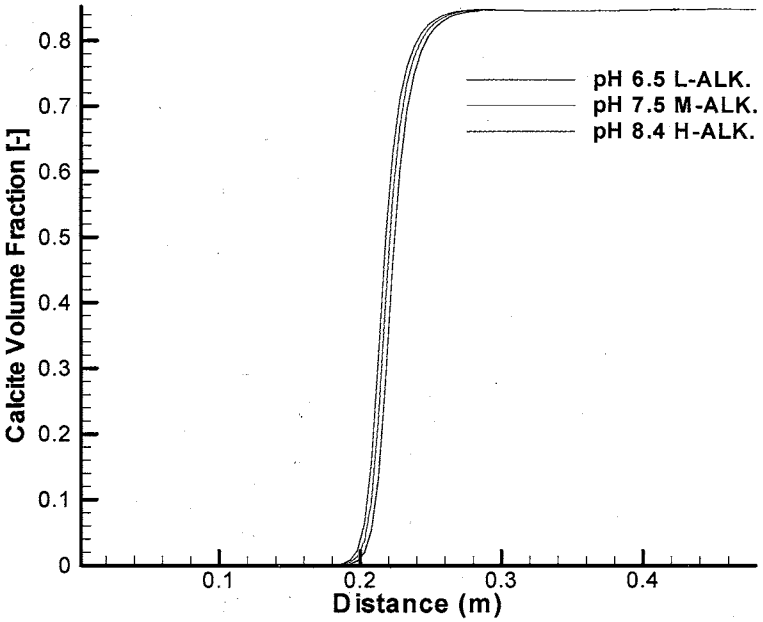

Figure 7-6: Calcite volume fraction with varying brine compositions. The least resistant brine to CO_2 acidification has a pH of 6.5 at a low alkalinity (L-ALK) and the brine most resistant to acidification to CO_2 injection has a pH of 8.4 at a high alkalinity (H-ALK). Shown is the calcite volume fraction profile at time 1.5×10^7 sec.

time step size by three orders of magnitude (Figure 7-7). The black dashed line indicates the manually calculated dissolved CO_2 from EOSCO2 (Reid et al. (1987)). The blue, green, and red lines indicate the simulated values. The test simulations revealed an increase (nonlinear) in the smearing response as the maximum time step was increased. In addition, the CO_2 solubility relation (Reid et. al, 1994) employed in EOSCO2 is positively correlated with pressure. Therefore, dissolved CO_2 concentration should be greatest near injection, where the pressure is the greatest. This is not the case. TOUGH2 predicts lower dissolved CO_2 concentrations near the injection area. In general the laboratory experiments were very difficult to simulate. In comparison to Cole (1999), the experimental injection rate to cell volume ratio was 4-5 orders greater in magnitude, which required injection of fluids to be partitioned across the first 4 grid cells. The

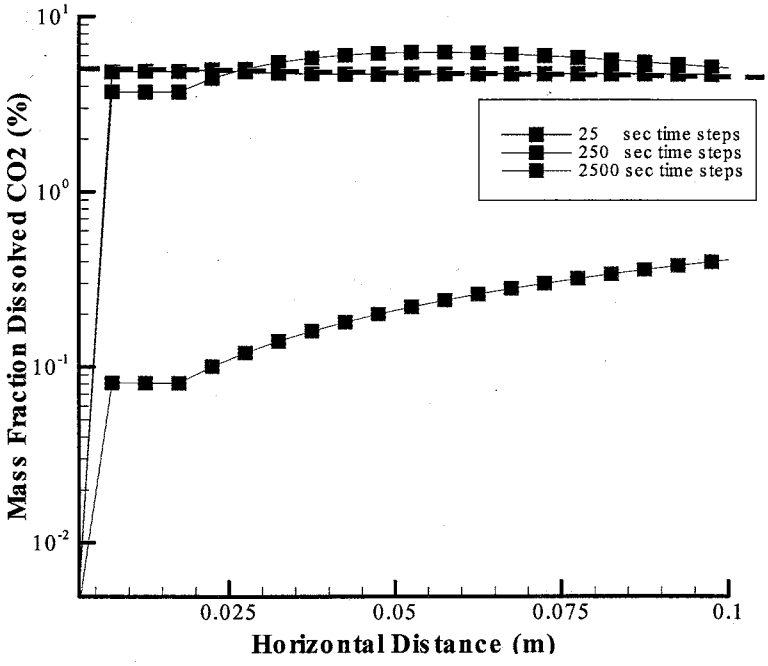

Figure 7-7: Affect of increasing time step in TOUGH2 at the first .1m of the simulated domain. The dashed black line indicates the results from a manual mass fraction calculation using the Reid et al. (1987) relation in EOSCO2. There is little difference in the profiles using 25 and 250 sec time step. However, the 2500 sec time step shows evidence of significant numerical smearing. Note units are in percent X_{CO2}.

extreme injection rates may be the cause of the numerical dispersion. Also, perhaps an alternative experimental representation (input model) in the TR-T simulator would improve results. However, integration of the aqueous CO_2 concentration with distance along the core would show that numerical dispersion occurs over a relatively small area. As further support TR-T predictions of the completed dolomite-anhydrite experiment were in strong agreement with measured results. In short, we chose a time step that allowed for moderate numerical smearing but large enough to allow for reasonable simulation run times.

7.2.8.3 Results

In light of these minor differences in physical changes to the media and for the purpose of brevity, graphical output was restricted to simulations using the brine solution with pH 8.4, and 305mg/L alkalinity. The results are similar for all pH values and alkalinity of each simulated lithology.

For our analysis, we compared the response of each media type under constant injection of CO_2 and brine. Simulation time was limited to 1.50×10^7 seconds (~6 months), the maximum expected duration of future laboratory experiments. For each media, the upper two subplots show the aqueous profiles at 1.0×10^5 seconds (T1), near the beginning of the simulation, and near the end of simulation at 1.25×10^7 seconds (T2). The lower two subplots show the corresponding mineral volume fraction at T1 and T2 (Figure 7-8).

Our simulation results suggest that the pure quartz sandstone was the least reactive media (Figure 7-8). Quartz reaction kinetic rates are orders of magnitude slower than most carbonates minerals (Stumm, 1990). As a result, negligible matrix changes were observed over the ~6 month simulated time scale. CO_2 dissolution in the brine dropped pH from 8.4 to 3.3. All other species concentrations were unaffected by the CO_2 or quartz media and remained constant. Results of the quartz simulations indicate that chemical processes associated with CO_2 and brine injection in pure quartz sandstone are minor.

Contrary to the pure quartz media, the simulated quartz-evaporite sandstone showed significant matrix changes due to CO_2 and brine injection (Figure 7-9). As with the pure

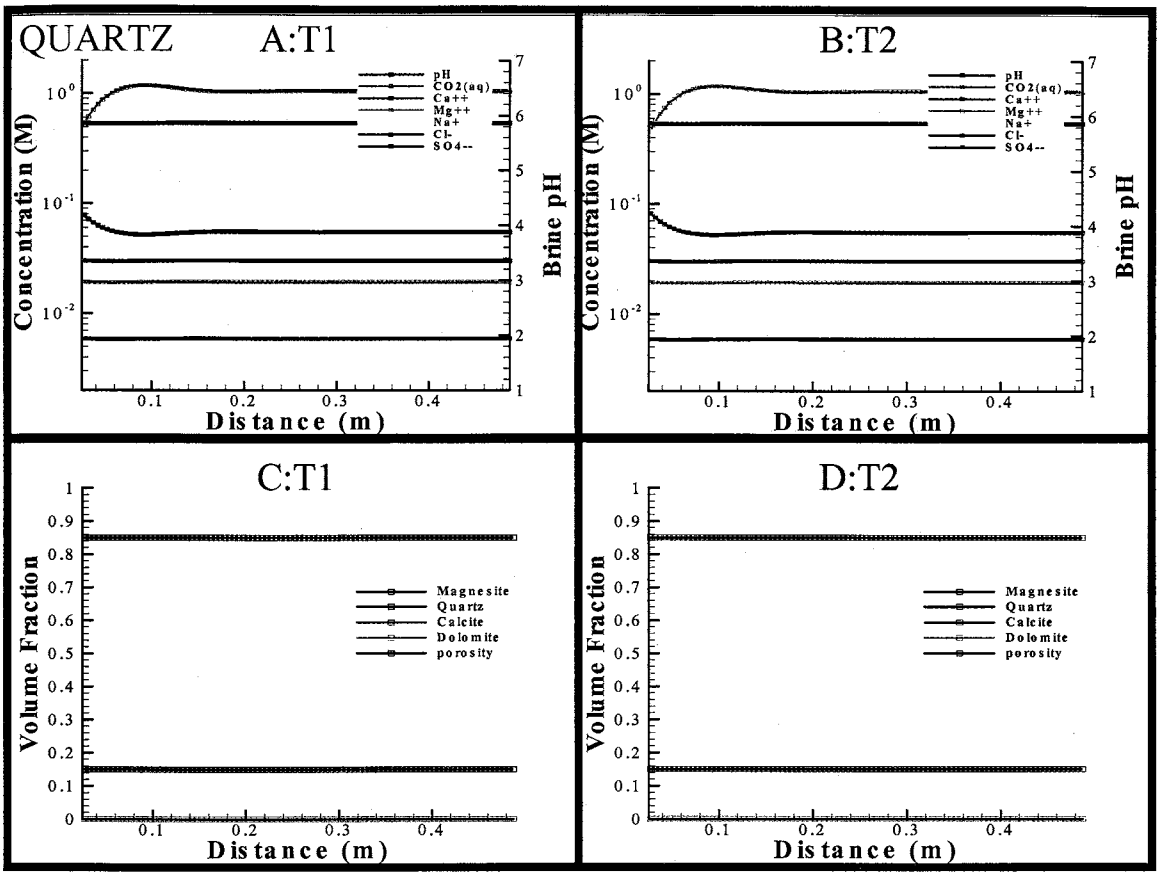

Figure 7-8: TR-T simulation results for the quartz media. The upper two subplots show the aqueous species concentrations at 1.0 x 10^5 seconds (T1) and 1.25 x 10^7 (T2) from left to right. The lower two subplots show the corresponding volume fractions at each corresponding times T1 and T2.

quartz media, the maximum dissolved CO_2 reaches ~1 M and pH decreases to 3.3. At 1.0 x 10^5 seconds (A), Na^+ and Cl^- concentrations increase from ~.4 M to approximately 2M across the column. At the same time, SO_4^{2-} and Ca^{2+} concentrations double across the column. The increase in concentration along the column is likely an indication that fluid flow is fast relative to the mineral reaction rates and brine saturation concentrations. In other words, with smaller Damkohler numbers we expect these concentration increases of chemical species across the column to attenuate. The reason for the disparity in the species concentration is preferential mineral dissolution. At early time in the simulation

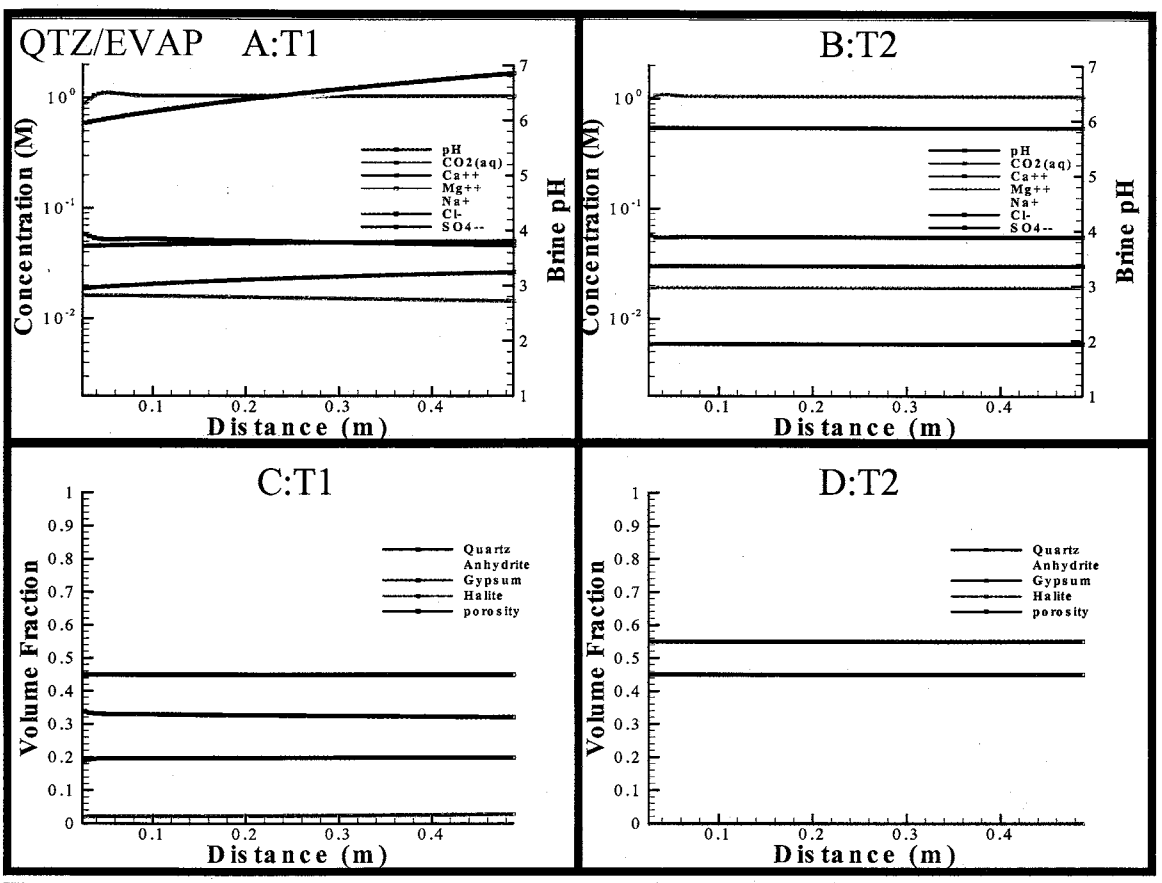

Figure 7-9:TR-T simulation results for the quartz-evaporite media. The upper two subplots show the aqueous species concentrations at 1.0 x 10^5 seconds (T1) and 1.25 x 10^7 (T2) from left to right. The lower two subplots show the corresponding volume fractions at each corresponding times T1 and T2.

the majority of the dissolution is from halite (panel C, Figure 7-9) Once halite is nearly dissolved, gypsum dissolution dominates, suggesting that the mineral controls on this system are time-dependent. However, by the end of the 6 month simulation, all of the evaporite minerals have dissolved (panel D, Figure 7-9) demonstrating that significant matrix changes may result on short time scales when both CO_2 and brine fluids are flushed through evaporite rock assemblages

The quartz-carbonate sandstone also showed significant dissolution but less pronounced

than that of the quartz-evaporite media (Figure 7-10). In agreement with previous results, the aqueous CO_2 concentration remained constant at ~1 M throughout the simulation. In the initial stages of injection the brine pH is 5 (Panel A, Figure 7-10). The cause of the elevated pH is carbonate dissolution, buffering the brine from the effects of CO_2 acidification. Mg^{2+} concentration linearly increased from 1 x 10^{-2} to 3 x 10^{-2} M across the column, indicating that the rate of magnesite dissolution limited brine-magnesite equilibrium. Otherwise the Mg^{2+} would have reached its maximum concentration near the injection area and remained constant throughout the column. We expected Ca^{2+}concentrations to increase across the column in a similar fashion. However, the Ca^{2+} exhibited a curvature, which was a product of numerical smearing of the dissolved CO_2 as described above. At 1.0 x 10^7 seconds the carbonates nearly dissolved, which reduced the buffering of the brine solution. As a result pH was held at ~3.8 from 0 to 0.4 m along the column. At .4 m significant calcite remained (panel D, Figure 7-10) and the solution pH increased back up to ~5 (panel B,). However, contrary to models of other media, this model predicts calcite mineralization of approximately 1 x 10^{-1} volume fraction from .4 m to .5m along the core. If such a phenomenon does indeed occur, it may benefit CO_2 sequestration in two ways. First, dissolution near the injection site may increase storage capacity within the medium, increasing localized CO_2 storage. Second, mineralization may act to reduce the matrix permeability and subsequently CO_2 mobility near the outer boundaries of the main plume In tandem, dissolving the matrix should increase local storage, whereupon carbonate species within the flushed brine solution precipitate at some downstream location. In this manner, CO_2 injection may act as a self-sealing mechanism. However, only 5 percent of the dissolved carbonates re-precipitated at the

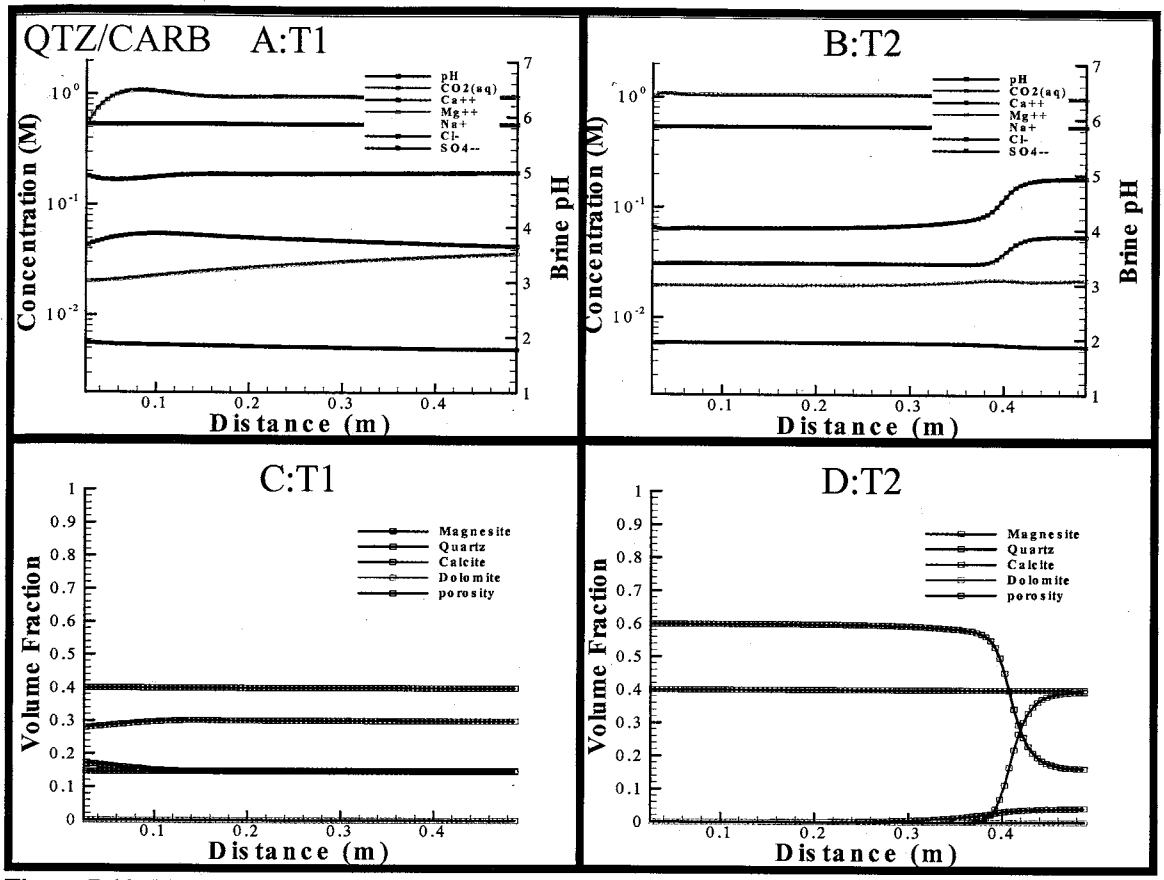

Figure 7-10: TR-T simulation results for the quartz-carbonate media. The upper two subplots show the aqueous species concentrations at 1.0 x 10^5 seconds (T1) and 1.25 x 10^7 seconds (T2) from left to right. The lower two subplots show the corresponding volume fractions at each corresponding times T1 and T2.

tail end of the column. If our bench scale simulation were representative of a basin scale response the amount of CO_2 flushing required to seal the media would preclude it as a viable mechanism to reduce permeability. However, if dissolution and subsequent precipitation create concentric sealing layers around the injection location, significant sealing potential may result. In summary, the results suggest that carbonate minerals within quartz sandstone show significant dissolution in CO_2 acidified brine, and that near injection dissolution may induce down stream carbonate precipitation.

The calcite simulations revealed the same magnitude of dissolution as the quartz-

carbonate (Figure 7-11). The fluid injection rates were identical in each simulation, but the reactive volume fraction (considering quartz as essentially nonreactive) was 2.22 times greater in the pure calcite media. Therefore, if the dissolution was purely a function of the reactive media we should have observed greater matrix changes due to the larger reactive surface of the pure calcite media. However this was not the case. Increasing the reactive surface area (pure calcite) had little effect on the bulk dissolution. We concluded there must be a minimum mineral volume below which decreasing mineral fractions will alter chemical processes. We encountered the same effect in the dolomite-anhydrite experiment, where simulations of varying mineral fractions produced similar magnitudes of mineral dissolution.

The TR-T model was shown to quantitatively replicate the outcome of the dolomite-anhydrite CO_2 and brine injection experiment. Supported by the strong agreement to experimental results, a sensitivity analysis was performed to determine which parameters control the interaction of CO_2, brine, and geologic media under deep basin pressure-temperature conditions. Simulation results, using the experimental brine composition, indicate that varying brine pH and alkalinity caused 0-5% differences on the resultant volumetric mineral fractions. The major controlling influence was found to be lithology type, while in the case of the quartz-evaporite media dissolution may be time-dependent. A secondary influence was the magnitude of fluid flushed through the media in relation to the reactive surface area.

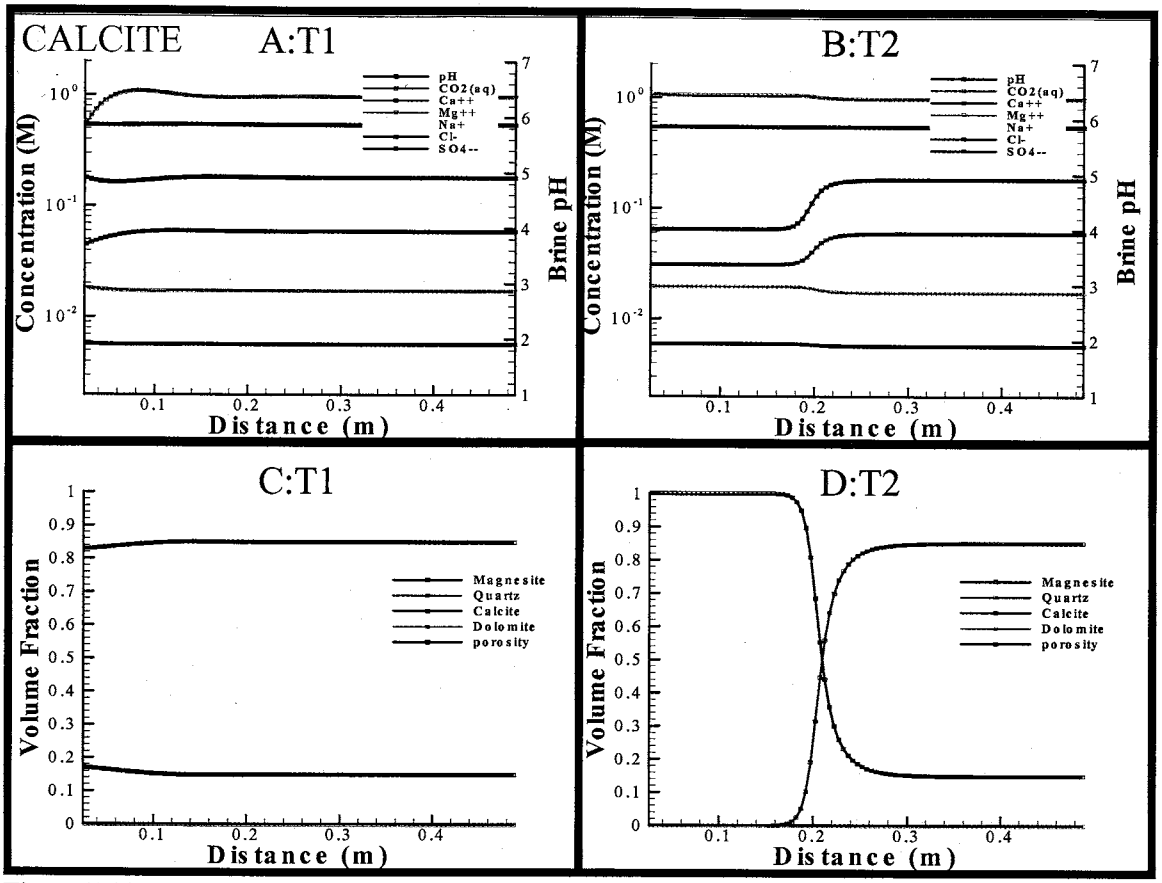

Figure 7-11: TR-T simulation results for the calcite media. The upper two subplots show the aqueous species concentrations at 1.0 x 10^5 seconds (T1) and 1.25 x 10^7 (T2) from left to right. The lower two subplots show the corresponding volume fractions at each corresponding times T1 and T2.

7.3 RESERVOIR SCALE SIMULATION

Although experiments and our modeling results suggest that reactive transport processes can significantly alter permeability and porosity at the bench scale, the ultimate goal of our project is to determine whether these processes are significant at the basin scale. At the basin scale, buoyancy forces, pressure and temperature gradients, and permeability heterogeneity are introduced, all of which may have a significant influence on chemical reactions within a specific geologic system. In addition, the CO_2 and brine simulations discussed above represented high fluid velocities encountered near an injection well, which decrease substantially with distance from the injection site. Furthermore, the

relative saturation of injected fluid would likely decrease as a function of distance from an injection well. Thus, although bench scale experiments are of paramount importance to understanding CO_2-brine-media interactions, temporal and spatial up-scaling are ultimately required to understand the impact of such processes at the reservoir scale.

Although reactive transport processes significantly altered permeability and porosity at the bench scale, the ultimate goal of our project group is to determine whether these processes are significant at the basin scale. At the basin scale, buoyancy forces, pressure and temperature gradients, and permeability heterogeneity are introduced, which may have a significant influence on the chemical reactions within a specific geologic system. In addition, the CO_2 and brine simulations shown above represented high fluid velocities encountered near an injection well, which decrease substantially with distance from the injection site. Furthermore, the relative saturation of injected fluid would likely decrease as a function of distance from an injection well. So, although bench scale experiments are of paramount importance to understanding CO_2-brine-media interactions, up scaling is ultimately required to understand the impact of such processes at the reservoir scale.

7.3.1 RESERVOIR DOMAIN AND INPUT SPECIFICATIONS

We conducted a test simulation of a reservoir model (5 km x 5 km) to lead future studies (Figure 7-12). We injected CO_2 (prograde cycle) at a constant rate for 100 years, followed by a 900-year shut in period of non-injection (retrograde cycle). CO_2 was injected at a depth of 2450m in the center of the model domain, denoted by the black dot (Figure 7-12). We prescribed Neuman (no flow) boundary conditions at the vertical

edges of the model, and assigned upper and lower boundary rows Dirichlet (constant head) boundary conditions. Initial assigned pressure was increased with depth at a rate of 9.8MPa/km. Initial assigned temperature was increased with depth at a rate of 25°C km^{-1}, from 15°C at the simulated ground surface (0m depth). The simulated media was pure calcite with an initial horizontal permeability of 1.0 x 10^{-15} m^2, two orders of magnitude greater than the initial vertical permeability of 1.0 x 10^{-17} m^2. The input parameters for this test simulation are summarized in Table 7-8. We initially saturated the reservoir with brine. The brine composition was identical to the pH 6.5, 200mg/L alkalinity solution used in the bench scale calcite simulation. We injected CO_2 for 100 years at a constant

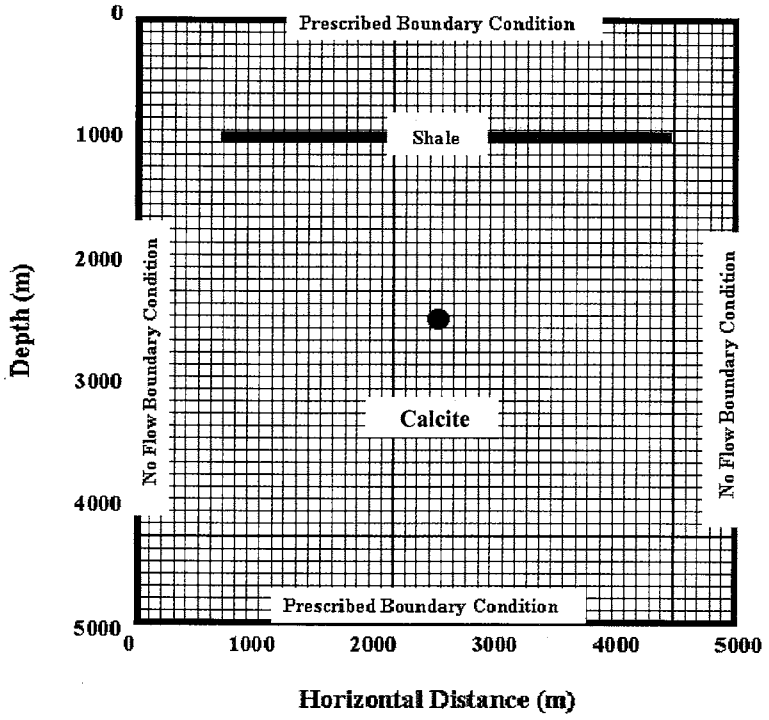

Figure 7-12: 2-D reservoir cross-section model domain used in simulation. Constant head boundary conditions were assigned at the upper and lower level rows. No flow boundary conditions were assigned at the vertical boundary cells. The media was pure calcite throughout the aquifer with the exception of the nonreactive shale capping layer.

rate of .7 kg sec^{-1} at a depth of 2450 meters (prograde) cycle. The total simulation time was 1000 years.

7.3.2 AQUEOUS CO_2 RESULTS

(Figure 7-13) illustrates an isometric projection of aqueous CO_2 concentration at 1000 years. The dissolved CO_2 plume extended across nearly 50 percent (2500m) of the lateral extent of the basin and approximately 500 hundred meters in the vertical direction. The plume "cap" was flattened, indicating maximum solubility of dissolved CO_2. The maximum dissolved mass fraction of CO_2 reaches approximately 4 percent. In this simulation the intrinsic permeability is low, restricting gravity segregation between the

	Completed Experiment
Temperature	25°C km^{-1}
Back Pressure	9.81MPa km^{-1}
Initial Saturation	Brine Sat. = 1.0
Capping layer Lithology	Shale
Shale Porosity	5%
Shale Vertical Permeability	1.0×10^{-17} m^2
Shale Horizontal Permeability	1.0×10^{-15} m^2
Reservoir Lithology	Calcite
Calcite Porosity	15%
Calcite Vertical Permeability	1.0×10^{-20} m^2
Calcite Horizontal Permeability	1.0×10^{-18} m^2
CO_2 Injection Rate	7.0×10^{-1} kg sec^{-1}
Injection Depth	2450m
Total Simulation Time	1000 years

Table 7-8: Model parameter specifications for the 2 dimensional basin simulation.

supercritical CO_2 and brine. The elongated shape of the plume in the horizontal direction corresponded to the higher absolute permeability in the horizontal direction.

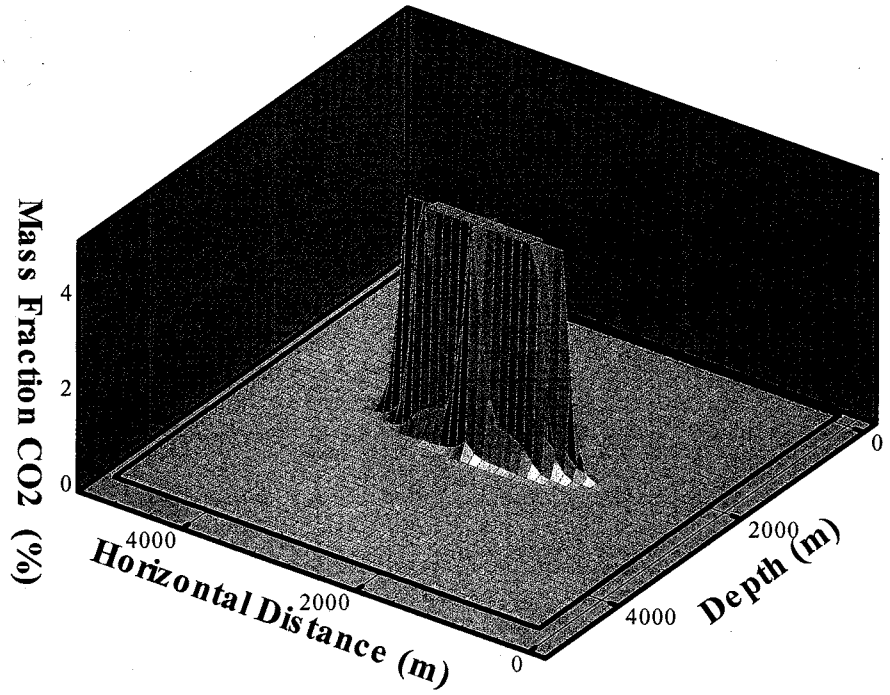

Figure 7-13: Mass fraction dissolved phase CO_2 at 1000 years

As a means to identify the influence of fluid-media interactions we compared the predicted dissolved CO_2 distribution in the TR-T and TOUGH2-EOSCO2 simulators. Figure 7-14 is a contour representation of the isometric plot above (Figure 7-13), showing the dissolved CO_2 distribution at 1000 years. We found that the dissolved mass fraction distributions for both models are closely matched or consistent with each other. Closer examination illustrates that the contours are slightly off center of one another, but overall the concentration profiles indicated that chemical reactions play a negligible role on the dissolved phase CO_2 distribution.

7.3.3 SEPARATE PHASE CO_2 RESULTS

Separate phase CO_2, in this case completely supercritical, displayed similar plume

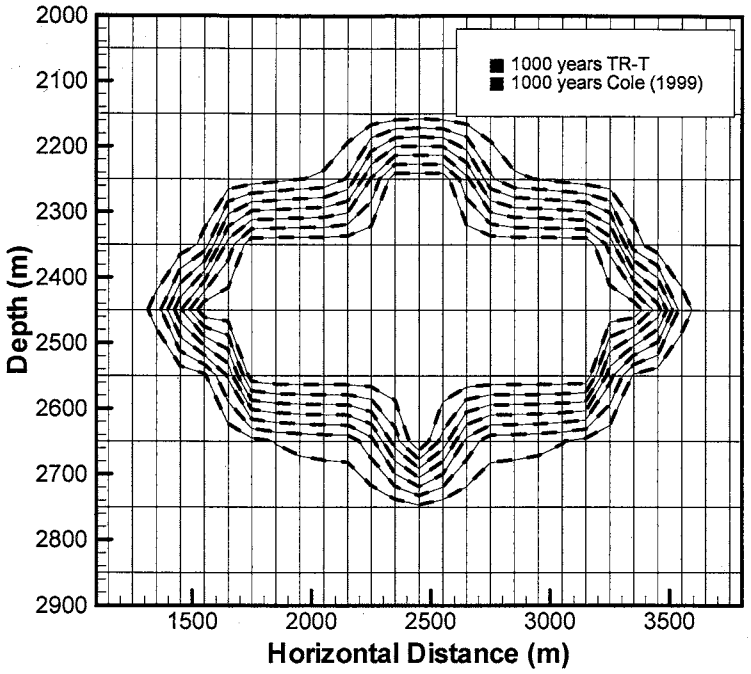

Figure 7-14: Dissolved phase CO_2 distribution comparison using the TOUGH2-EOSCO2 and TR-T simulators. The simulation time is 1000 years. Contours range from 0-4 percent dissolved mass fraction

geometry as the dissolved mass fraction CO_2 (Figure 7-15). The same attenuated shape was produced by the higher permeability in the horizontal direction. The peak of the saturation phase was more pronounced, however, revealing that a larger proportion of separate phase fluid remained longer near the injection location. Peak saturation was approximately 70 percent at the injection cell. saturation distributions to assess the influence of chemical processes (Figure 7-16), and again superimposed 2-D contour plots at 1000 years for comparison. As was the case with the dissolved mass fraction comparison, negligible differences between results of the two models occurred, indicating that chemical processes played a minor role in the distribution of separate phase CO_2. As with the dissolved mass fraction comparison, we compared TOUGH2 and TR-T

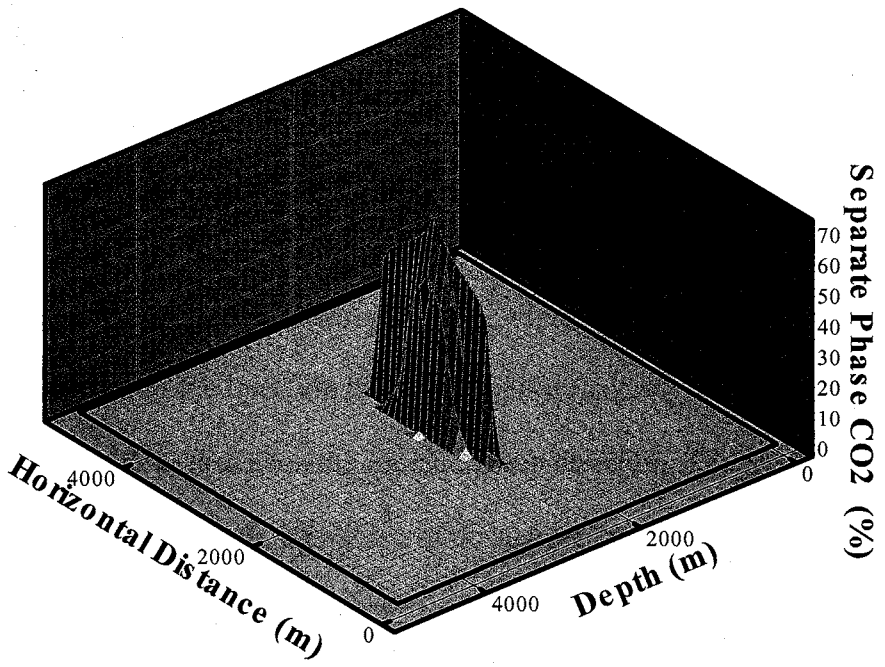

Figure 7-15: Separate Phase CO_2, in this case purely in the supercritical state at 1000 years.

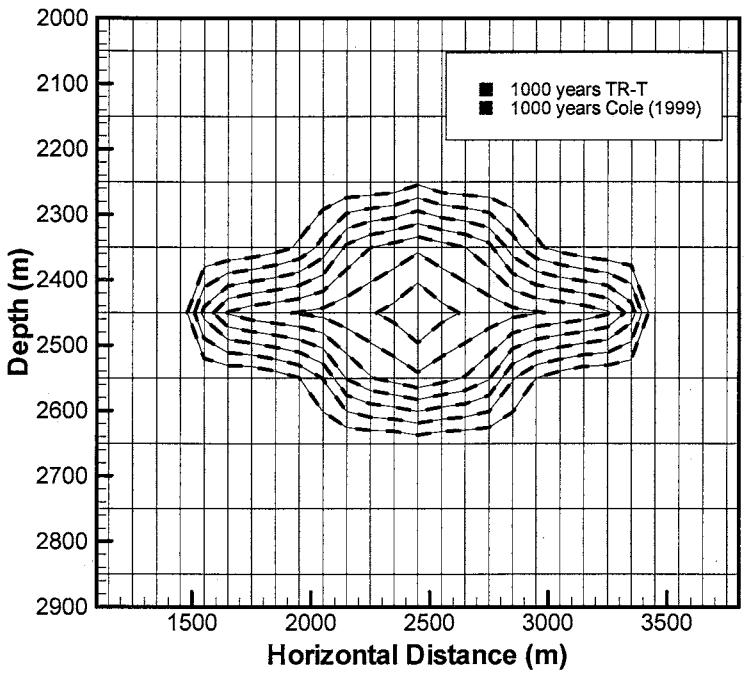

Figure 7-16: Saturation phase CO_2 distribution comparison using the TOUGH2-EOSCO2 and TR-T simulators. The simulation time is 1000 years. Contours range from 0-70 percent saturation separate phase CO_2.

7.3.4 PH RESULTS

Although the CO_2 distributions were similar, the effect of CO_2 injection on brine pH was extreme. A dramatic decrease in system pH occurred throughout the injection area during the 100-year injection period. The extent of the pH depression "plume" at 1000 years grew to nearly 3 km in length and 1 km in height (Figure 7-17). PH was slightly more depressed near the injection location, displaying nearly equivalent pH approximately .5km from the source in each direction. The pH profile was somewhat curvilinear with depth, a function of the temperature gradient affecting calcite solubility. Such drastic decreases in pH may cause significant changes to the matrix due to brine acidification by dissolved CO_2 in solution.

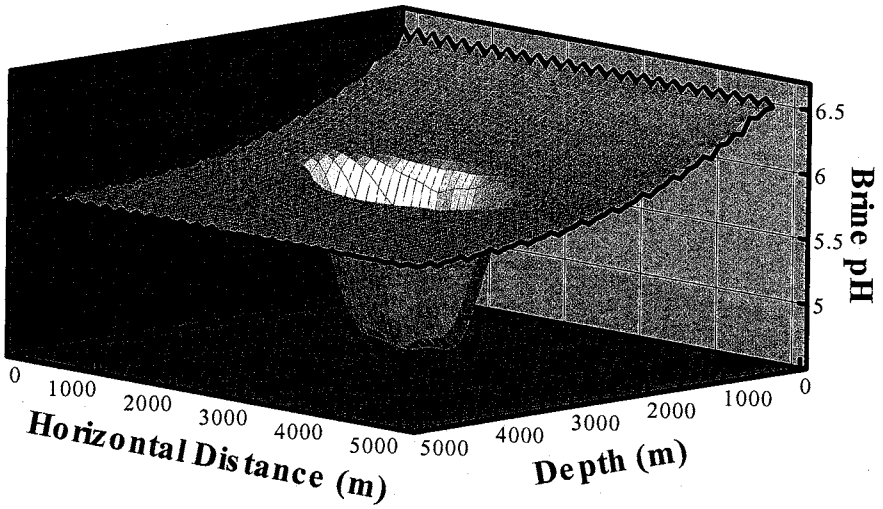

Figure 7-17: Simulated pH depression "plume" at 1000 years.

7.3.5 CALCITE VOLUME FRACTION RESULTS

The TR-T simulator predicted only minor calcite dissolution at the reservoir scale during the first 1000 years, contrary to both the simulation results of the calcite bench scale

simulation and completed dolomite-anhydrite experiment (Figure 7-18). The migration pattern of calcite dissolution exhibits a similar shape and location as that of the dissolved and separate phase CO_2 plume, but the percentage of mineral dissolution is far less compared to the calcite bench scale results. In the calcite bench scale simulations, roughly 45 percent of the total volume fraction dissolved but less than 1/100 of a percent dissolved in the larger scale model. Furthermore, since the kinetic reaction rates of calcite were rather rapid in relation to the simulation time and the source of CO_2 was removed at 100 years, arguably little additional chemical reactions with the media should occur after 1000 years. There could be some additional reactions with the media as the plume migrates further towards the surface due to buoyancy, but these reactions would probably be no more pronounced than when the CO_2 was being injected. This begs the following question: why does the TR-T simulator predict negligible dissolution at the basin scale, when both the bench scale simulations and experimental results reveal significant dissolution?

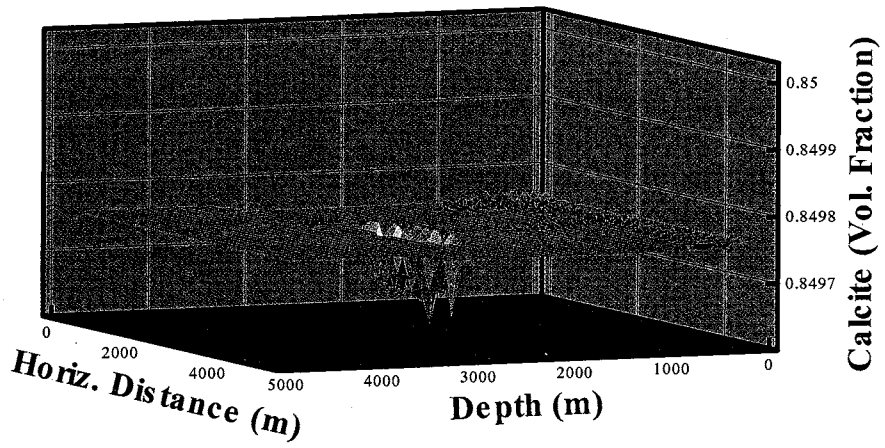

Figure 7-18: Calcite dissolution predicted by the TR-T model. Note the scale for the calcite volume fraction. Dissolution occurs but is minor.

7.4 FIELD SCALE SIMULATION

To understand the cause for the discrepancy in simulated dissolution, we performed an additional simulation using a field scale grid domain, measuring 11m x 11m, centered about the injection cell of the reservoir scale model. Our initial conditions were equivalent to those in the same location in the reservoir scale model. Identical boundary conditions to the reservoir scale model were implemented, allowing fluid flow into the upper and lower rows prescribed as Dirichlet boundary cells. As in the reservoir model, we injected CO_2 at a rate of 7×10^{-1} kg sec^{-1}. (Figure 7-19) shows the mass fraction of the dissolved phase CO_2 for the first few hours of the injection, after which the dissolved mass fraction of CO_2 remained essentially constant for the remainder of the simulation. The observed pattern for the first few hours was an outward expanding dissolved phaseCO_2 plume, which after 1.5×10^4 seconds reached the maximum dissolved CO_2 concentration throughout the remainder of the simulation. Figure 7-20 shows the corresponding supercritical CO_2 saturation. Of particular importance is the saturation of supercritical CO_2, exceeding 65 percent at 1.0×10^4 seconds. We hypothesize that at high saturations separate phase CO_2 limits brine mobility. The relative permeability relations used in EOSCO2 were taken after Parker et al. (1987), which are in good agreement with laboratory data (Holt et al., 1995) (Figure 7-21). Parker et al. (1987) showed that when NAPL saturation reached upwards of 65%, the relative permeability of H_2O was reduced to near zero. In the context of these simulations, our hypothesis suggests that when brine saturation decreased, the pressure required to overcome capillary pressure and mobilize additional brine within the pore space also increased. Both of these processes perhaps act to immobilize the brine within the pore space. Since the brine was immobile, it quickly became saturated with respect to CO_2, and the resulting magnitude of dissolution was

minor.

Our idealized model predicted a supercritical CO_2 plume to expand concentrically from the injection well, displacing the majority of the brine solution, and we hypothesize that immobilized residual brine is left behind the plume front. As a result, repeated CO_2 and brineflushing through the same rock volume is prevented, limiting mineral dissolution. Our alternative hypothesis was that the ratio of injected CO_2 to calcite mineral volume was simply much greater at the bench scale, accounting for the observed differences in mineral dissolution (bench versus reservoir scale). The total CO_2 injected through the 1-D

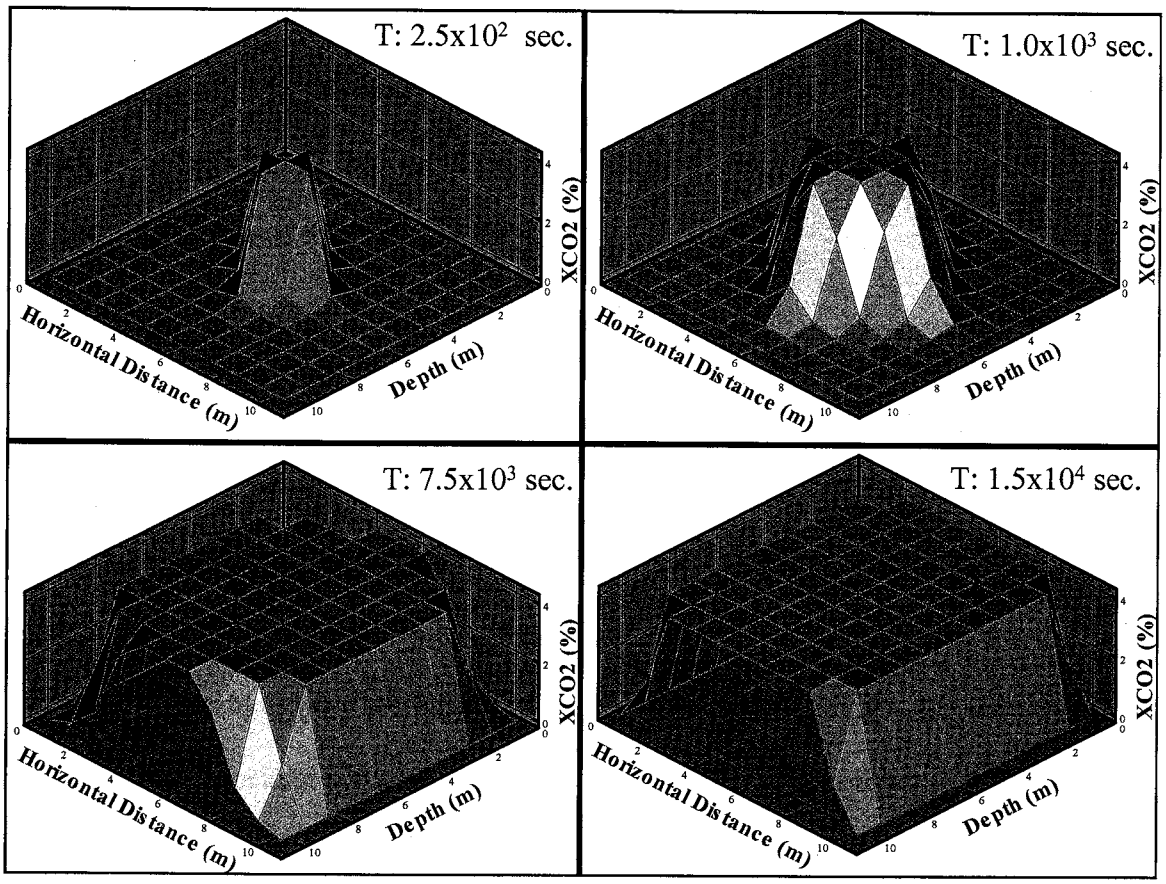

Figure 7-19: Mass fraction of dissolved CO_2 through time near the injection site

benchscale core was 150 kg, and the ratio of injected CO_2 to core volume was ~1.5 x 10^5 kg per m^3. The injection-media ratio through the injection cell in the reservoir simulation was ~2.2 x 10^4 kg per m^3. Therefore there was proportionally 6.8 times more CO_2 injected at the bench scale in relation to core volume. We hypothesize of two potential causes for the discrepancy in simulated calcite dissolution. First, the injected CO_2 to mineral volume was 6.8 times greater at the bench scale and the magnitude of CO_2 injected at the reservoir scale was insufficient to cause significant dissolution. Second, the lack of heterogeneity and course grid resolution retarded fluid mixing and subsequently significant dissolution. In any event, our model is highly simplified and is intended as an introduction to the next phase of our research, simulating CO_2 injection at the basin scale. In our future research we will incorporate more complex, representative systems. The results of future research may indicate that the influence of chemical processes at the basin scale may be significant.

7.5 SIMULATION-EXPERIMENT SUMMARY AND CONCLUSIONS

The TR-T model was shown to quantitatively replicate the outcome of the dolomite-anhydrite experiment. Porosity agreement was within 1.5 percent and permeability agreement was within 20mD for much of the experiment. Simulated porosity and permeability changes were more attenuated than in the measured data, but the general trends were in excellent agreement. Additional analysis varying anhydrite volume fraction 10-30 percent produced similar results. We found that a greater reactive mineral fraction did not amount to greater physical changes to the matrix.

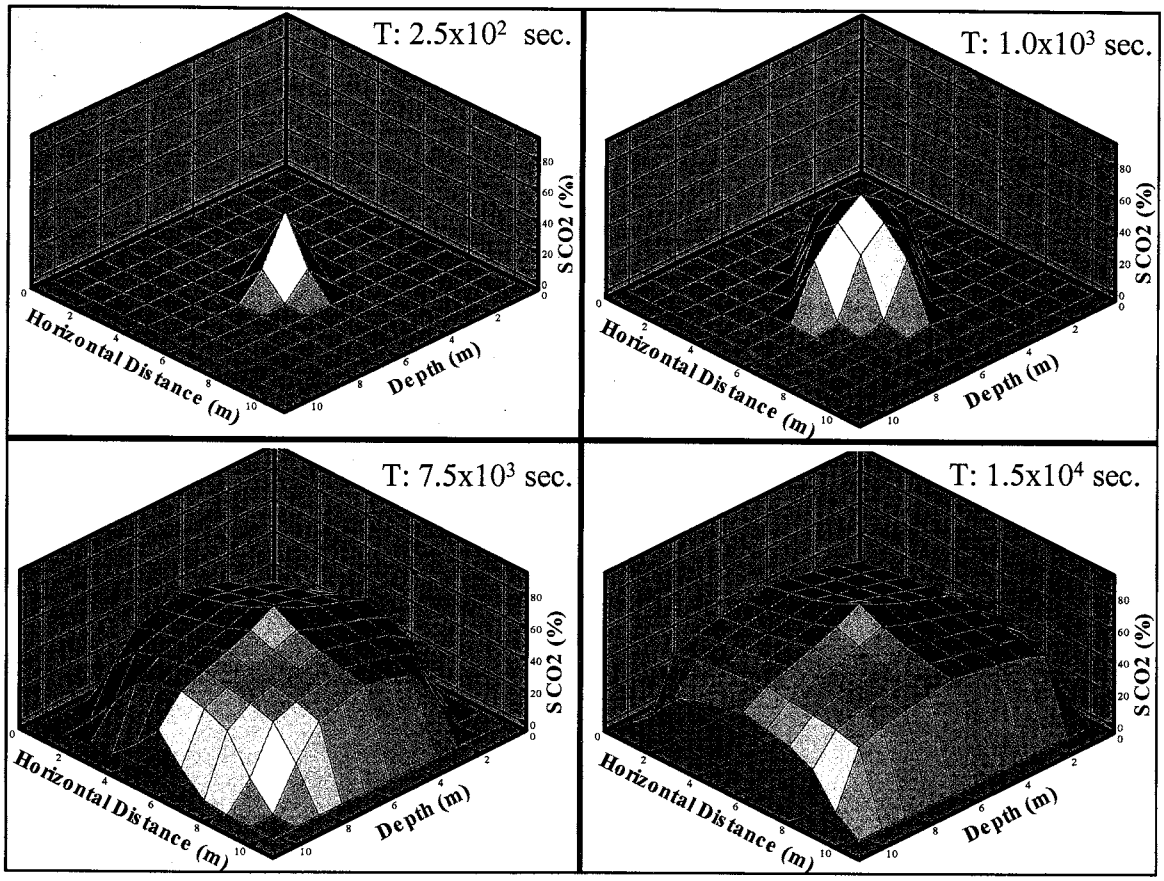

Figure 7-20: Separate phase saturation through time near the injection site

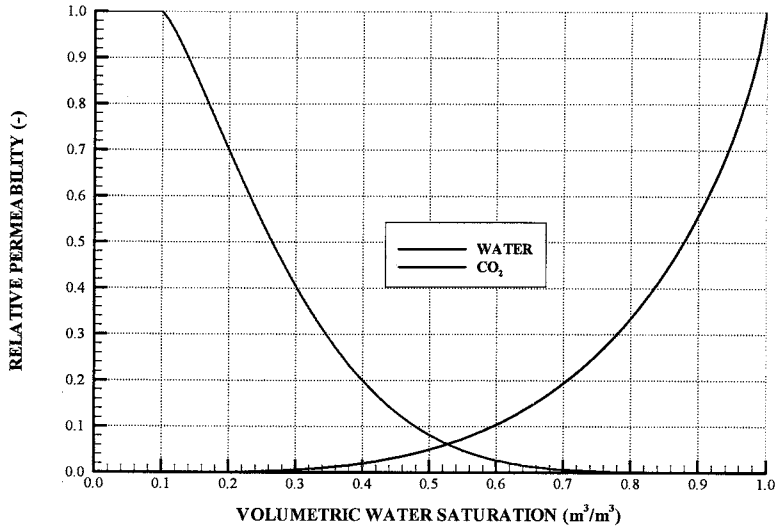

Figure 7-21: Relative permeability of Brine and NAPL(CO_2) from Parker et al., (1987). Figure was taken from Cole (1999)

Varying brine pH and alkalinity, between reported ranges for siliclastic and carbonate aquifers, altered the total mineral fraction 0-5%. However, we held ambient temperature and back-pressure constant, which would affect solubility. Future studies should investigate the effects of varying temperature, pressure, and brine composition. If we determine that fluid-mineral interactions in a specific reservoir are unaffected by (insensitive to) brine composition, then using estimated brine compositions should not preclude an accurate prediction. If such is the case, efforts could be focused towards parameterizing more sensitive model input. It is possible that brine composition is always a secondary influence under any condition and accurate characterization of lithology is the dominant factor. In this case, we should focus our efforts toward characterizing the lithology.

Our bench scale quartz simulation indicated negligible dissolution/precipitation after 1.25 x 10^7 seconds of injection. Although quartz arenite sandstone exists, it is likely that most reservoirs will contain other minerals in addition to quartz. Therefore we expect a virtually nonreactive matrix to be an anomaly.

The bench scale quartz-evaporite simulations revealed time dependent dissolution of matrix components. Results at 1 x 10^5 seconds predicted linearly increasing Na^+ and Cl^- profiles across the column. Halite was more soluble and had a faster reaction rate than dolomite. As a result, halite dissolution occurred early in the experiment, followed by gypsum dissolution in later part of the simulation. We expect CO_2 injection to induce time-dependent dissolution in many multi-media systems.

Contrary to other media, the quartz carbonate bench-scale simulation predicted mineral precipitation. Calcite precipitation occurred from .4 to .5 m of the column. However, upstream of the precipitation, nearly 80 percent of the carbonate dissolved. The implications of dissolution are usually negative in terms of CO_2 sequestration, as dissolution tends to increase permeability and subsequently CO_2 mobility. However, dissolution near injection will increase local storage potential and may help constrain the CO_2 plume. In addition, calcite mineralization may retard the CO_2 plume migration. Mineralization is the most favorable form of CO_2 sequestration since the phase transition into the solid form immobilizes CO_2. However, in this simulation 80 percent of the carbonate dissolved and only 5 percent re-precipitated at the tail end of the column. Therefore CO_2 injection induced additional aqueous CO_2, in addition to that injected. Perhaps in future projects we can identify systems where the precipitation/dissolution ratios are much greater. If we can identify the controlling parameters that enhance precipitation, perhaps we can engineer processes to mimic these ideal conditions and significantly increase CO_2 storage potential.

The calcite bench-scale simulation showed nearly the same magnitude of dissolution as the quartz carbonate simulation. We found increasing the reactive surface area had little effect on the bulk dissolution. As a result, we hypothesized of a system specific minimum volume fraction, above which increasing mineral fractions have little affect on fluid-media interactions. We observed the same effect in the dolomite-anhydrite experiment, where simulations of varying mineral fractions had no effect on the magnitude of mineral

dissolution. As a future project we intend to quantify these system specific mimimum mineral fractions to guide future simulations.

Reservoir scale simulations of CO_2 injection into a pure calcite medium predicted negligible dissolution, contrary to the bench scale simulations with the same media and fluid compositions. The disparity between the predicted results may be due to the displacement of the brine fluid by the expanding supercritical CO_2 plume. The expanded supercritical plume prevented multiple pore volumes of reactive aqueous CO_2/brine from passing through the same rock volume as in the case of the bench scale simulations. The reservoir scale simulation suggests that in homogeneous, quiescent, closed basin environments, subsurface mineral reactions may be minor on the 1000-year time scale. However, the injected CO_2 to rock volume was 6.8 times greater at the bench scale as compared to the reservoir scale. In any event, our simple model was meant as an introduction to larger scale processes. The results presented here may not be representative of a true reservoir response to CO_2 injection. For instance, incorporating permeability heterogeneity may promote the mixing necessary to induce significant dissolution similar to that in the bench scale experiment and simulations. Upscaling to larger and more complex systems is the focus of our future work.

In summary, we believe the excellent agreement between TR-T simulator predictions and experiment results is strong support that our model can be used to accurately predict CO_2-brine-media interactions at the bench scale. However, future comparisons between laboratory results and TR-T simulations are required to better understand these

interactions. Specifically we need to quantify the effects of CO_2 injection on the absolute permeability and porosity of various geologic media in specific basin environments. Results from future laboratory experiments will aid in better model parameterization, improving simulated predictions at the basin scale. Accurate basin scale simulations are required to properly characterize CO_2 mobility, chemical processes, and the subsequent environmental impacts specific to each prospective repository.

CHAPTER 8: SUMMARY

Global warming trends, whether of anthropogenic or natural causes, warn of significant future climatic changes (Jones, 1999). Temperature increases of just a few degrees could cause significant changes to the earth's landscape, including flooding of major coastal regions, comprising a major portion of the human population. In light of the potentially severe threat that anthropogenic emissions may pose, the scientific community has begun to seek out strategies of sequestering CO2 gases from the atmosphere.

Finding safe, affordable, and reliable methods of sequestering CO_2 in the subsurface may be the best near term solution. Of the various proposed strategies to sequester CO_2, injection into deep basin reservoirs has received much scientific attention. Previous numerical studies have indicated intrinsic permeability and capping layer integrity to be the dominant controls on migration rates (Weir, 1996, Law and Bachu 1996, Cole, 1999). However these studies did not consider the chemical reactions between the injected CO_2, formation brine, and geologic media. Chemical reactions may enhance CO_2 trapping due to mineralization, or may decrease mineral trapping through dissolution, thereby increasing absolute permeability and CO_2 mobility. The main goal of this project was to assemble the reactive transport model TR-T, incorporating the influence of chemistry in simulating CO_2 sequestration in geologic media.

Although the TR-T model remains in the developmental stages, simulated results compared favorably to available P.R.R.C. experimental results, providing support that the TR-T model accurately simulates CO_2 sequestration under deep reservoir conditions. Additional TR-T simulations were performed employing a range of geologic media, solution pH, and brine alkalinities. The results indicate that under equivalent volumetric fluid injection of CO_2 and brine, at the prescribed concentrations, there is little difference in the magnitude of dissolution with variation in brine pH and alkalinity. This negligible difference in media response may likely be due to the equivalent volumetric injection of CO_2 and brine, where the brine is always saturated with respect to dissolved CO_2 and therefore dominates the brine properties. The results of the laboratory experiments and the corresponding bench scale numerical simulations suggest that chemical reactivity with the geologic media can be extreme, depending on mineral kinetic reaction rates and the volume of brine fluid present.

Although bench scale simulations and laboratory experiments are a necessary component in better characterizing CO_2-brine-media interactions, reservoir scale simulations are critical in gaining an understanding of the more applicable large scale effects that may be incurred from CO_2 injection. For example, reservoir simulations incorporate more realistic proportions of CO_2 and brine, and decreasing fluid velocities as a function of distance from the injection well. Simulations of a reservoir cross-section models comprised of calcite were performed as a basic examination of larger scale processes, paving the way for future reservoir studies. Contrary to the bench scale model composed of calcite, little dissolution occurred in the comparable calcite reservoir scale model. A

close examination near the injection well revealed that as CO_2 was injected, the brine solution was forced outward away from the injection well, causing the saturation of separate phase CO_2 to increase locally. As the saturation of separate phase CO_2 increased, the mobility of the residual brine solution decreased as a result of decreasing relative permeability and capillary effects. Therefore, simultaneous flushing of several pore volumes of CO_2 and brine through the same rock volume did not occur. As a result little dissolution was predicted in the reservoir as compared to the constant injection bench scale laboratory experiments, showing at first glance that structural changes to the media induced by CO_2 injection at the reservoir scale may be minor.

However, the testing of reservoir processes is far from complete. The aforementioned reservoir model consisted of a perfectly closed reservoir with a homogeneous mineral and brine composition. Fracture flow, mutli-layer geology, varying formation fluid concentrations, and regional flow paths were not considered. Therefore it would be premature to accept the results from the single reservoir analyses performed in this study.

Additional laboratory experiments and representative bench scale simulations must be performed to gain a better understanding of the effects of CO_2 injection into geologic media and to calibrate model parameters for specific types of geologic media. In addition, future reservoir scale simulations must be performed that incorporate the complex structural and chemical signatures specific to each reservoir. We anticipate that the TR-T model will be used in conjunction with experimental results to gain a better understanding of key processes and controlling parameters to assess the safety, viability,

and feasibility of CO_2 injection into specific reservoir environments.

CHAPTER 9: LIMITATIONS

As with any model there are limitations in the capabilities of the TR-T simulator. Some of the limitations are intrinsic to each coupled module, while other limitations are a direct reflection of the method in which we have assembled the first version of the TR-T simulator. In this section we briefly review some of the current limitations.

9.1.1 EOSCO2

There are several limitations of the CO_2 equation of state. The main limitation of EOSCO2 is that it models a pure H_2O-CO_2 system. In other words the CO_2 equation of state does not incorporate the influence of other chemical species on any of the secondary variables. When modeling systems with dilute brine solutions the influence of additional chemical species on secondary variable values may be minor. However, with high TDS brine solutions the effects of additional chemical species may be extreme. Therefore the current version of EOSCO2 is applicable for systems where low TDS brines are present.

In the current version of EOSCO2 the gas phase is represented as pure separate phase CO_2. This representation is not reasonable in many systems, particularly in systems with preexisting gases or near surface environments where an additional gas phase is inevitable. By assuming a pure CO_2 separate phase, the EOSCO2 is valid in brine

saturated deep basin environments where additional gas species are less likely.

Another limitation is the phase partitioning function, which instantaneously transfers CO_2 between the separate and aqueous phases. The actual CO_2 phase transfer is likely dependent upon the degree to which the separate phase is in equilibrium with the aqueous phase. Therefore the EOSCO2 is valid in systems where the rate of phase partitioning would not significantly affect the predicted outcome. Also there is indication from our preliminary analyses that the CO_2 solubility function of Reid et al (1987) used in EOSCO2 needs refinement or should be replaced. Systems of higher pH values may not be properly represented using this relation.

In short the current version of the EOSCO2 is applicable for low TDS, low pH brine saturated environments where the rate of CO_2 phase partitioning is not a controlling factor influencing reservoir processes.

9.1.2 TOUGH2

The main limitations of TOUGH2 linked with the EOSCO2 are maximum number of grid cells and fluid mobility weighting. Large domains are often numerically unstable or computationally unfeasible. This is a significant limitation since small-scale heterogeneities may be lost at the basin scale (future study), which require grid domains employing hundreds of thousands to perhaps millions of grid cells. Therefore to study fine scale processes future simulations must be limited to smaller scale regions to allow

for appropriate grid resolution, reasonable simulation times, and numerical stability. In addition we found that in our simulations that fluid mobility was usually unstable unless the upstream weighting factor was employed which promotes excessive front smearing. We reduced front smearing by decreasing time step size with the tradeoff of increasing computational expense in the simulation. Lowering time step size also decreased mass balance errors in TR-T simulations. In short, grid domains and time step size should be limited to achieve numerical convergence, and reduce excessive front smearing and mass balance errors.

9.1.3 TRANS

The main limitation in TRANS is the relation used to calculate activity. TRANS uses the extended Debye-Huckel equation to calculate activity coefficients, which is usually accurate for brine solutions below 1 Molal. Therefore, brine concentrations should be limited to 1 Molal. This precludes simulating high TDS brine systems above 1Molal, present in many deep basin environments. An applicable activity relation (Pitzer equation) for high TDS brines is available on an unreleased version of TRANS.

9.1.4 TR-T

An initial version of the TR-T simulator was developed in this study. The current version is constrained to using a Cartesian coordinate system. Global mass balances are automatically calculated but local mass balance calculations are deferred to a future project. Mass balance calculations are automated for simulations employing one injection well, while mass balance accounting for multiple CO_2 and brine injection well

simulations requires code modification in the mass balance routine to include contributions from all of the CO_2 injection wells. While we have tested the TR-T model for simple systems, future code development and model verfication is required

CHAPTER 10: FUTURE WORK

Little is understood about CO_2 sequestration in deep basin reservoirs. It is not necessarily the case that CO_2 sequestration in deep basin reservoirs is environmentally damaging, but it certainly has not been shown to be a safe method of reducing atmospheric greenhouse gases. Previous modeling studies have demonstrated the potential for CO_2 returning back to the surface within 100's of years (see previous work section), potentially causing localized environmental problems (e.g., perhaps even asphyxiation), and amounting to a poor financial investment. On the contrary, other simulations have shown that in ideal closed system reservoirs, CO_2 can be sequestered for much longer periods, making CO_2 injection in deep basin reservoirs a viable option (see previous work section). However, these studies have neglected chemical reactivity between the brine, media, and CO_2, which could have major influences on migration rates and induce environmental hazards such as groundwater contamination. Further research must be conducted to determine whether CO_2 sequestration is a safe and economically robust strategy to sequester CO_2, and if so, what type of reservoir environments will act as the best repositories.

The steps required to simulate accurately CO_2 sequestration in deep basin reservoirs are relatively straightforward. We must gain a stronger understanding of mineralization and dissolution kinetics in deep basin environments under high pressure-temperature

conditions, and we must accurately characterize the resulting permeability and porosity relationships that result from these fluid-mineral reactions. In addition, we must upscale results of the bench scale to equivalent parameter values at the basin scale. At the basin scale, we must be able to characterize the lithologic features, brine composition, temperature and pressure gradients, and geometry of fracturing specific to each basin environment. Finally we must incorporate all of this knowledge into a comprehensive model to more accurately predict the effects of CO_2 injection in specific basin environments. Although the outline of these goals is simple, achieving them is much more difficult and will require contributions from many researchers in the earth science community (Wawersik et al., 2000).

There are several avenues for future laboratory experiments involving CO_2 injection into geologic media. Additional laboratory experiments are required to understand fluid-mineral reactions under varying brine composition, CO_2 and brine injection rates, and media type. Testing each parameter for all basin environments is essentially unachievable. The number of experimental parameters in conjunction with the time requirement for each experiment precludes an exhaustive study measuring each possible scenario. It may likely prove more realistic to select variations in brine and media type for a specific reservoir considered for CO_2 injection. Therefore fluid-mineral reactions can be quantified for a specific system and the groundwork will be laid to upscale to basin scale simulations at some future date. Background research of a specific reservoir should be performed to yield realistic ranges for each experimental parameter. Future experiments should also attempt to quantify fluid-media interactions in environments

representative of various temperature-pressure conditions at incremental distances (fluid velocities) from an injection well.

Also, contrary to the dolomite anhydrite experiment in this study, future experiments should incorporate brine solutions in equilibrium with the geologic media of interest at the specified temperature and pressure. Some complications may arise in laboratory preparation and injection of the brine as the equilibrium solution must be mixed and stored prior to injection at the ambient temperature in the core flooding system. Otherwise, some of the brine species may precipitate from solution. In addition some judgment may be required when considering the reported brine compositions for particular formations, as it may be difficult to achieve these exact measured multi-species concentrations in TRANS. There will likely be minor differences between the measured brine composition and the equilibrium concentration. In addition, to predict similar brine composition it will be necessary to characterize accurately the mineral composition of the geologic media. PH is often not reported and may need to be estimated, perhaps simulated by assuming brine equilibrium with separate phase CO_2 and the geologic media. Although additional effort is required in the initial model and experimental setup, brine fluid in equilibrium with the geologic media is more representative of true deep basin conditions. Therefore injecting CO_2 in these systems should closely represent basin reactions induced by CO_2 sequestration.

In addition to the effects of varying fluid properties, matrix (structural) heterogeneities should be considered. Ideally some sort of imaging will be available to measure matrix

structure to calculate porosity distribution throughout the geologic sample at various stages during the experiment. Los Alamos National Laboratory has such capabilities. In this manner one could directly compare the measured to simulated porosity changes caused by fluid-media interactions at each location in the sample. Future analysis may show that while bulk porosity-permeability are unaffected by some variance of the volumetric mineral fractions, there may be stark differences at various locations along the core. In addition several repetitions of each experiment should be performed for each media to quantify the expected variations in fluid-media interactions caused by variations in the media structure and composition.

Aside from scaling issues, if several samples behave nearly identically to one another, then experimental bench scale results may be employed throughout a basin scale model domain. However, if the there is a large degree of variability then some averaging or distribution of parameter values should be employed.

In short, ranges of experimental conditions must be tested for a particular system of interest. A suite of experiments should be performed to measure the range of potential fluid-media interactions as a result of system variability.

Future code development is also needed for the TR-T simulator. For this study a base version of the model was created, but future modification and testing is required. Time step optimization must be improved. In the current version each module follows its own set of time stepping constraints, independent of the mass balance errors occurring in the

other simulator. A local mass balance algorithm should be created along with the global mass balance routine now in place. The global mass balancing routine should be improved to automatically accommodate any combination of injection wells, which now requires code modification (subroutine balla). In addition a subroutine to automatically read the param.mcp (TOUGH-EOSCO2) and grid_input.h (TR-T) files should be created in the driver program. This will prevent the need to recompile the code each time these parameters are changed. In addition the current work array (aa) was patterned after the FLOTRAN structure in the driver program. Using the same array addressing as FLOTRAN reduced the potential to overwrite existing array values, but allowed for some unnecessary array space unused by TOUGH2. To decrease storage in the aa work array some variable locations may be eliminated. The main needs of the TR-T simulator are to perform additional testing, optimize operation efficiency, and create a communication link between TOUGH2 and TRANS so that each simulator considers its impact on global and local mass balances.

Each of the coupled simulators requires some modification. TRANS must be modified to incorporate the Pitzer equation to calculate ion activity so that the TR-T simulator can model high TDS brines. Both TRANS and TOUGH2 should be modified to include a step change injection function to simulate alternating fluid injection scenarios (W.A.G.). If possible the fluid mobility weighting function should be improved such that the harmonically averaged scheme is stable in high injection rate simulations.

The CO_2 equation of state requires the most modification. The CO_2 solubility function

(Reid et al., 1987) needs modification or replacement. At higher pH differences between individual CO_2(aq) species and total aqueous CO_2 becomes significant. The current relation by Reid et al (1987) is likely assuming the solution is at low pH. Prior analysis revealed this relation is representative of the measured individual CO_2(aq) species. In addition the fugacity and enthalpy functions need modification. Essentially all of the secondary variables must incorporate the effects of additional chemical species. Also, the instantaneous CO_2 phase partitioning function should be replaced by a rate phase transfer function as described in the equation of state section. Making these required improvements will dramatically improve the accuracy and applicability in using the TR-T simulator to model most deep basin environments.

REFERENCES

Adeneken, A., T. W. Patzek, et al. (1993). "Modeling of multiphase transport of multicomponent organic contaminants and heat in the subsurface." *Water Resour. Res.* **29**(11): 3727-3740.

Anderson, O. L., H. Oda, et al. (1992). "A Model for thermal expansivity at high compression and high temperature." *Geophys.* **19**.

Angus, S. B., B. Armstrong, et al. (1973). Thermodynamic tables of the fluid state: carbon dioxide. Pergamon, Oxford.

Arvidson, R. S., A. Luttge, (2000). Vertical scanning interferometry; the holy grail of low temperature dolomite precipitation kinetics. *Geological Society of America, 2000 annual meeting Abstracts with Programs - Geological Society of America*, 32, no. 7 (2000): 79

Aziz, K. and A. Settari (1979). "Pertroleum Reservoir Simulation." *Applied Science.*

Celia, M. A. and W. G. Gray (1992). Numerical Methods for Differential Equations, Prentice-Hall.

Cole , B. S. (1999). "An equation of state for multiphase CO_2 and water." Independent Study (M.Sc), New Mexico Institute of Mining and Technology.

Committee, I. F. (1967). A Formulation Of The Thermodynamic Properties Of Ordinary Water Substance. Dusseldorf, Germany, IFC Secretariat.

Edwards, A. L. (1972). TRUMP: A computer Program for transient and steady state temperature distributions in multidimensional systems. Springfield, VA, Nat. Tech. Inf. Serv.

Enick, R. M. and S. M. Klara (1990). "CO_2 Solubility in water and brine under reservoir conditions." *Chem. Eng. Comm.* **90**: 23-33.

Enick, R. M. K., S.M. (1990). "CO_2 solubility in water and brine under reservoir

conditions." *Chem. Eng. Comm.* **90**: 23-33.

Folk, R. L. (1962). "Spectral subdivision of limestone." *Amer. Assoc Petrol. Geol. Mem.* **1**: 62-84.

Holt, T., I. Jensen, et al. (1995). "Underground storage of CO_2 in aquifers and oil reservoirs." *Ener. Convers. Mgmt.* **36**: 535-538.

Johnson, J. W., S. C. I., et al. (2000). "Reactive transport modeling of subsurface CO_2 sequestration: Identification of optimal target reservoirs and evaluation of performance based on geochemical, hydrologic, and structural constraints." Energex.

Jones, P. D., D. E. Parker, (1999). Global and hemispheric temperature anonmalies - land and marine instrument records. Trends: A Compendium of *Data on Global Climate Change*. Oak Ridge, Tenn., National Laboratory, U.S. Department Of Energy.

Knox, P.R., and S.D. Hovorka, 2001, Geological sequestration of greenhouse gases: opportunities for Industry-Academe research partnerships, *Houston Geological Society Bulletin*, January, p. 26–33

Land, L. S. (1998), Failure to precipitate dolomite at 25 degrees C from dilute solution despite 1000-fold oversaturation after 32 years. Geochemistry of low temperature processes *Aquatic Geochemistry*. 4, no. 3-4 (1998): 361-368

Langmuir, D. (1997). Aqueous Environmental Geochemistry. Upper Saddle River, New Jersey, Prentice-Hall Inc.

Langmuir, D. and J. Mahoney (1985). Chemical equilibrium and kinetics of geochemical processes in ground water studies. Canadian/American conference on hydrgeology, Ohio, National Well Assoc.

Law, H. S. and S. Bachu (1996). "Hydrological and Numerical Analysis of CO_2 disposal in deep aquifer systems in the Alberta sedimentary basin." *Ener. Convers. Mgmt* **37**(6-8): 1167-1174.

Leverett,M.C. (1941) Capillary behavior in Porous Solids, *Trans Soc. Pet. Eng.* AIME, 142, 152-169

Lichtner, P. C. (2000). FLOTRAN Users Guide. Los Alamos, New Mexico, Los Alamos National Laboratory. DRAFT.

Lichtner, P. C., C. I. Steffel, et al. (1996). Reactive Transport in Porous Media. *Reviews In Mineralogy*. P. S. Lichtner, C.I.;Oelkers,E.H.

Litchner, P. C. (2000). Flotran Programmers Manual. Los Alamos National Laboratory.

Lindeburg, E. (1995). Escape of CO_2 from large horizontal aquifers confined only be a cap seal. Conference: Greenhouse Gases: Mitigation Options.

Lith, Y.V and R. Warthmann (2000), Role of Sulfate Reducing Bacteria During Microbial Dolomite Precipitation as Deduced from Culture Experiments. Journal of Conference, *Cambridge Publications*, September 3rd–8th, Volume 5(2), 1038 Oxford, UK.

Marland, G. and T.A. Boden (1999). Global, Regional, and National CO_2 emissions. In Trends: A compendium of Data on Global Change. Oak Ridge, Tenn., Carbon Dioxide Information Analyses Center, Oak RIdge National Laboratory, USA.

Narasimham, T. N. and P. A. Witherspoon (1976). "An integrated finite difference method for analyzing fluid flow porous media." *Water Resour. Res.* **12**(1): 57-64.

Parker, J. C., R. J. Lenhard, et al. (1987). "A parametric model for constitutive properties governing multiphase flow in porous media." *Water Resour. Res.* **23**(4): 618-624.

Patel, M. R. and P. T. Eubank (1988). "Experimental densities and derived thermodynamic properties for carbon dioxide-water mixtures." *Journal Of Chemical Engineering Data* **33**: 185-193.

Peaceman, D. W. (1977). Fundamentals of Numerical Reservoir Simulation. Amsterdam, Elsevier.

Pruess, K. (1999). TOUGH2- a general-purpose numerical simulator for multiphase fluid and heat flow, Lawrence-Berekley Laboratory.

Reid, R. C., J. M. Prasnitz, et al. (1987). The Properties Of Fluids And Gases. New York, McGraw-Hill.

Sjoberg, E. L. and D. T. Rickard (1987). "Temperature dependence of calcite dissolution kinetics between between 1 and 62°C at pH 2.7 to 8.4 in aqueous solutions." *Geochim Cosmochin Acta* **48**: 485-493.

Stumm, W. (1992). Chemistry of solid water-interface. New York, Wiley.

Van Der Meer, L. G. H. (1993). "The conditions limiting CO_2 storage in aquifers." *Ener. Convers. Mgmt.* **34**(9-11): 959-966.

Van Der Meer, L. G. H. (1995). "The CO_2 storage effieciency of aquifers." *Ener.*

Convers. Mgmt. **36**(6-9): 513-518.

Van Genutchten, M. T. A. (1980). "A closed form equation for predicting the hydraulic conductivity of unsaturated soils." *Soil Science Society of America Journal* **44**: 892-898.

VanderKwaak, J. E., P. A. Forsyth, et al. (1995). "WATSOLV, Sparse Matrix Iterative Solver Package, Users Guide. Waterloo, Ontario, Canada: Waterloo Centre for Groundwater Research, University of Waterloo." .

Vesovic, V., G. A. Wakeham, et al. (1990). "The Transport Of Carbon Dioxide." *J. Phys. Chem. Ref. Data* **19**(3): 763-808.

Wawersik, R., W., F. M. Orr, et al. (2001). "Terrestrial Sequestration of CO_2: An Assessment of Research Needs." *Advances in Geophysics* **43**.

Weir, G. J., S. P. White, et al. (1996). "Reservoir storage and contaminant of greehouse gases." *Transport in porous media* **23**: 37-60.

White, A. F. and B. S.L. (1995). "Chemical weathering rates of silicate minerals." *Rev. Mineral* **31**: 1-583.

Wolery (1983). EQ3NR, "A Computer Program for Geochemical Aqueous Speciation-Solubility Calculations: User's Guide and Documentation" UCRL-53414, Lawrence Livermore National Laboratory,.

APPENDIX A: DESIGN, CREATION, AND TESTING OF A HIGH PRESSURE PERMEAMETER

INTRODUCTION

Optimizing sequestration of CO_2 in deep basin reservoirs requires a strong understanding of fluid-mineral reactions induced by CO_2 injection. Of particular importance is the effect of chemical reactions on absolute permeability of the media. CO_2 injection may cause mineral dissolution perhaps increasing matrix permeability and enhancing CO_2 mobility. Alternatively, mineralization may reduce absolute permeability, perhaps decreasing CO_2 mobility. Other reactions such as sorption, ion exchange, and colloidal transport may also affect the matrix structure. The permeability changes may be dependent on the injection rate, fluid compositions, media type, and basin pressure and temperature conditions. Since these properties will differ between basins, permeability changes due to CO_2 injection will be reservoir specific. Therefore one must test how the site-specific fluid-mineral reactions affect permeability under representative conditions. To better understand the physical effects to the matrix induced by CO_2 injection, a permeameter was engineered which could measure the matrix permeability of a consolidated sample under high pressure, moderate temperature, and corrosive conditions.

DESIGN

The basic permeameter design is simple but robust. A sample is held in the permeameter reservoir. Fluid enters the reservoir through the inlet, flows through the sample, and exits through the outlet. The fluid properties and media in the reservoir cause a fluid pressure drop across the sample, where the fluid at the inlet is at a higher total potential than the outlet. The design becomes more complicated with high pressure systems using precision instrumentation and automated data acquisition methods, as implemented in this study. Yet, the basic functions of the permeameter remain similar. The permeameter provides the pressure difference across and flow rate through a sample required to calculate the absolute permeability of the geologic media. Under laminar flow the permeability could be calculated by the Darcy's law equation.

Time intensive permeability experiments, such as mineral/dissolution induced permeability reductions, require automated data acquisition. Some experiments may require months till completion, rendering manual data collection inappropriate and inefficient. Also manual data entry introduces the potential for human error in recording instrument values.

In addition to implementing automated data acquisition to improve data collection, the permeameter was designed to operate under representative subsurface environments. Under atmospheric pressure conditions with non-corrosive fluids and unconsolidated media, permeameter reservoirs made from rubber tubing and glass or plastic are satisfactory. However, these standard permeameters cannot be used for high pressure,

moderate temperature experiments in the presence of a corrosive fluid such as CO_2. Also it is difficult to prevent preferential fluid flow along the vertical edges of the core sample in such permeameters. Therefore, high pressure, corrosive resistant components were used in the permeameter design. All fluid contact regions are composed of 316 chemical resistant stainless steel or Hastoloy®, and all components and instruments are rated to at least to 3000 and up to 60,000psi. Corrosion resistant materials and instruments with high pressure and temperature resistance allows the permeameter to measure the effects of CO_2 injection under representative deep basin conditions.

The permeameter schematic is depicted in Figure 1. Stainless steel tubing connects all of the instrumentation. Fluid is pumped through the tubing and instrumentation using an ISCO 500D syringe pump controlled by an ISCO series D pump controller. The ISCO pump is set to constant flow mode at a prescribed volumetric flow rate. Fluid travels through the tubing into the inlet of a pressure vessel that holds the sample. The sample is encased in thick rubber tubing within the pressure vessel. A confining fluid is pumped into the pressure vessel prior to testing, creating a confining pressure around the sample. An axial load is applied to the sample, prior to testing, by a hydraulic press. Fluid flows into the pressure vessel, flows through the sample and then exits through the outlet. At the outlet a TEMCO backpressure regulator series BPR-50 (BPR), sets the outlet pressure. Nitrogen gas is used to apply the dome pressure in the BPR. The outflow must overcome the nitrogen gas

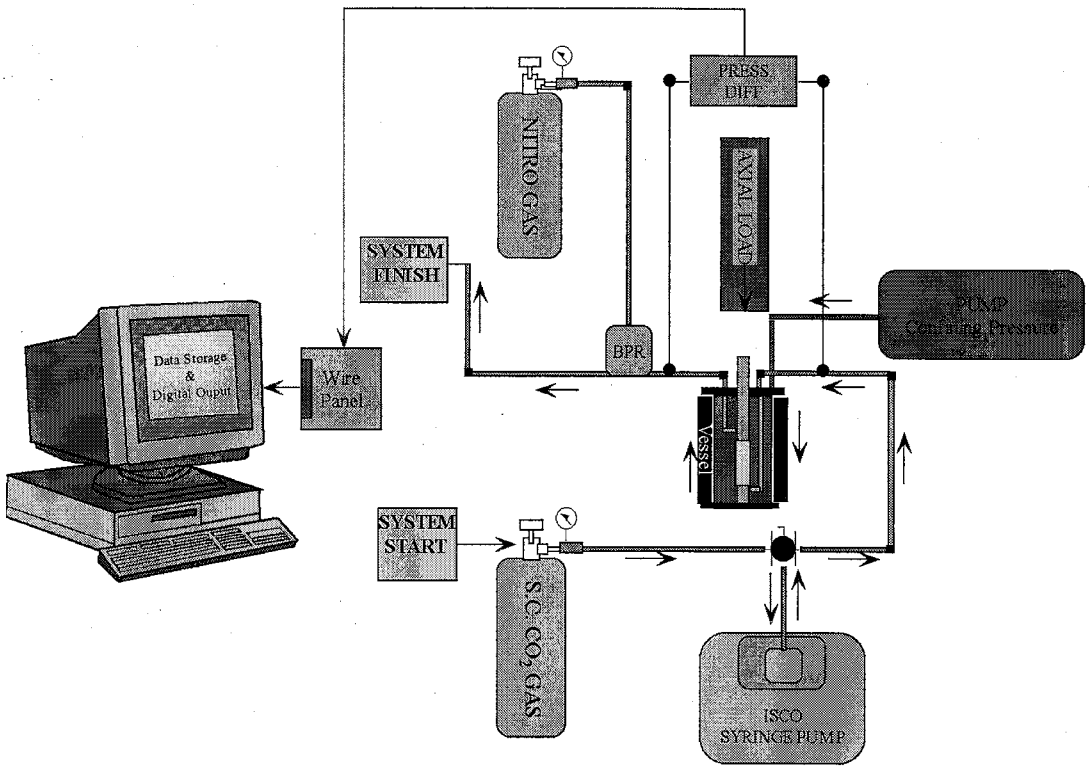

Figure 1: Schematic of permeameter. A fluid solution is pumped from the ISCO syringe pump into the pressure vessel containing the sample. A confining pump maintains the confining pressure against the sample. The pressure drop across the sample due to fluid flow is measured with a pressure differential.

back pressure in order for the fluid to flow through the BPR valve. A Validyne very high line, variable reluctance, differential pressure transducer wired to a Validyne CD15 Sine Wave Carrier Demodulator is used to measure the pressure difference across the rock core sample. The output signals are converted from analog to digital using a National Instruments Incorporated data acquisition card and software, and the results are recorded directly to a computer output file.

INSTRUMENT DESCRIPTIONS

- Tubing-Tubing connections: .28cm inner diameter type-316 chemically resistant stainless steel. Connections are Superpressure brand Lot No. 54360 No. 45-1434

rated to 60,000psi.

- Temco Back Pressure Regulator: dome loaded BPR series -model BPR-50: BPR is externally loaded by gas or liquid pressure. The line pressure must overcome the dome pressure for the fluid to pass through the BPR. Allowable flow rate ranges is from 1-600 ml/hr. the BPR is also constructed of type-316 chemical resistant stainless steel and can endure temperatures up to 100°C.

- Validyne Very High Line-Variable Reluctance- Model DP-48- Differential Pressure Transducer: measures the pressure difference between two points in a system. The pressure-sensing element is a flat diaphram of magnetic stainless, clamped between case halves of the same material, in a symmetric assembly. Pick-off coils, embedded in each case halve, sense the diaphram deflection. The maximum pressure differential is printed as 550kPa, but a more realistic maximum, due to the age of the instrument, is estimated to be 420kPa. The linearity is +/- .5 % best straight line, the hysteresis is .5% pressure excursion, maximum line pressure is 8.65×10^4 kPa, and the operating temperature range is –20°C to +125°C.

- Validyne Sine Wave Carrier Demodulator Model CD15: sine wave carrier designed to operate with variable reluctance transducers to provide a DC output signal for dynamic as well as steadystate measurements. The instrument supplies regulated carrier exitation of a 5Vrms, 5kHz sine wave to the two-inductance

ratio arms of the transducer. The resulting output is demodulated and amplified using integrated circuit techniques. The ZERO and SPAN controls allow to adjust for any imbalance in the system and to match the transducer sensitivity.

- ISCO Series 500D Syringe Pump and Series D Pump Controller: capable of pumping a wide range of fluids. The pump reservoir is made of Hastalloy®, which is highly chemical resistant but is not impervious to pitting by hard colloidal particles. The allowable flow rate ranges from 0-204ml/min with an accuracy of +/- .5%. Refill time is 2.5 minutes. Pressure accuracy is +/- 2% full scale with a repeatability of +/- 1% of full scale. The ambient temperature can range between 0-40°C.

- Pressure Vessel: fabricated from aluminum and stainless steel (Figure 2). Two circular aluminum endplates (3.4cm in height x 15.7cm diameter) with 6 bolt-holes symmetric around the outer circumference, cap a hollow aluminum cylinder (1.4cm wall thickness x 10cm diameter x 29cm in length). High-pressure rubber gaskets lie between the endplates and the cylinder. Within the pressure vessel, a type-316 stainless steel base (3.4cm diameter x 6cm long) contains an inflow port fastened to its bottom plate. The sample core sits between this lower base and an upper shaft also of 3.4cm diameter, which contains the outflow port. The load shaft (3.4cm x 15cm in length) runs through the center of the top endplate and when in operation applies pressure to the upper shaft resting over the sample. Thick rubber tubing (.56cm thick) covers the sample and overlaps

approximately 1.7 cm on each shaft. This seals the sample from the confining fluid that is pumped in the main body cylinder of the pressure vessel.

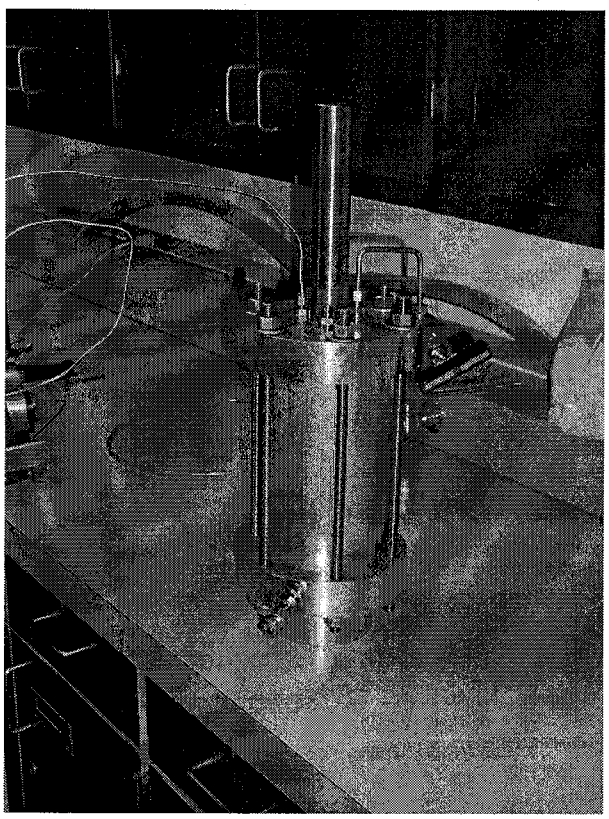

ar

Figure 2: Photograph of pressure vessel

- National Instruments Data Acquisition Package: a NI-4351 data acquisition card, TBX-68 terminal block, SH6868 shielded cable, and Lab View software comprise the data acquisition system. Instruments are wired to the TBX-68 terminal block. A personal computer reads the signals from the instruments using the Lab View software, converting the signal from analog to digital. The system allows data to be converted from an analog signal of the instrument to a digital signal that is readable by a PC.

INSTRUMENT CALIBRATION/PERMEAMETER EFFECTS

The ISCO syringe pump and the Validyne pressure differential required calibration to ensure accurate permeability measurements from the permeameter. The ISCO 500D syringe pump was verified for pressure accuracy using a Parascientific Digiquartz Incorporated portable pressure standard, and for flow rate accuracy using a stop watch and a 500ml graduated cylinder. The portable standard was connected to the syringe pump reservoir aperture and reset prior to each calibration test. The syringe pump was set to a specified pressure level and line pressure was allowed to equilibrate for 3 minutes.

For the pressure test, the syringe pump was set to a constant pressure of 250kPa and the portable standard read 248.11kPa. For the second test the syringe pump was set to a constant pressure of 500kPa and the portable standard indicated a pressure of 497.21kPa, showing good agreement and within the +/- 2% pressure accuracy of the syringe pump and .01% pressure accuracy of the portable standard stated in their respective manuals.

The syringe pump flow rate accuracy was tested using a stopwatch and a graduated cylinder. The cylinder was used to ensure that all of the fluid had been expelled from the syringe pump reservoir during a test. The syringe pump reservoir was filled and the reservoir volume was read from the controller display. A flow rate was specified and the expected time to empty the reservoir was compared to the actual time. Table 1 shows the results of the flow rate tests, where time was rounded to the nearest second. The results indicate that the average flow rate is within the precision of the stopwatch method and is

within the .5% accuracy stated in the manual.

Flowrate (ml/hr)	Cylinder Volume (ml)	Expected Time (sec)	Actual Time (sec)
10,000	507.84	183	183
5,000	507.8	366	366
1,000	507.85	1828	1829
500	507.8	3656	3656

Table 1: ISCO 500D syringe pump flow rate verification

In addition, the Validyne very high line, variable reluctance, differential pressure transducer was calibrated using the Parascientific Digiquartz portable pressure standard. The Validyne pressure differential was wired to a Validyne Model CD15 Sine Wave Carrier Demodulator to amplify voltage signal. The ISCO syringe pump was used to apply a specified pressure to the system, which was read by the Digitquartz pressure standard. Since the pressure differential instrument measures the pressure difference between its two ends, a better calibration would involve applying specified pressure differentials at various pressure magnitudes, but with the available instrumentation this was not possible. Preliminary testing showed nearly identical voltages using either end of the pressure differential at the same pressure, so it was assumed that the pressure differential could be calibrated with one end attached to the syringe pump applying a known pressure. The syringe pump was set on constant pressure mode, at a specified pressure, and the system was allowed to equilibrate for 3 minutes. The pressure indicated on the pressure standard display was recorded along with the voltage output of the carrier demodulator. The pressure differential is rated for a maximum pressure difference of 550kPa (80psi) across the sample, but testing showed a nonlinear voltage-pressure

response beyond 420kPa (60psi). Thus, the pressure differential was calibrated to 420kPa rather than its rated maximum of 550kPa. The voltage pressure relationship was plotted beginning at 0 pressure to a maximum pressure of ~420kPa and back down to 0 pressure (Figure 3). Linear fits to the increasing and decreasing data points measured at 7

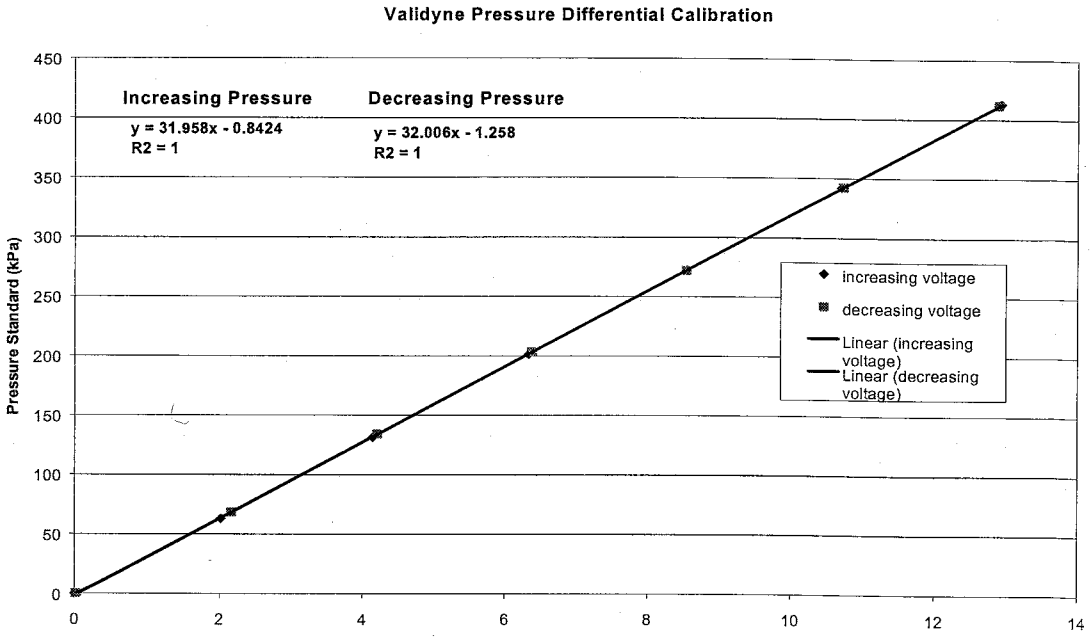

Figure 3: Pressure-Voltage Calibration of Validyne Pressure differential

different pressure values are shown to have R^2 values of ~1. An average of the two linear trend lines was considered representative of the pressure-voltage calibration (Eq 1).

$$P(kPa) = 32 \cdot MV(V) - 1$$

Eq 1: Average linear trend regression for Validyne pressure differential. Pressure in kPa (P(kPa)), meter voltage in volts (MV(V))

This relation was used to convert voltage response to equivalent pressure in all subsequent testing.

Drift

Preliminary testing showed some instrument drift during testing periods. The ISCO syringe pump was set to constant pressure mode at specified pressures of 70kPa and 135kPa (Figure 4), which corresponds to This is the pressure differential range expected during testing. Lower

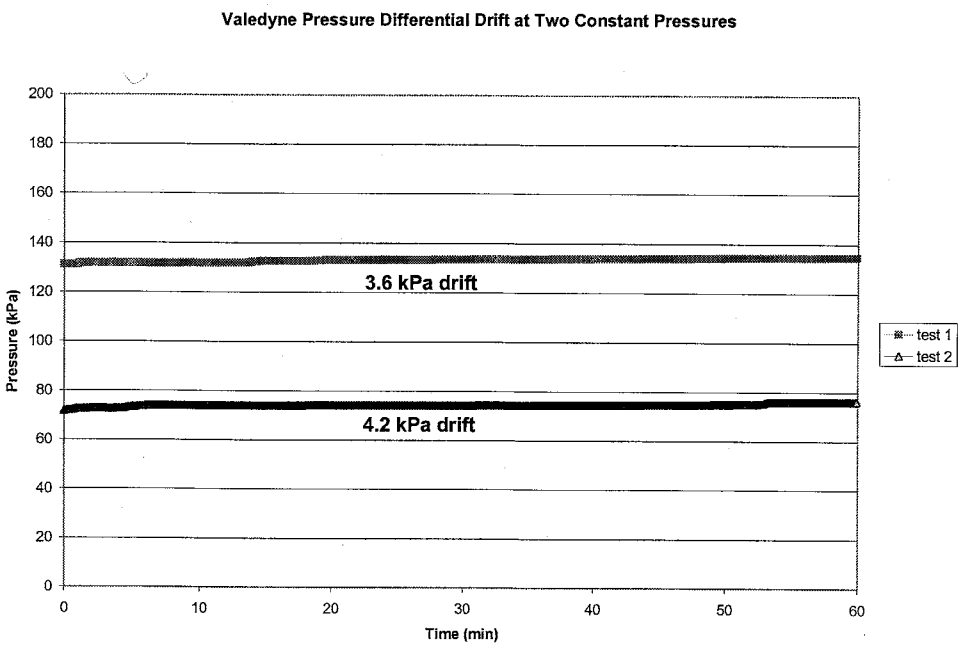

Figure 4: Example of drift of Valydyne pressure differential at constant pressure. Test 1 pressure (green) is set constant at 135kPa. Test 2 pressure (blue) is set constant at 70kPa. Test duration is 60 minutes

pressure tests may have been helpful, but the syringe pump minimum pressure is 70kPa and thus limited to operation at constant pressures above 70kPa. The measured drift

averaged .06V with average voltage magnitudes of 2.3 and 4.2 volts over 60 minutes of testing. Voltage output drift is often a sign of inadequate grounding or instrument error. The older wiring of the pressure differential or the sine wave demodulator could be the culprit. Though they exhibit little degradation, both instruments are 20 years old. Perhaps re-wiring the pressure differential and the frequency demodulator would remove the minor drift. Also, the aged mechanical diaphragm of the pressure differential may be worn from repeated pressure fluctuations during previous experiments. However, some key observations are noted; the drift is rather small in relation to the pressure differentials expected during testing, and the drift is linear and can be removed from the raw data. Therefore, discovering the cause of the consistent drift was not considered imperative, and the drift was removed from the data without further error analyses. Instrument drift of 4kPa over 60 minutes was removed from the data using a linear regression trendline correction (Eq 2). Pressure was removed as a function of time where the corrected pressure equals the measured pressure minus the drift at a particular time in the experiment.

$$P_C = P_m - t_{\min} \cdot \left(\frac{4kPa}{60\,\min utes} \right)$$

Eq 2: Corrected permeability equation. Corrected pressure (P_c), measured pressure (P_m), time in minutes (tmin)

Permeameter Resistance

In addition to the instrument calibrations, the pressure loss across an empty permeameter was calculated to ensure accurate results. The permeability test results actually provide the effective permeability, a function of both the core sample and resistance of the

instrument. The instrument permeability was measured using a flow rate of 750ml/hr without a sample present, which is the highest expected experimental flow rate in future experiments. The instrument permeability (resistance) was calculated to be on the order of $10^{-7}cm^2$ (Figure 5). It was considered appropriate to calculate the permeability as a harmonic average of the instrument permeability and the core sample intrinsic permeability. When using a harmonic average, the smaller permeability controls the magnitude of the effective permeability. The minimum effective permeability values measured in this study fall in the 10^{-9} cm^2 range, two orders of magnitude lower than the empty instrument permeability. With an effective permeability of 1.0×10^{-9} cm^2, the calculated intrinsic permeability would be $.99 \times 10^{-9} cm^2$, demonstrating a negligible difference between the effective and intrinsic permeability. The influence of the permeameter would be expected to decrease with lower permeability samples. Despite the slight mechanical resistance of the permeameter, the effective permeability is considered equal to the core sample permeability.

ROCK SAMPLE CALIBRATION

A Berea sandstone core sample of known permeability was used to test the accuracy of the permeameter. The Berea sandstone was purchased from American Stone Incorporated, a major supplier of Berea sandstone. The sample permeability reported by American Stone Incorporated is 500 mD (5.0×10^{-9} cm^2). A cylindrical sample measuring 3.4cm diameter x 7.25cm in length was cored from a larger slab. Six successive H_2O permeability tests were performed on the sample, four at a flow rate of 500ml/hr and two at a flowrate of 750ml/hr (Figure 6). The average permeability calculated by the

permeameter

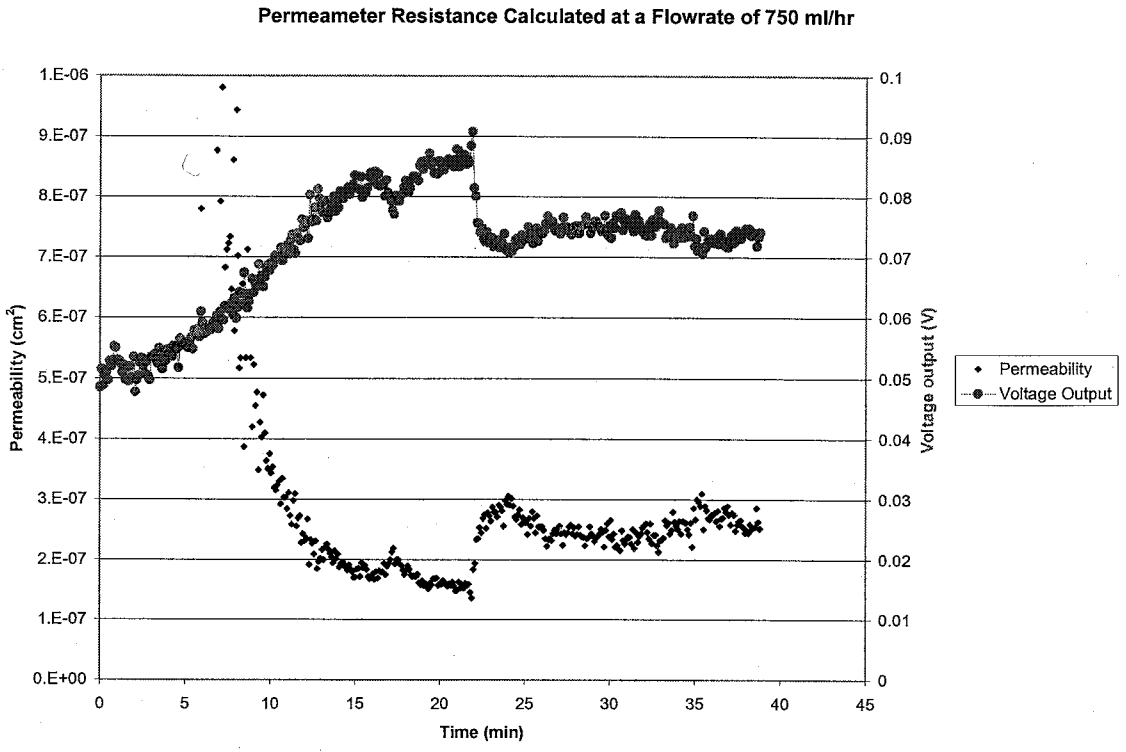

Figure 5: Example of measured pressure drop in permeameter with 750 ml/hr fluid injection (without core sample).

is 5.07 x 10^{-9}cm^2, in good agreement with the 5 x 10^{-9} cm^2 permeability values supplied by American Stone Incorporated. Permeability values varied +/- 4 x 10^{-10} cm^2, an order of magnitude less than the average permeability. The distribution of values is shown in (Figure 7). A q-q normal distribution plot is used to ascertain whether the data is normally distributed (Figure 8). The range of permeability is shown to have a linear relationship with the Z score, an indication that the data is normal distributed.

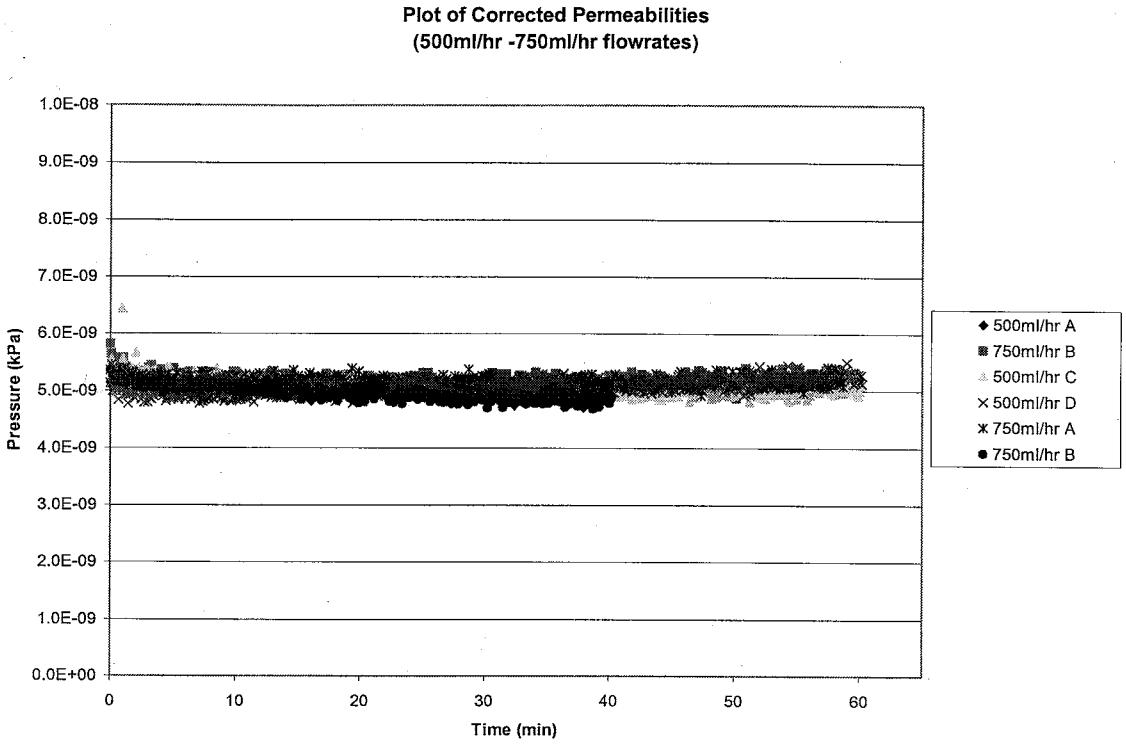

Figure 6: Example of permeability testing of Berea Sandstone sample using the permeameter developed in this study

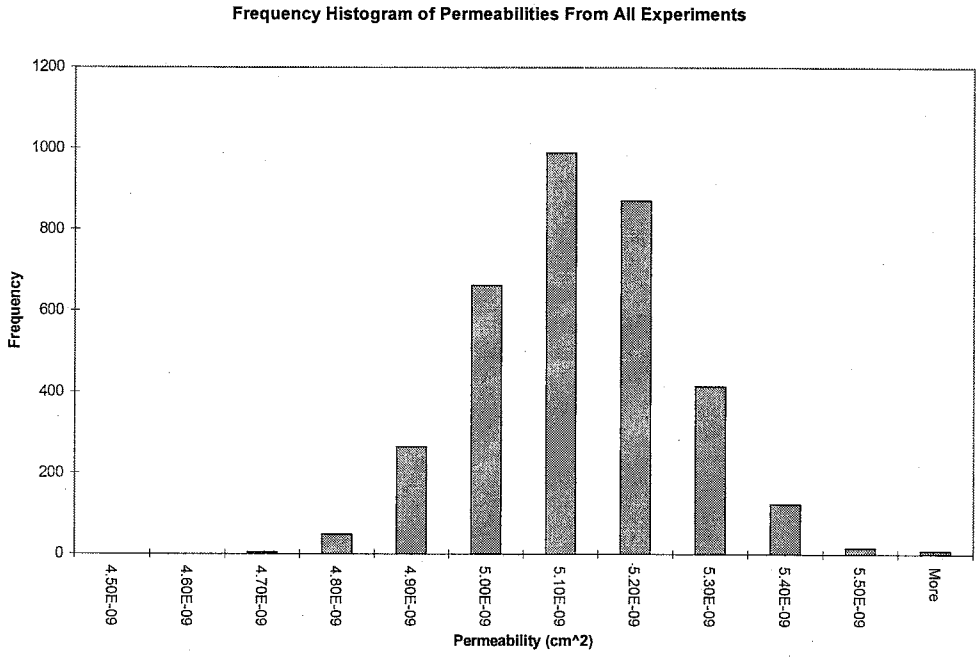

Figure 7: Histogram of combined permeability test values

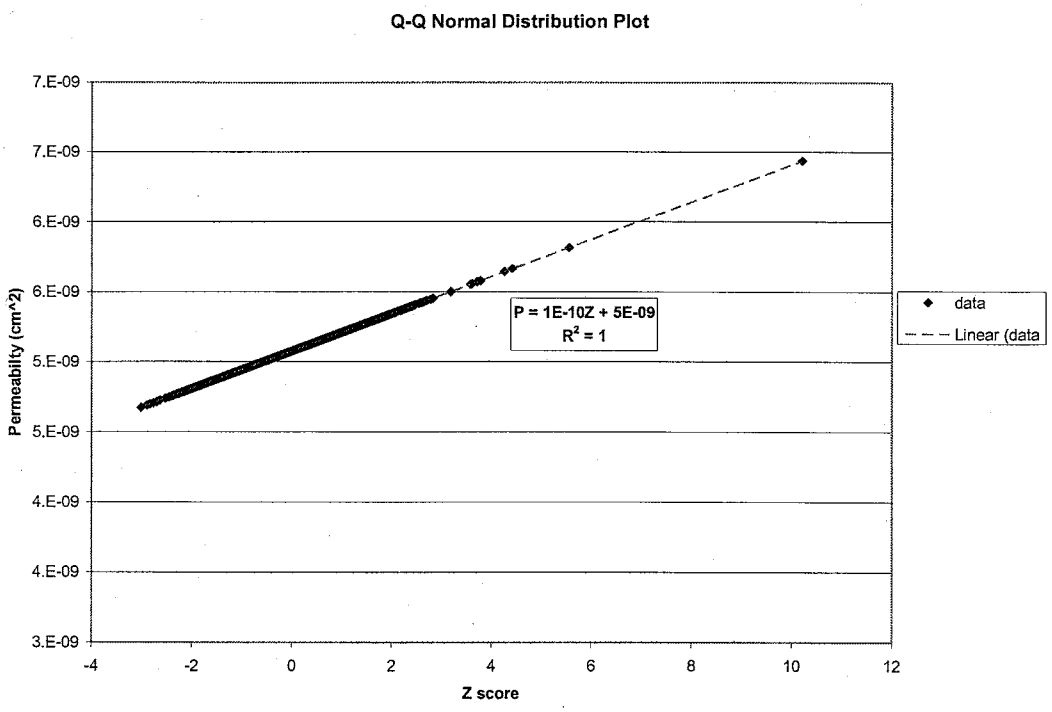

Figure 8: Q-Q plot showing normal distribution of permeability data

population. In this case, 95 percent of the measurement fall between 4.81 x 10^{-9} to 5.34 x10^{-9}cm^2. Also, the permeability range calculated by the permeameter of 4.81 x 10^{-9} to 5.34 x 10^{-9} cm^2 encompasses the permeability value of 5 x 10^{-9} cm^2 specified by American Stone Incorporated. This series of tests demonstrate the ability of permeameter to accurately measure the permeability of a rock sample to an accuracy 2.5 percent.

INSTRUMENT LIMITATIONS

The permeameter provides an effective base design for future research. The ISCO 500D syringe pump is capable of pumping most fluids, ranging from low viscosity gases to highly viscous viscoplastic fluids. The pump reservoir, made of Hastelloy®, is very

resistant to corrosive chemicals but susceptable to pitting from hard colloidal particles within a fluid. Experiments using fluids containing hard colloidal particles should be avoided, as they will damage the reservoir. The fluid reservoir has a capacity of 507ml and therefore the maximum test duration is controlled by the specified constant flow rate. At a flow rate of 500ml/hr, experiments can be run for up to 60 minutes. The reservoir can be re-filled in 2.5 minutes. If pausing the experiment for 2.5 minutes is not acceptable, then an additional syringe pump should be linked in tandem, using an appropriate pump controller, so that the additional pump will operate during the refill period while the main pump reservoir refills. The temperature in the reservoir is limited to a range of 0-40°C. However, under normal thermal gradients the permeameter can represent up to a 1km depth. A heating unit may be applied to the permeameter lines and pressure vessel to maintain the testing temperature. The maximum pressure of the syringe pump and pressure vessel is 3000 psi, which is sufficient to reproduce most reservoir conditions. The flowrate range is from 0-204ml-min^{-1} depending upon the line pressure, but is well above the 8.3ml min^{-1} flow rate used in this study. The BPR valve handles a maximum flow rate of 10ml-min^{-1}, and therefore provides the greatest instrument limitation in the permeameter design. If a flow rate higher than 10ml-min^{-1} is desired then an alternative back pressure system will need to be implemented. While there are limitations to the permeameter, the instrument provides reliable, accurate permeability measurements for temperatures between 0-40°C and pressures up to 3000 psi.

SET-UP PROCEDURE

The specific set-up procedure may vary from one experiment to the next, either by

experimental differences or preferred laboratory practices of different researchers. The following lists provide a baseline set-up procedure used in this study for sealing the sample in the pressure vessel and running a permeability test. The test procedure list assumes that the permeameter is functional and properly calibrated.

- Process Sample: Cut the core sample, use a rock-core drill bit attached to a floor dill. A lathe may be used to face the sample ends. The sample should be cylindrical with a radius of 1.70cm and a length close to 6.7cm.

- Pre-Saturate Sample: Apply a vacuum to the sample, using a bell jar and either a roughing pump or laboratory vacuum line, for at least 2 hours. Remove sample from bell jar and immediately submerge sample in container of the fluid being used in the experiments.

- Seal Sample: Attain some 10cm inner diameter .56cm thick rubber tubing that softens well when exposed to heat. Cut a piece of the tubing 11cm long, and square both ends with a utility knife. Heat the tubing with a heat gun for about a minute and gently insert the sample in the tubing, leaving equal overlap on each end.

- Support Pressure Vessel: Use a sturdy laboratory ring stand with 3 Castaloy clamps to hold each part of the vessel components.

- Check Component Order: Ensure the set –up consists of (from top to bottom) the load shaft, upper shaft, upper hose clamp, sample encased in tubing, lower hose clamp, and lower base. The inflow tubing should be connected to the lower shaft and the outflow tubing shall be connected to the upper shaft (Figure 9).

- Assemble Pressure Vessel: Insert sample and excess tubing over lower and upper shafts. Since the sample is centered in the tubing, the tubing should slide equally onto the upper and lower shafts. The tubing must cover the O-ring gaskets inset into the upper and lower shafts. Fasten the hose clamps as tightly as possible (by hand) over the tubing at the o-ring locations. Remove the pressure vessel from the Castoloy clamps.

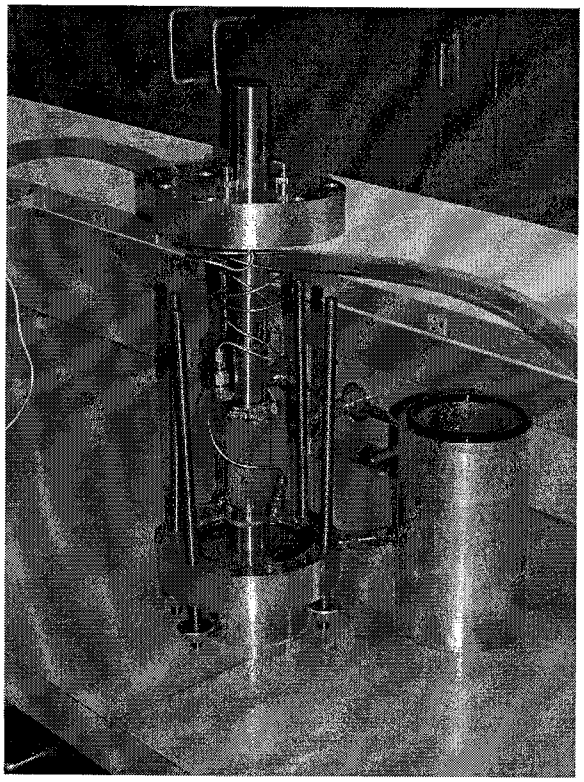

Figure 9: Disassembled pressure vessel: core sample is held between two shafts, sealed with a protective Tygon tubing sleeve. Inflow enters the bottom shaft and fluid moves through the sample and exits through the top outlet

- Secure Pressure Vessel: Gently begin pushing pressure vessel together. Make sure the gaskets are present and that the stainless steel tubing for the inflow and outflow are not caught between the endplates and the main body alumimum cylinder. Slide bolts through boltholes of pressure vessel. Finger tight each bolt. Alternate to the next bolt once the current bolt being tightened is snug. This process will begin to compress the gaskets. Continue alternating between bolts until all bolts remain tight during one loop through. This ensures the gaskets will properly seal during the experiment.

- Test Pressure Differential: Release line pressure before a new experiment, by opening some part of the system. Check that the voltage output returns to near 0 after just few seconds. Periodic re-calibration of the instrument is recommended.

- Refill Syringe Pump Reservoir. Turn the valve, connected to syringe pump, 180 degrees such that the arrow on the knob points opposite to the test flow direction. Push the refill button on the syringe pump controller. The refilling will stop once the reservoir is full. Turn valve knob 180 degrees so that the arrow points in the direction of flow. Reset pressure to 0 on pump by pressing the "zero pressure" button on the controller.

- Run test: set the flow rate using the constant "flow rate" option on the controller.

Finally begin logging pressure data through the data acquisition system.

Following these steps provides the user with a basic set-up procedure that may be modified for a specific application.

CONCLUSION

The permeameter design provides a solid base design for future studies. The permeameter can operate at pressures of up to 3000psi and temperatures from 0-40°C. Fluids may be highly viscous and moderately corrosive. Statistical tests showed that the data fluctuations about the mean are normally distributed and probably a function of signal noise from the pressure differential or shielded cable. Calibration and error analyses show that the permeameter may have up to a 2.5% error with 95 percent of the data population, resulting in accuracy of 97.5-100 percent for permeability values of 10^{-9} cm^2 and below. The permeameter provides a valuable tool to measure the effect of fluid injection on media permeability. Future studies will incorporate the use of the permeameter to measure the effects of CO_2 injection in geologic media.